



Lotta Bergman

Influence of surface functionalization on the behavior of silica nanoparticles in biological systems

Laboratory of Physical Chemistry
Center for Functional Materials
Department of Chemical Engineering

2014



Influence of surface functionalization on the behavior of silica nanoparticles in biological systems

Lotta Bergman

Laboratory of Physical Chemistry
Center for Functional Materials
Department of Chemical Engineering
Åbo Akademi University
Åbo, Finland 2014

Supervised by

Prof. Mika Lindén
Institute for Inorganic Chemistry II
University of Ulm
Germany

Prof. Jouko Peltonen
Laboratory of Physical Chemistry
Åbo Akademi University
Finland

Reviewed by

Adj. Prof. Hélder A. Santos
Faculty of Pharmacy,
University of Helsinki
Finland

Assoc. Prof. Freddy Kleitz
Department of Chemistry
Université Laval
Quebec, QC
Canada

Opponent

Adj. Prof. Hélder A. Santos
Faculty of Pharmacy
University of Helsinki
Finland

Abstract

Personalized nanomedicine has been shown to provide advantages over traditional clinical imaging, diagnosis, and conventional medical treatment. Using nanoparticles can enhance and clarify the clinical targeting and imaging, and lead them exactly to the place in the body that is the goal of treatment. At the same time, one can reduce the side effects that usually occur in the parts of the body that are not targets for treatment.

Nanoparticles are of a size that can penetrate into cells. Their surface functionalization offers a way to increase their sensitivity when detecting target molecules. In addition, it increases the potential for flexibility in particle design, their therapeutic function, and variation possibilities in diagnostics. Mesoporous nanoparticles of amorphous silica have attractive physical and chemical characteristics such as particle morphology, controllable pore size, and high surface area and pore volume. Additionally, the surface functionalization of silica nanoparticles is relatively straightforward, which enables optimization of the interaction between the particles and the biological system.

The main goal of this study was to prepare traceable and targetable silica nanoparticles for medical applications with a special focus on particle dispersion stability, biocompatibility, and targeting capabilities.

Nanoparticle properties are highly particle-size dependent and a good dispersion stability is a prerequisite for active therapeutic and diagnostic agents. In the study it was shown that traceable streptavidin-conjugated silica nanoparticles which exhibit a good dispersibility could be obtained by the suitable choice of a proper surface functionalization route.

Theranostic nanoparticles should exhibit sufficient hydrolytic stability to effectively carry the medicine to the target cells after which they should disintegrate and dissolve. Furthermore, the surface groups should stay at the particle surface until the particle has been internalized by the cell in order to optimize cell specificity. Model particles with fluorescently-labeled regions were tested *in vitro* using light microscopy and image processing technology, which allowed a detailed study of the disintegration and dissolution process. The study showed that nanoparticles degrade more slowly outside, as compared to inside the cell.

The main advantage of theranostic agents is their successful targeting *in vitro* and *in vivo*. Non-porous nanoparticles using monoclonal antibodies as guiding ligands were tested *in vitro* in order to follow their targeting ability and internalization. In addition to the targeting that was found successful, a specific internalization route for the particles could be detected. In the last part of the study, the objective was to clarify the feasibility of traceable mesoporous silica nanoparticles, loaded with a hydrophobic cancer drug, being applied for targeted drug delivery *in vitro* and *in vivo*. Particles were provided with a small molecular targeting ligand. In the study a significantly higher therapeutic effect

could be achieved with nanoparticles compared to free drug. The nanoparticles were biocompatible and stayed in the tumor for a longer time than a free medicine did, before being eliminated by renal excretion. Overall, the results showed that mesoporous silica nanoparticles are biocompatible, biodegradable drug carriers and that cell specificity can be achieved both *in vitro* and *in vivo*.

Referat

Individuellt skräddarsydd nanomedicin har visat sig ha fördelar jämfört med traditionell klinisk bildåtergivning, diagnos och konventionell medicinsk behandling. Med hjälp av nanopartiklar kan man effektivisera och precisera målsökningen och bildåtergivningen för de ämnen som är viktiga för den kliniska behandlingen och leda dem exakt till det ställe i kroppen som är målet för behandlingen. Samtidigt kan man minska de biverkningar som vanligtvis åsamkas de delar av kroppen som inte är mål för behandling.

Nanopartiklar har en sådan storlek att de kan tränga sig in i celler. Funktionalisering av dem erbjuder ett sätt att öka känsligheten när man detekterar mål-molekylerna. Dessutom ökar möjligheterna till flexibilitet i partiklarnas design, deras terapeutiska funktion och variationsmöjligheterna i diagnostiken. Mesoporösa nanopartiklar av amorf kiseldioxid har attraktiva fysikalisk-kemiska särdrag såsom en kontrollerbar partikelmorfologi och storlek samt hög ytareal och porvolym. Dessutom kan kiseldioxidnanopartiklarna relativt lätt ytfunktionaliseras, vilket möjliggör optimering av växelverkningarna mellan partiklarna och det biologiska systemet.

Det huvudsakliga målet för denna studie har varit att tillverka spårbara och målsökande kiseldioxidbaserade nanopartiklar för medicinska tillämpningar med speciell fokus på partiklarnas dispersionsstabilitet, biokompatibilitet och målsökningsförmåga.

Nanopartiklarnas egenskaper är mycket beroende av partikelstorleken och en god dispersionsstabilitet är en förutsättning för ett aktivt terapi- och diagnosmedel. I studien visades att spårbara streptavidinkonjugerade kiseldioxid nanopartiklar och vilka uppvisar en god dispergerbarhet kunde erhållas genom ett lämpligt val av ytfunktionaliseringsrutt.

Teranostiska nanopartiklar bör uppvisa en tillräckligt för att effektivt kunna bära läkemedel till målcellerna varefter de bör sönderfalla och upplösas. Dessutom bör ytgrupperna hållas på partikelytan tills partikeln har blivit internaliserad av cellen för att optimera cellspecifiteten. Modellpartiklar med fluorescent märkta regioner undersöktes *in vitro* med hjälp av ljusmikroskopi och bildbehandlingsteknik, vilket möjliggjorde en detaljerad studie av sönderfalls- och upplösningsprocessen. Studien visade att nanopartiklarna sönderfaller långsammare utanför jämfört med innanför cellen.

Den främsta fördelen med teranostiska preparat är deras lyckade målsökning *in vitro* och *in vivo*. Icke-porösa nanopartiklar som använde monoklonala antikroppar som guidningsmedel undersöktes *in vitro* för att följa deras målsökningsförmåga och internalisering. Förutom att målsökningen konstaterades framgångsrik, kunde en specifik internaliseringsrutt för partiklarna påvisas. Slutligen undersöktes möjligheten att använda spårbara mesoporösa kiseldioxidnanopartiklar laddade med en hydrofob cancermedicin för målsökande

läkemedelsfrisättning *in vitro* och *in vivo*. Partiklarna försågs med en småmolekylär målsökande ligand. En klart högre terapeutisk effekt kunde uppnås med nanopartiklarna jämfört med fri drog. Nanopartiklarna var biokompatibla och stannade i tumören en längre tid än en fri medicin, innan de eliminerades genom utsöndring via njurarna. Sammantaget visar resultaten att mesoporösa kiseldioxid nanopartiklar är biokompatibla, biodegraderbara läkemedelsbärare och att cellspecifitet kan uppnås såväl *in vitro* som *in vivo*.

Contents

Abstract	4
Referat	6
List of original publications	10
Symbols and abbreviations	12
Introduction	15
Background	17
1. Sol-gel synthesis for fabrication of non-porous and porous silica nanoparticles	17
2. Particle synthesis through sol-gel silica polymerization	20
2.1. Synthesis of mesoporous silica through template self-assembly	23
2.2. Alkaline synthesis pathway $S^{+}I^{-}$ is favored to obtain monodisperse mesoporous nanoparticles	25
2.3. Surfactant packing	26
2.4. Methods for template removal	26
2.5. Nanoparticle size, surface properties and dispersion stability	28
2.6. Surface chemistry of silica	30
2.7. Functionalization of the silica surface	31
2.7.1. Direct functionalization by co-condensation	32
2.7.2. Postsynthetic functionalization of silica by grafting	33
2.7.3. Surface polymerization	35
2.8. Standard bioconjugation strategies	37
2.8.1. Zero-length cross-linkers	37
2.8.2. Cross-linkers	38
2.8.3. Streptavidin-biotin interaction	40
3. Nanoparticles for molecular imaging	41
3.1. Fluorescently-labeled silica nanoparticles	41
4. Receptor-mediated uptake of nanoparticles	44
4.1. Active targeting	44
4.1.1. Antibodies as targeting ligands	45
5. Drug incorporation and release	48
6. Silica biodegradation	50
Characterization techniques	53
7. Small angle x-ray diffraction	54
8. Nitrogen physisorption	57
8.1. Porosity and classification of pores	57
8.2. The physisorption isotherms	57
9. Electrokinetic zeta potential measurements	61
9.1. Determination of zeta potential by electrophoretic light scattering	62
10. Dynamic light scattering	64

11.	Electron microscopy.....	66
11.1.	Transmission electron microscopy	66
11.2.	Scanning electron microscopy.....	66
12.	Confocal microscopy.....	68
13.	Flow cytometry.....	70
Summary of the results		71
14.	Article I.....	71
14.1.	Construction of the model particle.....	71
14.2.	Summary of the results.....	75
15.	Article II.....	76
15.1.	Construction of the model particle.....	76
15.2.	Characterization by the set of standard techniques.....	77
15.3.	Local pH correlates to the fluorescence intensity of the highly pH dependent fluorescein isothiocyanate.....	78
15.4.	Evaluation of the particle degradation <i>in vitro</i>	79
15.4.1.	Segmentations.....	80
15.4.2.	Co-localizations.....	81
15.5.	Summary of the results.....	83
16.	Article III.....	84
16.1.	Construction of the model particle.....	84
16.2.	Characterization by the set of standard techniques.....	84
16.3.	Targeting of the particles <i>in vitro</i>	85
16.3.1.	Flow cytometry.....	85
16.3.2.	Confocal microscopy and image analysis.....	85
16.4.	Summary of the results.....	90
17.	Article IV	91
17.1.	Construction of the particles.....	91
17.2.	Characterization by the set of standard techniques.....	91
17.3.	Targeting of the prepared particles <i>in vitro</i>	93
17.3.1.	Flow cytometry.....	93
17.3.2.	Luciferase-based reporter assay	94
17.4.	Targeting enhances tumor penetration and retains MSNs at the tumor site <i>in vivo</i>	95
17.4.1.	Peritumoral injections.....	95
17.5.	GSI-loaded MSNs show enhanced Notch inhibition as compared to a free drug <i>in vivo</i>	97
17.5.1.	Peritumoral injections.....	97
17.6.	Evaluation of the biocompatibility of MSNs administered through the intravenous and peritumoral routes	97
17.7.	Summary of the results.....	102
Conclusions and outlook		103
Acknowledgements		105
References		106

List of original publications

The thesis is based on the following four original publications, hereafter referred to by the Roman numerals I–IV. The original publications are reproduced with the permission of the copyright owners.

- I. L. Bergman, J.M. Rosenholm, A.-B. Öst, A. Duchanoy, P. Kankaanpää, J. Heino, M. Lindén, On the Complexity of Electrostatic Suspension Stabilization of Functionalized Silica Nanoparticles for Biotargeting and Imaging Applications. *J. Nanomater., Special Issue "Nanostructured Materials for Biomedical Applications"*, 2008. doi: 10.1155/2008/712514
- II. L. Bergman, P. Kankaanpää, S. Tiitta, A. Duchanoy, L. Li, J. Heino, M. Lindén, Intracellular Degradation of Multi-labelled Poly(Ethylene imine)-Mesoporous Silica–Silica Nanoparticles – Implications for Drug Release. *Mol. Pharmaceutics*, 2013, 10, 1795–1803. doi: 10.1021/mp3005879
- III. P. Kankaanpää, S. Tiitta, L. Bergman, A.-B. Puranen, M. Lindén, J. Heino, Cellular Recognition and Macropinocytosis-like Internalization of Nanoparticles Targeted to Integrin Alpha 2 Beta 1. *Submitted manuscript*.
- IV. V. Mamaeva, J.M. Rosenholm, L.T. Bate-Eya, L. Bergman, E. Peuhu, A. Duchanoy, L.E. Fortelius, S. Landor, D.M. Toivola, M. Lindén, C. Sahlgren, Mesoporous Silica Nanoparticles as Drug Delivery for Targeted Inhibition of Notch Signalling in Cancer. *Mol. Ther.*, 2011, 19 (8), 1538–1546. doi: 10.1038/mt.2011.105

List of Supporting Publications

- v. M. Karesoja, J. McKee, E. Karjalainen, S. Hietala, L. Bergman, M. Lindén, H. Tenhu. Mesoporous Silica Particles Grafted with Poly(ethyleneoxide-block-N-vinylcaprolactam). *J. Polym. Sci., Part A: Polym. Chem.* 2013, 51, 5012–5020. doi: 10.1002/pola.26928
- vi. R. Wittig, J.M. Rosenholm, E. von Haartman, J. Hemming, F. Genze, L. Bergman, T. Simmet, M. Lindén, C. Sahlgren, Active Targeting of Mesoporous Silica Drug Carriers Enhances γ -Secretase Inhibitor Efficacy in an *in vivo* Model for Breast Cancer. *Nanomedicine* 2014 9(7), 971–987. doi: 10.2217/nnm.13.62

- vii. J. Zhang, W. Sun, L. Bergman, J.M. Rosenholm, M. Lindén, G. Wu, H. Xu, H.-C. Gwa. Magnetic mesoporous silica nanospheres as DNA/Drug carrier. *Mat. Lett.*, 2012, 67(1), 379-382. doi: 10.1016/j.matlet.2011.09.086
- viii. B. Ufer, J.M. Rosenholm, A. Duchanoy, L. Bergman, M. Lindén. Poly(ethylene imine) functionalized mesoporous silica nanoparticle for biological applications. *Stud. Surf. Sci. Catal.*, 2008, 1, 353-356. doi:10.1016/S0167-2991(08)80215-7

Contribution of the Author

The author is responsible for the experimental work in this thesis, with the following exceptions.

Paper I

TEM images were taken by Markus Peurla at Electron Microscopy, University of Turku. Anna-Brita Öst and Pasi Kankaanpää carried out the confocal imaging studies.

Paper II

In vitro experiments followed by confocal imaging was carried out by Pasi Kankaanpää and Silja Tiitta. The dissolution tests were conducted by Ling Li.

Paper III

The flow cytometry was carried out by Eva von Haartman and Anna-Brita Öst. Pasi Kankaanpää and Silja Tiitta were responsible for the *in vitro* experiments followed by confocal imaging studies and image analysis.

Paper IV

The particle synthesis was carried out in collaboration with Jessica Rosenholm. Veronika Mamaeva was responsible for the *in vivo* tests. Laurel Tabe-Eya, Emilia Peuhu and Sebastian Landor carried out the *in vitro* tests. Alain Duchanoy conducted the particle dissolution tests.

Symbols and abbreviations

α_{OH}	Amount of surface silanols (in $\mu\text{mol}/\text{m}^2$ or nm^2)
Γ	Surface excess
ζ	Zeta potential
θ	Scattering angle
κ^{-1}	Thickness of the diffuse layer
Ψ_0	Surface potential
AFM	Atomic Force Microscopy
APTS	(3-Aminopropyl)triethoxysilane
APTMS	(3-Aminopropyl)trimethoxysilane
BET	Brunauer-Emmett-Teller theory for surface area determination
BJH	Barrett-Joyner-Halenda for pore size determination
CPP	Critical Packing Parameter (of surfactants)
CTAB	Cetyltrimethylammonium bromide
CTAC	Cetyltrimethylammonium chloride
d	Diameter of a sphere
Da	Dalton
DAPT	A hydrophobic substance used for the treatment of various types of cancers, ($\{\text{N}-[\text{N}-(3,5\text{-Difluorophenacetyl})\text{-L-alanyl}]\text{-S-phenylglycine-t-butyl ester}\}$)
DCC	N,N'-dicyclohexylcarbodiimide
DLS	Dynamic Light Scattering
FA	Folic Acid
FITC	Fluorescein isothiocyanate
GA	Glutaraldehyde
GSI	Gamma Secretase Inhibitor
EDC	1-Ethyl-3-(3-(dimethylamino)propyl)-carbodiimide
<i>ex vivo</i>	from latin: "out of the living"
EPR	Enhanced Permeability and Retention (effect on the tumor site)
HEPES	2-[4-(2-hydroxyethyl)piperazin-1-yl]ethanesulfonic acid buffer
IEP	Isoelectric point
<i>in vitro</i>	from Latin: "in living", <i>i.e.</i> under physiological conditions
<i>in vivo</i>	from Latin: "in glass", <i>i.e.</i> under simulated physiological conditions
i.v.	intravenous
IUPAC	International Union of Pure and Applied Chemistry
K_{D}	Dissociation constant
M41S	The family of mesoporous materials introduced by Mobil Oil
MAB	Monoclonal Antibody

MCM-41	2-dimensional hexagonally ordered (p6m) mesoporous silica material synthesized with cationic surfactants as structure-directing agents, first reported by a research group at the Mobil Oil Company, USA
MCM	Mobil Composition of Matter
MES	Morpholinoethanesulfonic acid buffer
NIR	Near Infrared
NHS	N-hydroxysuccinimide
NLDFT	Non-local density functional theory
MRI	Magnetic resonance imaging
MSN	Mesoporous silica nanoparticle
NMR	Nuclear magnetic resonance
PEG	Polyethyleneglycol
PEI	Poly(ethyleneimine)
PET	Positron Emission Tomography
pK _a	Acidity constant
p.t.	peritumoral
PZC	Point of zero charge
RT	Room temperature (298 K)
ROI	Region of Interest (in confocal imaging)
SAOS-2 cells	Human sarcoma osteogenic cells
SAXS/SAXD	Small Angle X-ray Scattering/ Small Angle X-ray Diffraction
scFv	Single-chain Fragment variable (antibody)
SEM	Scanning electron microscopy
SBF	Simulated Body Fluid
STV	Streptavidin
SUCC	Succinic acid
SSA	Specific Surface Area per unit of mass
Sulfo-NHS	N-hydroxysulfosuccinimide
Sulfo-SMCC	Sulfo-succinimidyl-(4-N-maleimidomethyl) cyclohexane-1-carboxylate
TEM	Transmission electron microscopy
TEOS	Tetraethyl orthosilicate
TMB	Trimethylbenzene
TMOS	Tetramethyl orthosilicate
TRITC	Tetramethylrhodamine-5-(and 6)-isothiocyanate
U _e	Electrophoretic mobility
PBS	Phosphate buffered saline
RES	Reticulo-endothelial system
XRD	X-Ray Diffraction

Introduction

Personalized nanomedicine aims on developing tailored approaches to disease prevention and care. Nanomedicine has paved a way for improved disease treatment strategies enabling targeted imaging, diagnosis, and treatment.

Nanoparticles have size that matches the scale of the molecular substrates of personalized medicine;¹ their functionalization provides a way for increased sensitivity in detecting and binding with target molecules, and flexibility in the design and function of therapeutics and diagnostics. Theranostic nanoparticles can be utilized diagnostically to assess the disease status, molecular profile, and treatment response, all having influence on the treatment strategies. Silica nanoparticles have high potential to be used for theranostics due to their exceptional features and good biocompatibility.^{2–6} Recently silica nanoparticles “Cornell dots” got approval from US Food and Drug administration (FDA) for the first in human clinical trial for targeted molecular imaging of cancer.⁷

A flexible nanosized drug carrier platform consists of a general toolbox that is employed to design a drug delivery system for a defined purpose. The prerequisites for a flexible drug-delivery platform include a) the option of diverse surface functionalization, b) a high cell specificity and efficient cellular uptake, c) a low degree of premature leakage and the possibility for sustained and controlled release of the drug, d) a low cytotoxicity of the carrier matrix itself, e) the ability to incorporate therapeutically sufficient amounts of drugs into the carrier, f) a good dispersibility of the carrier in biological prevailing conditions, and g) a low level of protein adsorption onto the carrier surface.⁸

The bottom-up approach synthesis of silica nanoparticles enables preparation of nonporous and porous nanocarriers with various particle and pore diameters and narrow particle size distribution. Mesoporous silica nanoparticles can be synthesized with high specific pore volumes and surface areas of 0.6–1 cm³/g and 700–1000 m²/g, respectively.

The relatively straightforward functionalization of silica surface allows preparation of material with diverse surface chemistries allowing the particles to be readily adapted for specific applications. Silica nanoparticles can be functionalized to facilitate their targeting to specific sites, tracing, and to enable triggered release of therapeutic agents to target cells. Silica nanoparticles are capable of encapsulating high amounts of contrast agents that effectively increase the sensitivity of imaging modalities to enable imaging at the molecular level.^{9–11} Loading the targeted nanoparticles with therapeutic agents ensures high efficacy on the target site while lessening or eliminating potential off-target side effects.¹² The incorporation of cargo in silica nanoparticles is most often conducted as last step, enabling regulation of the drug concentration in the particles. This loading procedure is especially applicable for often poorly water-soluble cancer drugs.

Moreover, amorphous silica is biocompatible, dissolves in aqueous solutions and is actively degraded by cells. The material properties of silica allow regulation of carriers' degradation profile in such a way that enables surface functionalities to stay attached to particle the times relevant for the particles' reaching their target sites. The requirement for a good biocompatibility is degradation and excretion of the carrier matrix from the body after particles have accomplished their task.^{4,13-19}

Silica nanoparticle platform enables a flexible particle design where features and functionalities can be combined to produce multifunctional delivery systems enabling targeting, drug delivery and diagnostics actions. This thesis evaluates the potential of silica nanoparticles in medical imaging and targeted drug delivery applications.

Background

1. Sol-gel synthesis for fabrication of non-porous and porous silica nanoparticles

The sol-gel method is a one-step procedure to prepare nanosized nonporous and mesoporous silica nanoparticles in low temperatures and in mild chemical conditions with predetermined particle and pore size, and morphology.

In 1968 Stöber *et al.* reported the formation of monodisperse nanoparticles by means of hydrolysis and polycondensation of silicates in alcoholic solutions catalyzed by alkali conditions. Under alkaline conditions silica solubility increases rapidly and Ostwald ripening takes place, which allows well-controlled nucleation and growth rate leading to the synthesis of monodisperse silica particles. Ideally during the synthesis, a short initial burst of nucleation is followed by a uniform growth resulting in the synthesis of homogenous particles. In an alkaline solution silica species are negatively charged, where simultaneous highly diluted reaction conditions are used to avoid the inter-particle aggregation during the particle synthesis. During controlled regulation of conditions such as concentration of ammonia, water, the chosen type of silicon alkoxide, type of alcohol, and reaction temperature, the Stöber synthesis allows production of monodisperse non-porous particles with a diameter ranging from 50 nm to 2 μm .¹

In 1992 Kresge *et al.* at Mobil Oil Research successfully synthesized ordered mesoporous materials by employing isotropic supramolecular surfactant aggregates as structure directing agents (SDAs) around which inorganic material can deposit through hydrolysis and condensation via sol-gel approach, finally forming a mesoscopically-ordered hybrid inorganic material. The original synthesis of Mobil Composition of Matter No 41 or, broader speaking, the M41S family of mesoporous materials is based on the co-operative self-assembly of aluminosilicates or silicates and alkyltrimethylammonium-based cationic surfactants. The procedure principally follows the synthesis of zeolithe molecular sieves, with the exception that instead of using single molecules as templates, supramolecular surfactant structures are used as porogens. The pore size of zeolithes is restricted to about 1.5 nm, while using of supramolecular surfactant structures as structure directing agents allows the synthesis of M41S family of mesoporous materials with a remarkably larger pore size typically ranging from 1.5 to 10 nm. The removal of an organic structure-directing agent by thermal calcination or chemical extraction reveals an ordered pore structure of inorganic silica materials.²

According to the International Union of Pure and Applied Chemistry (IUPAC), mesopores are pores with a diameter ranging from 2–50 nm. The

mesoporous class of the M41S type of material has a well-defined pore size distribution with a pore diameter ranging from 1.5–10 nm and with high surface areas ($\geq 700 \text{ m}^2/\text{g}$). The original members of M41S family consist of Mobil Composition of Matter No 41, MCM-41 with a hexagonal pore structure, of

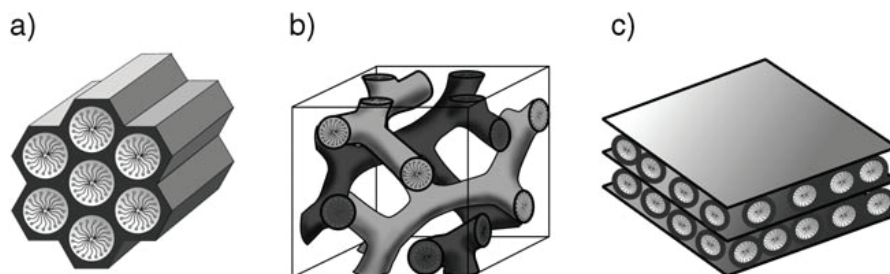


Figure 1. Schematic presentation of the structures of the MCM41S family of mesoporous ordered materials: (A) MCM-41, (B) MCM-48, (C) MCM-50.⁴

MCM-48 type material with cubic pore structure and of MCM-50 type material with pillared lamellar structure (Figure 1). As part of this thesis, MCM-41-type hexagonally ordered nanoparticles were studied.³

Grün *et al.* introduced a mesoporous particle synthesis, which is a modification of the Stöber approach. The synthesis is carried out in alkaline conditions by using alcohol as a co-solvent and aqueous ammonia as a catalyzing agent. Grün *et al.*, moreover, used cationic quaternary ammonium surfactants similar to the original M41S type of synthesis to synthesize the mesoporous MCM-41 type particles located in the sub-micrometer size class.⁵ Furthermore, Cai *et al.* and Nooney *et al.* reported the importance of controlled nucleation and growth of the particles during synthesis. This could be achieved by applying lower surfactant concentrations in alkaline conditions for the synthesis of MCM-41 type material leading to a defined particle morphology and a size of less than 100 nm.^{6–8} Generally, the synthesis of monodisperse silica nanoparticles has proved to require alkaline synthesis conditions, thus following the principles of the original Stöber synthesis. These selected examples indicate that mesoporous silica synthesis is highly dependent on reaction conditions but is very versatile with respect to particle size, for example, allowing synthesis of mesoporous particles in the size range of tens of nanometers up to several micrometers.

Silica is a very versatile material also allowing synthesis of various nanoparticle types, those consisting of intrinsic silica and those consisting of silica composite materials. Already as early as in the 1970's and 1980's, the studies of Matijević *et al.* demonstrated the synthesis of core-shell type colloids.⁹ Caruso *et al.* introduced the principles of colloidal templating to prepare hollow

silica spheres in 1998.¹⁰ As the particle size is crucial in theranostics, efforts have been undertaken to develop the particle synthesis in the direction enabling preparation of core-shell, hollow and enlarged-pore particles in nanosize. These extraordinary particle features provide a benefit of increased loading capacity of therapeutic agents, enabling loading of high molecular size cargos such as genes and proteins for example.^{11,12} However, generally many aspects in the particle synthesis of silica nanoparticles are still not well understood and need further research and optimization.

2. Particle synthesis through sol-gel silica polymerization

In the sol-gel synthesis process the polymerization of silica proceeds in three steps. These steps are nucleation, growth, and aggregation.

1. With particle formation by polymerization and nucleation, silica monomers polymerize via dimers, trimers, etc. and will further form cyclic structures and reach the 3D form of condensed particles.
2. Particle growth and Ostwald ripening follows.
3. Particles aggregate into branched chains and networks leading to the forming of a gel.

The condensation process proceeds by first maximizing the number of Si-O-Si bonds and resulting in the number of terminal hydroxyl groups being minimized by internal condensation. This condensation includes a rapid ring-formation into which the monomers further bind, leading to the formation of three-dimensional small particles. These formed particles are compact and have OH- groups only on the particle surface. The further growth of the particles proceeds through Ostwald ripening resulting in particle size growth since particles diminish in numbers when smaller particles dissolve into monomers that then re-deposit on the larger less soluble particles. Both pH and the temperature have an effect on the progress of particle growth. An overview of the polymerization process of silica in an aqueous solution can be seen in Figure 2.

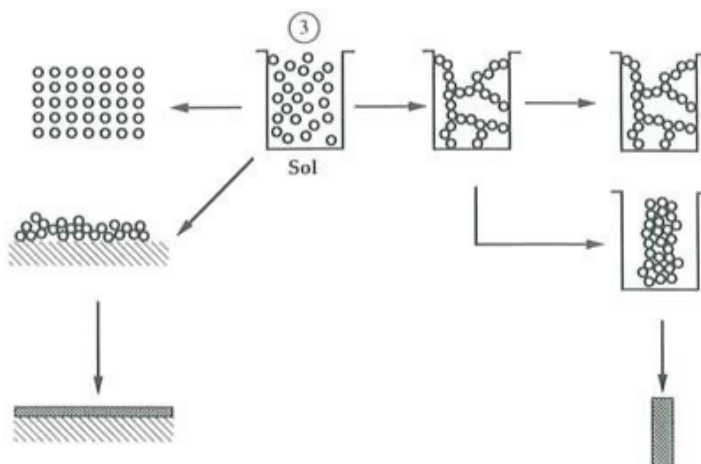
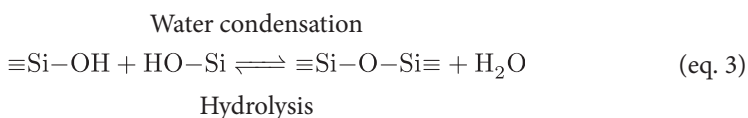
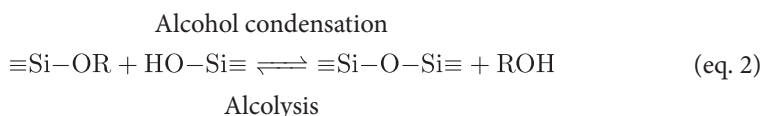
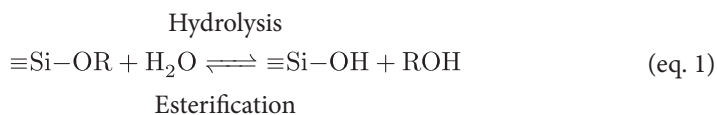


Figure 2. An illustration of the sol-gel process.¹³

The sol-gel process can be described by three equilibrium reactions (where R is an alkyl group).



In the hydrolysis reaction (eq. 1) alcoxide groups are replaced by hydroxyl groups. Hydrolysis is generally catalyzed by a base (NH_3 , NaOH) or mineral acid (HCl). In the subsequent condensation reactions siloxane bonds ($\text{Si}-\text{O}-\text{Si}$) are formed and with alcohol (eq. 2) and water (eq. 3) formed as by-products. Because water and alkoxy silanes are immiscible, alcohol is often used as the homogenizing agent. The relative kinetics of the three equilibrium reactions involved is regulated by several parameters such as pH, the type of silica precursor, $\text{H}_2\text{O}/\text{Si}$ molar ratio (r -value), temperature, co-solvents, and the solubility of silica.

Hydrolysis reaction-rate retardation is observed when the silicon alkoxide precursor molecular size is increased. This is caused by steric hindrance (spatial effects) and seen notably in branched, bulkier precursors. During the hydrolysis, inductive effects become important. This is result of both hydrolysis (substitution of $-\text{OH}$ or $-\text{OR}$) and condensation (substitution of $-\text{OSi}$ for $-\text{OR}$ or $-\text{OH}$) decreasing the electron density of silicon, which in turn increases the stability of negatively-charged transition states. This means that in acidic conditions the hydrolysis rate will decrease with each subsequent hydrolysis and condensation step but increase under basic conditions due to the enhanced electron-withdrawing capabilities of $-\text{OH}$ compared to $-\text{OR}$ groups.

According to the illustration in Figure 3, the overall reaction proceeds as a poly-condensation to form soluble, higher molecular weight polysilicates. This colloidal dispersion is the sol. The polysilicates can link together to form a three-dimensional network filled with solvent molecules and spanning the container, called the gel or precipitate, as silica. Sol-gel polymerization proceeds in several possibly overlapping steps, which are monomer polymeriza-

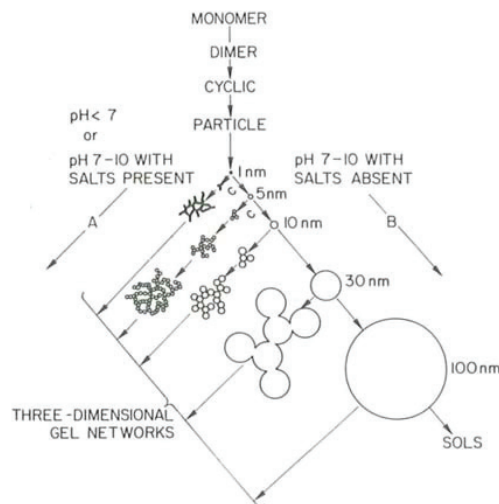


Figure 3. Polymerization behavior of silica. In basic conditions (B) particles grow in size with a decrease in number. In acidic conditions (A) or in the presence of flocculating salts, particles form aggregates and three-dimensional networks, gels.¹⁴

tion to form primary particles, growth of the particles, and the aggregation. Sol-gel reaction is highly dependent on the reaction conditions including pH, temperature, concentration, and co-solvent. However, hydrolysis and condensation reactions depend most strongly on the nature and the concentration of the catalysts, resulting in strong pH dependence.

Based on the difference in the polymerization process related to the prevailing pH, three pH domains can be separated, $\text{pH} < 2$, $\text{pH} = 2\text{--}7$, and $\text{pH} > 7$. The value $\text{pH} 2$ corresponds approximately to the isoelectric point of silica, IEP (electrical mobility of silica particles here equals to zero) and the point of zero charge, PZC (surface charge here is zero). Below $\text{pH} 2$ the silicate species are positively charged. At pH values < 2 the solubility of silica is relatively low and gel times are long (Figure 4). Here the rate of polymerization is proportional to the concentration of $[\text{H}^+]$ ions. At $\text{pH} 7$ there is a boundary since above this value solubility of the silicates increases strongly. Silica species are negatively charged and hereby stabilized leading preferentially to the growth of large particles instead of aggregation to a gel.¹⁴

The effect of pH is critical. In a basic solution where most of the nanoparticle synthesis occurs, the hydrolysis rate of TEOS increases with the increase of pH, while the condensation rate of TEOS is not monotonic. The highest condensation rate is around $\text{pH} 8.4$ and decreases when the pH value is below or above 8.4. There is no proportional relation between the particle size and the applied pH value.

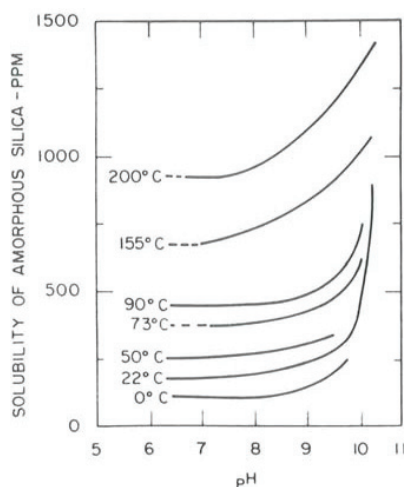


Figure 4. Solubility of amorphous silica as a function of pH at different temperatures.¹³

2.1. Synthesis of mesoporous silica through template self-assembly

Ordered mesoporous silica materials form through the self-assembly process of silica species with surfactant structures. During the mesoporous silica synthesis, the prerequisite for mesophase formation is an attractive interaction between the head group of structure directing agent and the silica precursor through electrostatic, counter-ion mediation or hydrogen-bonding interactions.

The first four reaction pathways described in Figure 5a–d are of an electrostatic nature. If the synthesis takes place under alkaline conditions and cationic quaternary ammonium surfactants are used as the SDA, silicate species are present as anions, and the synthesis pathway is termed S^+I^- (Figure 5a), which is the pathway for the M41S-family of materials. When the synthesis takes place under acidic conditions (below IEP of Si–OH bearing species, $pH \approx 2$) and cationic quaternary ammonium surfactants are used as the SDA, silicate species are present as cations and a mediator ion is needed to create interactions between those species and the surfactant head group. In this process the synthesis pathway is termed as $S^+X^-I^+$ (Figure 5b). If the synthesis takes place under alkaline conditions and anionic surfactants (e.g., long-chain alkyl phosphates) are used as the SDA, the silicate species are present as anions and a mediator ion is again needed. In this latter process the synthesis pathway is termed $S^-M^+I^-$ (Figure 5c). Conversely, a mediator ion is not required in acidic media, the synthesis S^-I^+ pathway (Figure 5d).

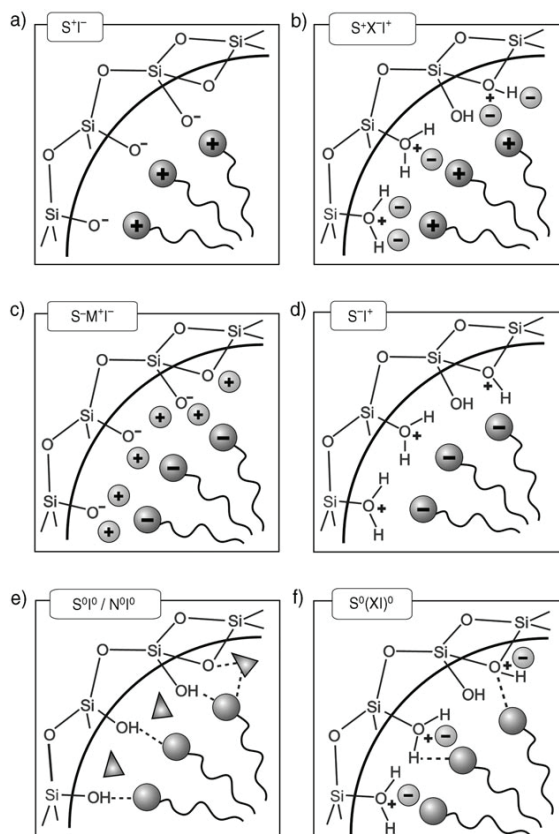


Figure 5. Interaction between the surfactant head group and inorganic silica enables synthesis of mesoporous material in acidic, basic, or neutral synthetic conditions. Electrostatic interactions: S^+I^- , $S^+X^-I^+$, $S^-M^+I^-$, $S-I^+$; through hydrogen bonds: S^0I^0/N^0I^0 , $S^0(XI)^0$. (S: surfactant, I: inorganic species, X: mediator ion, which is usually a halide).⁴

In the last two reaction pathways presented in Figures 5e–f, the attractive interaction between the nonionic SDA (e.g., S^0 : a long-chained amine; N^0 : polyethylene oxide) and the silica species are created through hydrogen bonding. If silica is present as uncharged silica species, the reaction pathway is termed S^0I^0 (Figure 5e). When silicate is present as ion pairs, the reaction pathway is termed $S^0(XI)^0$ (Figure 5f).⁴

2.2. Alkaline synthesis pathway S^+I^- is favored to obtain monodisperse mesoporous nanoparticles

To attain highly monodisperse particles, a short initial burst of nucleation is favored, followed by a uniform growth resulting in the synthesis of homogenous particles. As stated above, the reaction pathway S^+I^- (Figure 5a) is the pathway for the M41S-family of materials. Alkaline and diluted conditions are typically used to synthesize negatively-charged particles to avoid inter-particle aggregation.

Generally monodisperse particles are obtained by template-directed alkaline synthesis and by using very dilute silane concentrations or by the addition of particle growth quenchers. The use of a particle growth quencher is interesting as higher product yields can be obtained and higher particle concentrations can be reached before aggregation occurs, which leads to more easily scalable nanoparticle syntheses. Different mechanisms for synthesis in alkaline conditions related to reaction conditions have been employed, such as dilution together with pH quenching,^{17,18} dilute conditions together with water and EtOH as co-solvent,⁶ pH adjustment,¹⁹ or mere dilute conditions.^{20,21} Similarly high alkaline conditions with a wide range of reactants have proved to enable particle size control such as in case of non-ionic polymers or polymers,^{22–25} fluorocarbon-based cationic surfactants,²⁶ triethanolamine,^{27,28} and propanetriol,²⁹ for example. Recently, Yamaha *et al.* reported a facile size control of MSNs realized by using tetraalkoxysilanes with different alkoxy groups ($Si(OR)_4$; R=Me, Et, Pr, and Bu) as silica sources. The average particle size could be controlled in the range of 20–80 nm, which can be explained by the different hydrolysis rate of the tetraalkoxysilanes (longer alkyl chain leads to lower hydrolysis rate).¹⁷⁸ Experiments have shown that organosilanes together with TEOS in the reaction mixture lead to a smaller particle size compared to using TEOS only as a source of silica. These findings indicate that functional silanes can be used as size quenchers. The addition of organosilane can, alternatively, affect the nucleation process and lead to a larger number of formed nuclei, *i.e.* a larger number of nuclei are formed and a smaller particle size is obtained.

There are very few mesoporous silica nanoparticle syntheses reported as being carried out under acidic conditions, where the nucleation and particle-growth kinetics is hard to control. However, one of the advantages of acidic conditions is the capability of using non-ionic block copolymers as porogens, which allows the formation of larger mesopores (>5 nm). Particle size in acidic conditions has been controlled by using size quenching with a cationic fluorocarbon surfactant²⁶ and by the addition of salts to varying amount of water,³⁰ for example.

2.3. Surfactant packing

The formation of the inorganic-organic mesophase is a co-operative process, where all interactions including solvent–silicate, solvent–surfactant, surfactant–surfactant, surfactant–inorganics, and inorganics–inorganics are important. Surfactant packing properties can be estimated based on the critical packing parameter (CPP) or surfactant number, which relates the effective head group area a_0 , the critical chain length l_{max} (normally 80–90% of the fully extended hydrocarbon chain) and the volume of the hydrocarbon chains v .

$$CPP = \frac{v}{l_{max}a_0} \quad (\text{eq. 4})$$

The CPP value gives an approximation of the curvature of the formed liquid crystals, thereby predicting the shape of the micelle. A larger head group (Figure 7) in relation to the tail group leads into a higher curvature *i.e.* to small CPP values (<0.5) indicating structures of spherical or rod-like micelles. A high CPP value (>0.5) gives an anticipation of flat interfaces such as with flexible and planar bilayers having zero curvature. A CPP value of one indicates the formation of inverse micelles.³¹ Figure 6 is an illustration of CPPs corresponding to surfactant self-assembly during synthesis.³² Although the CPP value gives an anticipation of the surfactant self-assembly, experimental conditions such as pH, ionic strength and temperature have a strong effect on the hydrophilic–lipophilic balance. For instance, the effective head group area a_0 can be decreased by the presence of an electrolyte, as this leads to a decrease in the electrostatic repulsion by reducing the electrical double layer between the head groups. In addition, using pore-swelling agents can control the structure of the micelles. A swelling agent such as the widely-used 1,3,5-trimethylbenzene (TMB) is a non-polar molecule that is largely located within the hydrophobic core of micelles in aqueous solution, thereby increasing the micellar diameter and thus the pore size of the final product.^{33,34}

2.4. Methods for template removal

After the silica network has reached a sufficient degree of condensation, the templating molecules are no longer needed and can be removed to open the porous structure. Since most composite mesoporous materials of this type contain as much as 45–55 wt-% of organic material, the template removal process is very important for material preparation.^{36,37} The template can be removed either by calcination or by solvent extraction. Other surfactant removal processes include plasma extraction, supercritical fluid extraction,³⁸ and ozone treatment.³⁹

In calcination the as-synthesized dried materials are typically heated in air,

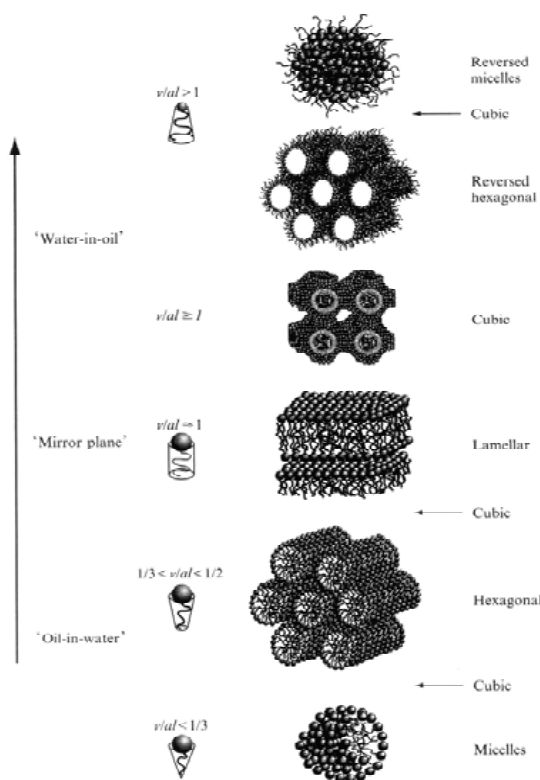


Figure 6. Critical packing parameters (CPPs) of surfactants with various features and their preferred micellar aggregate structures.³²



Figure 7. (On the left) Large head groups of surfactants provoke high surface curvature, (On the right) while surfactants with large hydrophobic chain volume and relatively small head groups creates micellar structure with small surface curvature.³⁵

and by applying heating rates of 1 K/min up to at least 823 K followed by an extended period usually 4–8 h of heating at a temperature plateau.³⁶ The heat treatment leads to contraction of the silica structure, which is, in turn, a result of an increased degree of condensation of the silica network, compared to the as-synthesized material.

The template removal by solvent extraction is carried out by different procedures depending on the synthesis employed. For the M41S-family of materials prepared under basic conditions via the S^+I^- pathway, strong electrostatic interactions exist between the cationic surfactant head groups and the negatively-charged silica network. An ion exchange process by using acids or cationic proton donors is required to remove the template. Commonly utilized extraction procedures for materials prepared in basic conditions involve extraction in acidic ethanol,⁴⁰ or an ethanolic solution of ammonium nitrate,³⁷ where the removal process can be enhanced by a simultaneous sonication treatment and the heating up of the particle dispersion up to 333–343 K during the template removal. The thermal treatment can easily lead to decomposition of organic functions originating from the co-condensation reactions, and thus ion-exchange methods are preferred when co-condensation synthesis is employed.

2.5. Nanoparticle size, surface properties and dispersion stability

Important features of nanoparticles aimed at theranostics are their size and surface properties, both features influencing the particle dispersion stability and the particles' biopharmaceutical properties.

Colloidal nanoscale material has high specific surface to volume ratio, *i.e.* high specific surface area per unit of mass (SSA). The measure is important because many physical and chemical processes take place at the surface of solids. As the percentage of atoms at the surface increase and surface interactions become dominant, the properties of materials change. The chemical and physical properties of nanomaterials may differ significantly from those of the atomic and molecular scale to the bulk materials of the same composition including their magnetic, optical, electric, adsorptive, and catalytic properties for example.⁴¹

Mesoporous silica nanoparticles have a large intraparticular surface that expands the material total SSA in a remarkable manner compared to that of solid nanoparticles. The reactivity of the material increases with the surface area, which is high both for nonporous and mesoporous nanoparticles. With respect to dispersion this is seen as the material aspiration of a decrease of the surface energy by coagulation or aggregation of single particles into larger clusters and by nonspecific interaction with molecules in the surrounding media.

The dispersion properties of silica nanoparticles are determined by the particle size and by surface properties together with the molecular composition of the surrounding media that define the characteristics of the near-surface region. Particle-dispersion stability can be achieved by electrostatic or steric stabilization and is practically attained by proper particle surface functionalization (Figure 8). As the surrounding media interacts with the surface, a high

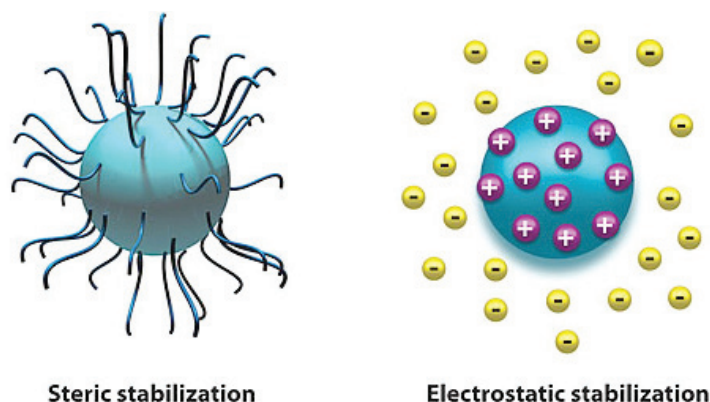


Figure 8. Surface functionalization can provide dispersion stability electrostatically or sterically.⁴⁴

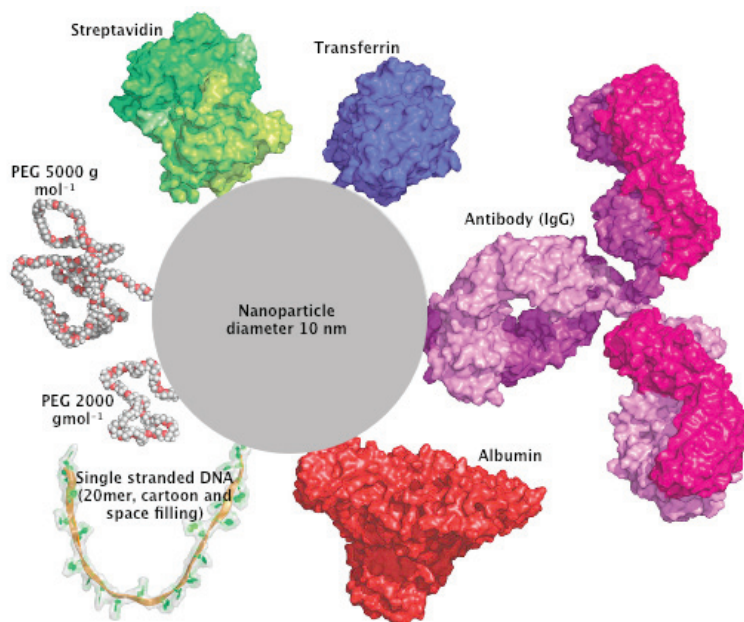


Figure 9. A schematic illustration of the relative size of nanoparticles and biomolecules, drawn to scale.⁴⁵

electrolyte concentration in the physiological environment creates the challenge of reaching stable particle dispersions via the electrostatic route.^{42,43}

Controlled surface functionalization is not only important for ensuring dispersion stability. The theranostic applications of nanoparticles need additional functions, where surface chemistry provides means to attach tracing and targeting agents to the nanoparticles.

2.6. Surface chemistry of silica

Functional groups of an intrinsic-silica surface consist of silanol and siloxane groups. The degree of hydrophilic and hydrophobic properties of the surface depends on the amount of hydroxyl, or silanol (Si-OH) and siloxane (Si-O-Si) groups, covering the surface (Figure 10). The higher the number of silanol groups present on the surface the more hydrophilic the silica surface is. The protonation and deprotonation of the surface silanol groups determine the surface charge of intrinsic silica nanoparticles and the extent of the repulsive energy keeping the particles dispersed in a solution.⁴⁶

Thermal treatment of the material leads to condensation of silanol groups (Si-OH) into siloxane (Si-O-Si) bridges. High calcination temperatures (673–723 K) lead to condensation of unreacted silanol groups after some of the surface groups are lost. Thermal treatment removes water and makes the silica network denser and increases its hydrolytic stability in aqueous solutions. The constitution of silica-surface groups describes directly the thermal history of the material. However, the silica can be re-hydroxylated by boiling calcined particles in water (Figure 11),^{47,52} by acid hydrolysis,⁴⁸ or by steam treatment.⁴⁹ Hydrogen-bonded silanols can be re-activated by thermal treatment, after free active silanols are formed.⁵⁰

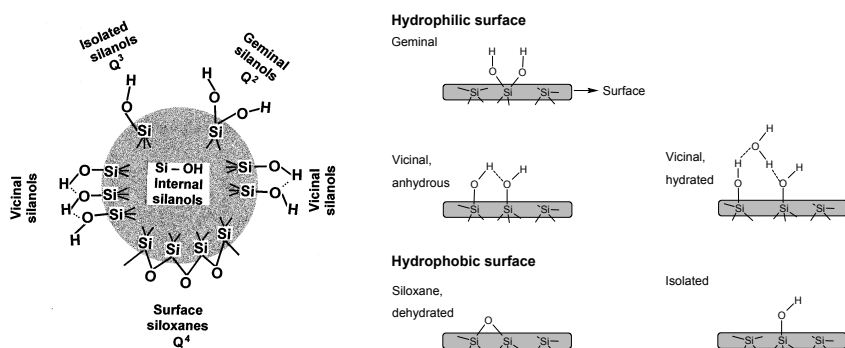


Figure 10. Presented (On the left) are various types of silanol groups and siloxane bridges on the surface of amorphous silica, as well as internal silanol groups.⁵¹ (On the right) the hydrophobicity versus hydrophilicity of the particles is determined by the proportion of various surface groups on the particle surface.⁵⁰

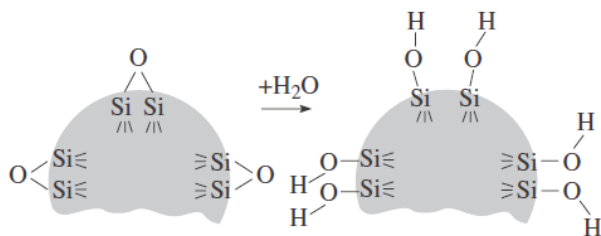


Figure 11. Rehydroxylation of the silica surface by boiling the particles in water can be utilized to create active free silanol groups reactive for further surface functionalization.⁵²

2.7. Functionalization of the silica surface

The possibilities for functionalization of the silica surface are many and often based on the use of functional silanes. The composition of the particle surface determines its interaction with the surrounding media, which in turn has a high impact on the particle-dispersion stability. Tracing and targeting moieties can be conjugated on the particle surface to introduce theranostic features such as those facilitating their specific interaction with cells. The overall composition of the silica surface has a high impact on the pharmacokinetics of the particles in a biological environment.

Mesoporous silica nanoparticles have three topologically distinct regions that can be independently functionalized -the silica framework, nanochannels or pores, and particle exterior. Functional groups of the external surface are more accessible and therefore predominantly functionalized as compared to intraparticular surface groups. To selectively functionalize the outer surface the template removal can be accomplished after the functionalization. Selective functionalization of the intraparticular surface can be done for example by first passivating the outer functional groups, then by functionalizing the inner surface and finally by removing the groups used for passivation (Figure 16).⁵³

The functionalization of inorganic silica through organic moieties combines the advantages of organic functionalities with an inorganic substrate to create hybrid materials. The silica framework provides structural order as well as thermal and mechanical stability while organic species permit versatile control of interfacial and bulk material characteristics such as porosity (e.g. gate-keeping polymers), hydrophobicity, and optical (e.g. fluorophores),^{54–56} electrical (e.g. conducting polymers),^{57–59} or magnetic properties (e.g. organic chelates that allow forming of complexes with magnetic resonance imaging (MRI) contrast agents).^{60,61} Surface functionalization of silica can be carried out by using various methods including covalent binding, chemisorption, electrostatic or hydrophobic interaction. The covalent conjugation is the most stable and selective, and in this study the focus is on covalent functionalization only.

Functionalization of amorphous silica can be accomplished by co-condensation, by post-synthetic grafting “silanization”, or by surface polymerization that includes “grafting to” or “grafting from” methods.^{4,62–64} Functionalization means can also be combined relatively freely, enabling the flexible design of theranostic agents.

2.7.1. Direct functionalization by co-condensation

Co-condensation of tetraalkoxysilanes $[(\text{RO})_4\text{Si}]$ (TEOS or TMOS) with terminal trialkoxyorganosilanes of the type $(\text{R}'\text{O})_3\text{SiR}$ forms Si–C bonds. The approach enables incorporation of a variety of organic groups into the material during the one-pot sol-gel synthesis where organic residues are anchored directly to all particle surfaces (Figure 12).⁴ Furthermore, this method enables the preparation of imageable particles in one step. In practice this is conducted by pre-reacting fluorophore with organosilane (Figure 13), which is subsequently used in the co-condensation synthesis, yielding inherently fluorescent silica nanoparticles. For instance, isothiocyanate group consisting fluorophores, *e.g.* fluorescein isothiocyanate (FITC) or tetramethylrhodamine-5-(and 6)-isothiocyanate (TRITC) can be conjugated with an organosilane primary amino groups and hereby be incorporated directly into the particle network.¹⁵

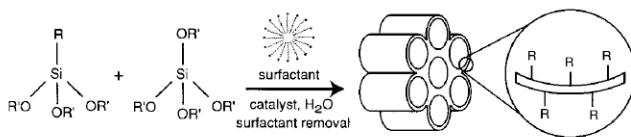


Figure 12. Co-condensation “direct synthesis” method can be employed to modify mesoporous silica phases with organic groups. *R* = organic functional group. It is worth to note that, in contrast to the illustration, the surface consists of both organic groups and silanol groups.⁵³

Since the organic functionalities are introduced during the synthesis stage, pore blocking is not a problem. The organic units are generally more homogeneously distributed in the material compared to material functionalized by a grafting process. However, an increased concentration of organic groups in the network can lead to a decreased degree of mesoscopic order, and a reduction in the pore diameter, pore volume, and specific surface areas. As the co-condensation synthesis includes structurally different precursors having different hydrolysis and condensation rates, there is a change in the tendency of homocondensation reactions and nonhomogeneous distribution of organic functionalities in the framework. Furthermore, as the organic groups are already in-

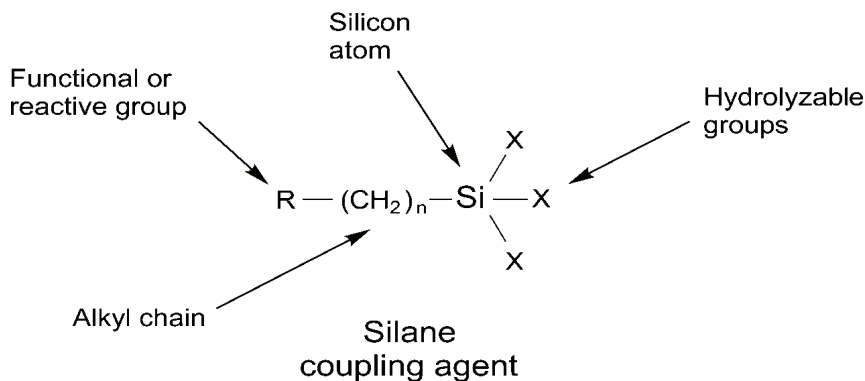


Figure 13. General structure of an organosilane.¹⁵

incorporated into the material during the synthesis, the extraction method must be sensitive so as not to destroy the organic functionality during removal of the surfactant. Commonly only extractive methods can be used.⁴

2.7.2. Postsynthetic functionalization of silica by grafting

In the grafting method “silylation” the surface silanols serve as anchoring groups where both free ($\equiv Si-OH$) and geminal silanols ($=Si(OH)_2$) are responsible for active silylation, while hydrogen-bonded silanol groups are less accessible. The conjugation of surface silanols and organosilanes progresses through simple elimination reactions.⁵⁰ The silanization is often carried out in organic solvents, but the importance of trace water is pointed out in several reports.⁶⁵ The influence of physisorbed water has been emphasized especially in surface modification of aminoalkoxysilanes,^{66–68} while some reports state that the silanization reaction with aminopropylsilanes is self-catalyzed and siloxane bonds are formed also in the absence of water.^{69,70}

The grafting approach for silica was demonstrated already in 1992 by researchers from Mobil Oil where the MCM-41 surface was modified by trimethylsilyl groups.⁷¹ The procedure is carried out primarily by reaction of organosilanes of the type $(R'O)_3SiR$, or less frequently chlorosilanes $ClSiR_3$ or silazanes $HN(SiR_3)_3$. Functionalization with a variety of organic groups can be realized by variation of the organic residue R . Most of the commonly-used organosilanes such as 3-aminopropyltriethoxysilane (APTS) and 3-aminopropyltrimethoxysilane (APTMS) have one organic substituent and three hydrolysable substituents in their molecular structure (Figure 14).¹⁵ In the post-synthetic grafting approach the material is synthesized without disturbance of the organosilanes yielding therefore hydrothermally more stable “compact” mate-

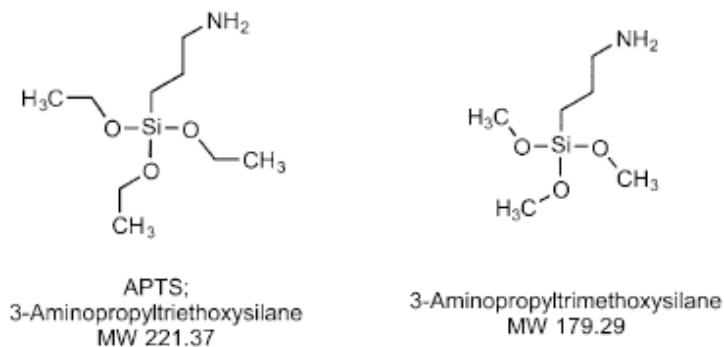


Figure 14. Molecular structures of widely used terminal trialkoxyorganosilanes APTS and APTMS.¹⁵

rial compared to that synthesized via co-condensation approach (Figure 15). However, the grafting method often leads to a heterogeneous surface coverage, where grafting occurs with higher efficiency in pore openings and in a lower quantity on the intraparticular surface.⁷² The functionalization conditions such as the polarity and dielectric constants of solvents have been reported to strongly affect the concentration of grafted organic groups and the degree of their site-isolation.^{72,73} Here, the site-isolation of organic groups is considered to be their sites or locus separated by a sufficient distance to prevent the hydrogen bonding between adjacent groups such as amines, which makes them reactive for further functionalization.

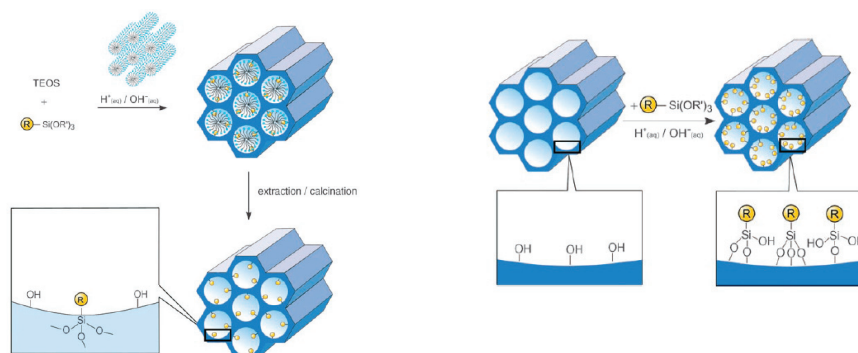


Figure 15. A schematic illustration of co-condensation (on the left) and grafting (on the right).⁴

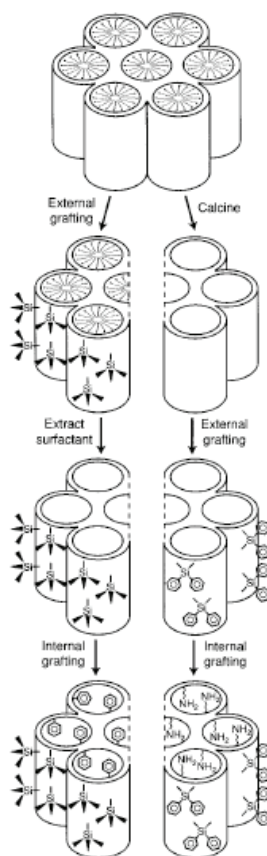


Figure 16. An illustration of selective grafting on external and internal surfaces of mesoporous silica material.⁵³

2.7.3. Surface polymerization

Polymer coating alters the interfacial properties of the particles. Surface polymerization can be used to increase the number of outer functional groups, or “anchoring groups”, to increase particle-suspension stability by providing electrostatically- or sterically-stabilized particle suspensions, or “smart gate-keeper” polymer surfaces, capable of responding to external stimuli such as temperature, pH, or ionic strength.^{74–77} The gate property responds to an external trigger to release the cargo such as drug molecules or imaging agents from the voids of mesoporous particles.

Although polymer adsorption onto a surface is a widely-used means of surface functionalization, in this study only covalent surface polymerization was employed. Covalent grafting involves either “grafting to” or “grafting from” methods. “Grafting to” is maintained through conjugation of reactive macro-

molecules with compatible surface groups. This technique has limitations and can lead to low grafting densities due to steric crowding of reactive sites by previously attached polymers.^{78,79} The “grafting from” method allows a higher control of functionality, density, and thickness of the polymer brushes.^{80,81} A higher grafting density can be achieved by using small monomers not suffering from steric hindrance and having access to the active initiation sites.⁷⁴ A surface-initiated “grafting-from” technique is versatile and allows creation of polymer chains of a “dendritic nature”, which increases the number of outmost functional groups available for further modification.^{75,76}

The hyperbranching ring-opening polymerization of aziridine initiated by silanol groups forms hyperbranched polyethyleneimine-modified particle surfaces leading to highly positively charged particles with increased electrostatic stability in physiological conditions (Figure 17).^{63,76,78} Polyamino functionalized surfaces have also shown to be capable of creating pH controlled gate “open-close” systems, advantageous for smart drug delivery systems (Figure 18).

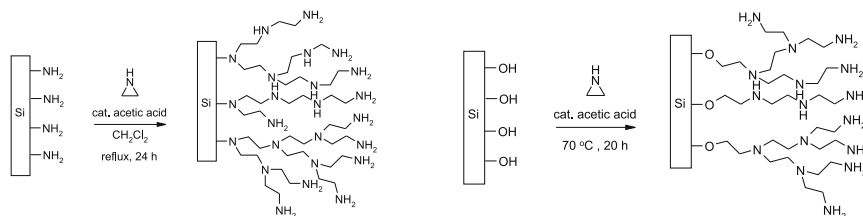


Figure 17. Hyperbranched surface polymerization. Surface grown polyethyleneimine (on the left) grown from amino groups (on the right) grown from silanol groups.¹⁵

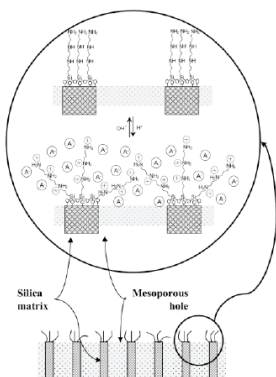


Figure 18. pH responsive molecular gate created by polyamines. The gate “open-close” mechanism is based on hydrogen-bonding interactions between amines (open-gate) and Coulombic repulsion between ammonium groups (closed-gate).⁷⁷

Another commonly used polymer for silica surface functionalization is polyethyleneglycol (PEG). It has been widely used for creation of sterically stabilized nanoparticles. Rapid nanoparticle clearance from the body is maintained by the body defense system (reticulo-endothelial system, RES) that recognizes an object as foreign. Anchoring of PEG on the nanoparticle surface has been reported to significantly decrease the RES uptake by reorienting it towards the aqueous solution, creating steric stabilization and preventing protein adsorption on the particle surface (*i.e.* opsonization).⁸¹ There are a wide number of functional PEGs commercially available. The “grafting to” method can be utilized to conjugate PEG polymers to the particle surface. Grafting-from synthesis of PEG, grown directly from silica surface via anionic ring opening polymerization of glycidol by using Si–OH groups as the initiators, has also been reported.⁷⁵

Versatile external stimuli responsive polymer surfaces acting as valves to open and close the mesopores in a reversible manner have been reported. An example of a widely used thermoresponsive polymer is poly(N-isopropylacrylamide) (PNIPAM). Furthermore, the polymer technology allows the use of co-blockpolymer type of moieties consisting of, for example, an external stimuli reactive block and a stealth polymer outer block. Here, the aim of the external stimuli block is to close the pores, while the aim of the stealth block on the outer particle surface could provide the colloidal stability.⁷⁸

2.8. Standard bioconjugation strategies

To target nanoparticles in an effective manner, bioactive ligands can be conjugated to the outer surface of the particles. Bioconjugation can be employed to modify surfaces initially derived from co-condensation, grafting or surface polymerization to be further coupled with spacer arms or cross-linkers to create reactive groups for coupling small molecular ligands or biomolecules.

In this chapter the most common conjugation techniques are introduced. For complete report of all available techniques *Bioconjugation techniques* and *Recent Advances of Bioconjugation Chemistry in Molecular Imaging* are referred.^{15,82} Here, the most common conjugation techniques are separated into three broad categories, which are zero-length cross-linking, cross-linker mediated linking, and conjugation through streptavidin–biotin interaction.

For a nanoparticle functional group–biomolecule functional group pair there are usually several coupling methods available, with the choice of method based on the effectiveness, particle stability, and bioactivity loss associated.

2.8.1. Zero-length cross-linkers

Zero-length cross-linkers form chemical bonds between functional groups of the molecule to be conjugated and the particle surface functional groups,

without the use of a mediating linker.

A popular method for covalent linking of biological functions by using zero-length cross-linkers is the use of 1-ethyl-3-(3-dimethylaminopropyl) carbodiimide hydrochloride (EDC)-mediated carboxyl-amine coupling to form an amide “peptide” bond. Bioconjugation by amide bonds is very common since biomacromolecules such as antibodies usually possess several primary amino and carboxylic acid groups. EDC is a water-soluble derivative of N,N'-dicyclohexylcarbodiimide (DCC). These compounds convert carboxylate into an O-acylisourea intermediate. However, this intermediate is unstable in water leading to deactivation of the molecule via hydrolysis. Due to this N-hydroxysuccinimide (NHS), or its more water-soluble derivative N-hydroxysulfosuccinimide (sulfo-NHS), is used in combination with EDC, in order to obtain more stable NHS-ester intermediates to retain coupling capacity in water (Figure 19). Many compounds are commercially available in their preactivated NHS-ester-form, and the compounds can be stored in a solid state or an anhydrous solution.^{15,83}

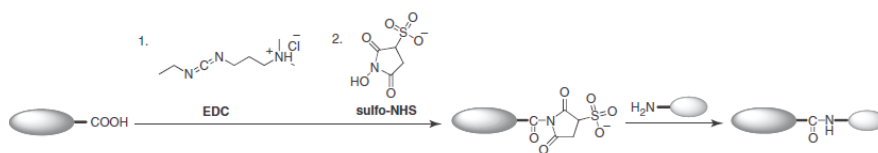


Figure 19. The carboxyl group activation reaction induced by EDC and sulfo-NHS to form stable amide bonds.⁸⁴

2.8.2. Cross-linkers

The chemical composition of nanoparticles and the molecules that are to be linked to the nanoparticle surface are not necessarily sufficient for a direct conjugation. In these cases, a cross-linker that is composed of a spacer with two terminal chemical groups that bind complementary groups on the nanoparticle and the biomolecule can be used. One example of a homobifunctional cross-linker is O,O'-Bis[2-(N-Succinimidyl-succinylamino)ethyl]polyethylene glycol consisting of an active NHS group at each end, capable of linking two amine groups together (Figure 20). Generally, a cross-linker containing two similar functional groups is called homobifunctional and a cross-linker with two different functional groups is of a heterobifunctional character.

In the reaction scheme shown in Figure 21, amine groups are coupled with thiol groups by applying a cross-linker with NHS ester and maleimide groups on opposing ends. In this example sulfo-succinimidyl-(4-N-maleimidomethyl) cyclohexane-1-carboxylate (sulfo-SMCC) is employed.^{86,87}

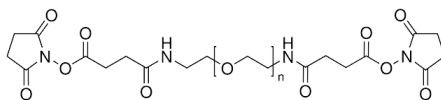


Figure 20. The chemical structure of a homobifunctional PEG O,O'-Bis[2-(N-Succinimidyl-succinylamino)ethyl]polyethylene glycol with activated carboxyl groups "NHS esters" at both ends capable of forming bonds with primary amino groups.⁸⁵

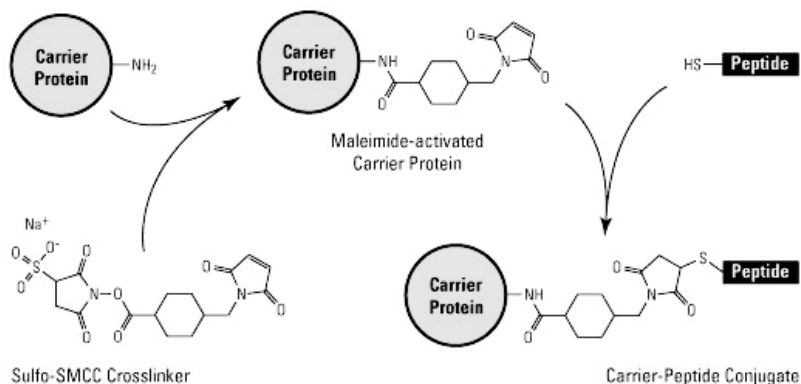


Figure 21. The sulfo-SMCC cross-linker is capable of forming maleimide-activated moieties which can further form covalent bonds with sulfhydryl (-SH) functional groups.¹⁴

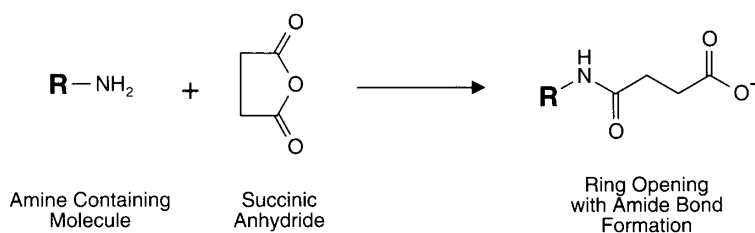


Figure 22. Carboxylation of amino surfaces by a ring-opening reaction of succinic anhydride.¹⁵

Another widely used cross-linker is succinic anhydride operating through a ring opening reaction with primary amine groups and thus converting them to carboxylate groups. Carboxylate groups can further be linked through activation with an amine group for example (Figure 22).

For targeted delivery, *i.e.* the specific interaction of the particle system with a target site, the targeting moieties (small molecules, or biomolecules such as proteins or peptides, antibodies or oligonucleotide or viral proteins) must be accessible on the outer particle surface in order to enable cell-specific recognition. It is worth noting that a short linker gives less spatial freedom for the targeting molecule to bind with its target molecule compared to a longer spacer.

2.8.3. Streptavidin–biotin interaction

Highly specific particle–biomolecule conjugates can also be formed through protein–ligand interactions. The most popular protein–ligand linking chemistry is the non-covalent interaction between streptavidin and biotin. Streptavidin consists of four identical streptavidin monomers, and therefore the molecule has four biotin binding sites. Streptavidin–biotin complex has an association constant in magnitude of 10^{15} , the highest known in biochemistry. The high association constant originates from a high shape complementarity between the binding pocket and biotin and from an extensive hydrogen bond network between the molecules. Streptavidin–biotin complex (Figure 23) is stable within a wide range of pH conditions and up to high temperatures. It is well known that ligand binding gives an increment in the thermal stability of a protein.^{88,89}

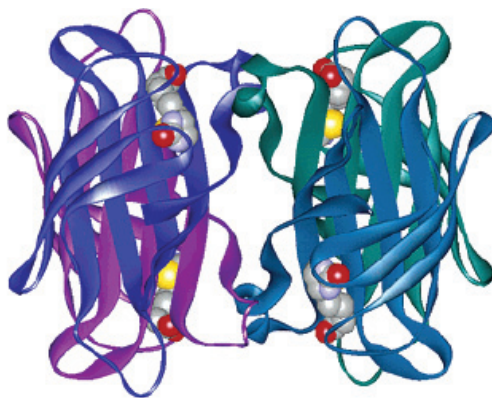


Figure 23. X-ray crystal structure of tetrameric streptavidin bound with four biotin molecules.⁹⁰

3. Nanoparticles for molecular imaging

Molecular imaging was first developed to localize antigens in light microscopy. Nanotechnology has now enabled molecular imaging to encompass all imaging modalities. To obtain good image quality, accumulation of contrast agents in the target site is a prerequisite and can be carried out by employing targetable imaging agent-containing nanoparticles to the site of action. Silica nanoparticles have been synthesized with wide range of contrast agents to enable their use in diverse imaging techniques. They have been coupled with fluorescent and entities for optical imaging,^{91–95} with radionucleotides for positron emission tomography (PET)^{96,97} and with various contrast agents for increase the contrast in magnetic resonance imaging (MRI).^{95,98} In this study, fluorescently-labeled silica nanoparticles were traced in the bioenvironment by optical imaging.

3.1. Fluorescently-labeled silica nanoparticles

Conventional molecular imaging employs labeled proteins such as monoclonal antibodies as imaging probes. However, the chemical modification of proteins is limited due to the potential loss of their biological functionality. The limit is approximately ten substitutions per molecule after which the antibody loses its antigen-recognition capability. Compared to this, the loading capacity of imaging agents in one single nanoparticle is remarkably higher, and beneficial especially for imaging modalities that are low in sensitivity. Conjugating them to nanoparticles provide a way for significant signal amplification. Particularly often the imaging and targeting is combined, as the contrast agents are incorporated into the carrier matrix while the particle surface remains free for subsequent conjugation of targeting moieties.^{99–101}

The well-studied functionalization techniques, co-condensation or grafting, can be used to synthesize fluorescently labeled silica nanoparticles. Fluorophores are trapped inside the inorganic material that protects them from the external environment, which reduces significantly the chemical or biological quenching. The high intensity and excellent optical stability of fluorescent nanoparticles enables ultrasensitive analytic determination, selective recognition, sensitive imaging and reporting and the monitoring of rare biological events that are otherwise undetectable using existing fluorescence-labeling techniques.¹⁰²

High numbers of fluorescent probes are available in their functionalized derivatives. Fluorescein (*Ex/Em* 494/518 nm) and its derivatives represent one of the most popular fluorescent-labeling agents. The fluorescent character of the fluorescein molecule originates from the presence of a fused three-ring aromatic structure. Most of its derivatives are prepared through substitutions to

carbons 5 and 6. Generally the functionalization of the fluorophore does not have any major impact on the fluorescent properties (Figure 24).¹⁵

Fluorescent probes can be covalently conjugated inside the silica network by replacing small amounts of alkoxysilane with an organosilane. For instance, aminosilane can react with several fluorescein derivatives such as fluorescein isothiocyanate (Figure 25) or fluorescein N-hydroxysuccinimide (NHS) (Figure 26). Grafting fluorophores to functional groups of the nanoparticle is the post-synthetic way of preparing fluorescent silica nanoparticles. Another benefit of nanoparticle technology is the option to multilabel the particle, for instance the particle structure-wise, and in this way to track several parameters simultaneously.

The type of label used and the labeling strategy must be considered carefully. Dyes have different quantum yields and therefore the amount of fluorophore needed varies depending on the label used. Some of the dyes are highly sensitive for pH changes.¹⁰³ Furthermore, multilabeling and the use of too high concentration of one and same fluorophore can lead to self-quenching. For *in vivo* imaging, near infrared (NIR)-emitting fluorophores are advantageous as their spectral window is between 650 and 1000 nm, which is the wavelengths that have minimum interference from tissue auto-fluorescence and can transmit tissues to be monitored outside the animal.¹⁰⁴

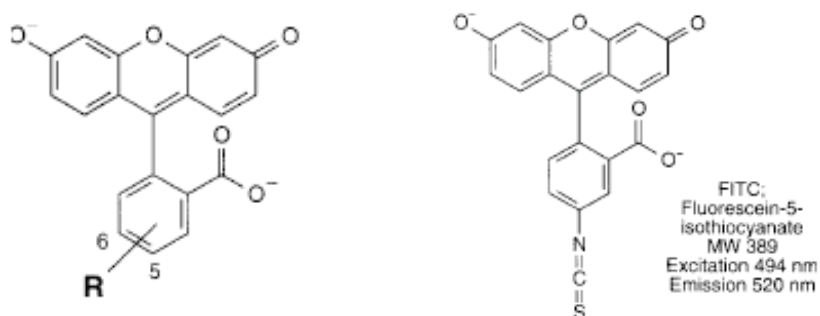


Figure 24. Molecular structure of fluorescein (on the left) and fluorescein isothiocyanate (on the right).¹⁵

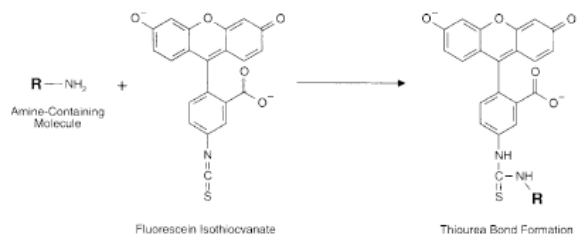


Figure 25. Fluorescein isothiocyanate can react with primary amines such as aminosilanes to form a stable covalent thiourea bond. By utilizing the co-condensation approach, the contrast agents can be taken to the silica material structure during the synthesis step.¹⁵

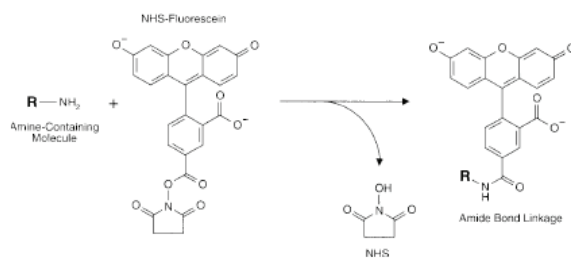


Figure 26. NHS-Fluorescein (5-carboxyfluorescein succinimidyl ester) reacts with primary amine groups to form an amide bond.¹⁵

4. Receptor-mediated uptake of nanoparticles

4.1. Active targeting

In order to actively target specific cells, the external surface of the silica particle can be modified with chemical entities acting as ligands for cell membrane receptors. Active targeting provides benefits over traditional treatments through increased efficacy as therapeutic agents are targeted specifically to the site of action while minimizing off-target side effects caused by the dosing of normal tissues. Targeting agents are classified in proteins (mainly antibodies and their fragments), nucleic acids (aptamers) or other small receptor ligands (peptides, vitamins, hormones, and carbohydrates).⁹¹ Passive targeting of nanocarriers is a mechanism of tumor biology during which particles accumulate in the tumor site through the enhanced permeability and retention (EPR) effect. Silica nanoparticles have been successfully targeted using peptides, proteins^{105,106} and small molecules as targeting ligands.^{107,108}

The targeting of nanoparticles occurs via cell-surface protein recognition and following particle binding to that receptor. Next, depending on the surface protein character, particles are either internalized to cells via specific endocytosis mechanisms or they remain attached to the cell surface receptor. Endocytosis is an active transport process dependent on time, pH, temperature and energy.¹⁰⁹ The four basic endocytosis mechanisms are caveolae- and clathrin-mediated endocytosis, macropinocytosis, and clathrin- and caveolae-independent endocytosis.^{110,111} It is challenging to draw general conclusions about how to produce particles for optimal cellular uptake, as the rate and the mechanism of uptake are cell-type dependent and vary between nanoparticles of different sizes, charges, and other surface properties.

Because particles with a positive charge address an attractive force towards a negatively-charged cell surface, one would anticipate that positively-charged particles would be endocytosed more efficiently than negatively charged particles. The work of Harush-Frenkel *et al.* indicated that this was true for HeLa cells. The positively-charged nanoparticles with a diameter of 80 nm had an uptake 2-fold higher than that of negatively charged particles of an equal size.⁸¹ Slowing *et al.* obtained similar results. They studied internalization of 150 nm mesoporous nanoparticles functionalized with 3-aminopropyl (AP), N-(2-aminoethyl)-3-aminopropyl (AEAP), N-folate-3-aminopropyl (FAP) and 3-[N-(2-guanidinoethyl) guanidino]propyl groups and particles with intrinsic silanol groups. Particle internalization in HeLa cells was purely dependent on the surface charge with highly charged particles uptaken at a faster rate.¹¹² In contrast to these results, a higher uptake for negatively-charged particles had been observed in HEK cells, reported by Zhang *et al.*¹¹³ Maneerat *et al.* studied the effect of size and surface charge. They prepared mesoporous particles with

sizes of 10 nm and 50 nm. Uptake studies were conducted in ovarian cell lines for particles with intrinsic silanol, amino, and carboxyl groups. The results indicated that intrinsic 10 nm particles and 50 nm carboxyl-modified particles had the highest uptake in each particle size class.¹¹⁴ These studies show that more research on the topic is needed to clearly understand all related factors. For instance, the polyvalent surface of nanoparticles may induce cross-linking of cellular receptors, start signaling processes and induce structural alterations on the cell surface, and interfere with normal cell functions.^{115,116}

Moreover, there may be cell-type-specific differences in the handling of already internalized particles such as in intracellular sorting, trafficking, and particle localization.¹¹⁵ The cellular uptake of nanoparticles is also shown to be concentration- and time-dependent. Longer incubation times and higher concentrations have been shown to enhance the uptake of particles conjugated with a targeting ligand and control particles.^{102,117}

To reach high cell selectivity, a surface marker should be overexpressed on target cells, where receptor density of 10^4 – 10^5 copies per cell is reported to be the limit for effective cell recognition. It is generally known that multivalent binding of an object with its target cell leads to a higher binding affinity, which increases the targeting efficacy. It is, therefore beneficial to aim for a higher ligand density on the nanocarrier surface. Dendrimer nanocarriers conjugated with 3–15 folate molecules were reported to have 2500–170 000 -fold higher dissociation constants (K_D) over free folate when comparing the binding efficiency to the folate-binding proteins immobilized on an artificial surface.¹¹⁸

4.1.1. Antibodies as targeting ligands

Antibodies or immunoglobulins (Ig) are a group of proteins that are found in the blood serum and tissue fluids of mammals. Their role in the adaptive immune system is crucial because they recognize and bind to foreign compounds (antigens) and trigger the elimination of those compounds by creating a specific reaction to each infectious compound and eradicates that from the body. The key features of the adaptive immune system are its specificity and memory. The system remembers infectious compounds and can prevent it causing disease later.¹¹⁹

There are five classes of Igs: IgG, IgA, IgM, IgD and IgE. The major Ig class is of the IgG-type, accounting 70–75% of the total Ig content of serum. The average molecular size of IgG is approximately 150 kDa. The molecule is composed of four peptide chains, two identical heavy chains with an average size of 50 kDa and two identical light chains of about 25 kDa, thus forming a tetrameric quaternary structure. The two heavy chains are linked to each other with a light chain of disulfide bonds (Figure 27).¹¹⁹

Targeting cancer with monoclonal antibodies (mAb's) was first demonstrated by Millsten in 1981.¹²⁰ It is possible to create a monoclonal antibody specific

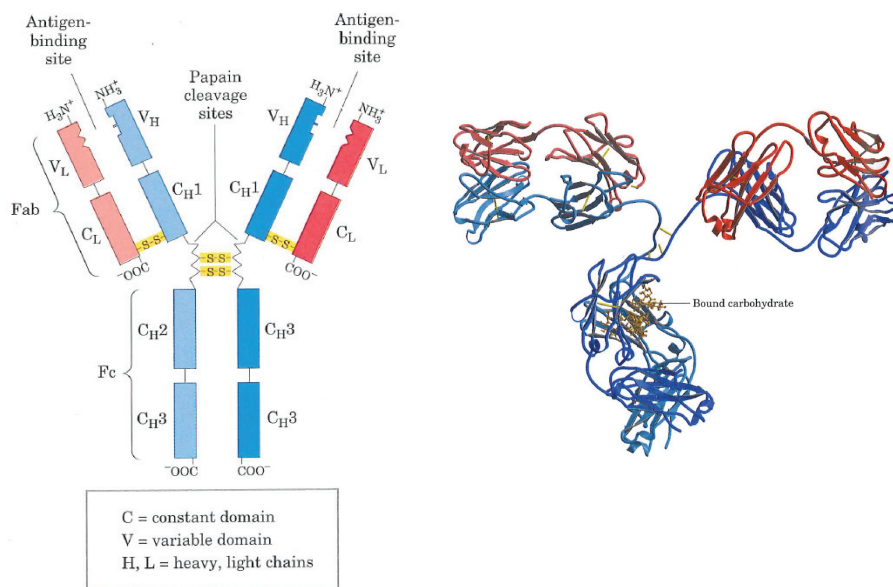


Figure 27. (On the left) A schematic illustration of an IgG type antibody. An IgG has two light and two heavy polypeptide chains. The Fab “antigen-binding region” consists of the light chains. The Fc region is the antibody stem, which is composed of the two heavy chains. The chains are bound together with covalent disulfide bonds and noncovalent interactions. The Fc part of the molecule is responsible of the immunogenicity. (On the right) an x-ray crystallographic structure of an IgG molecule.¹¹⁹

to almost any extracellular cell-surface target, which makes mAb's an attractive class of targeting ligands for nanocarriers. There are already thousands of identified markers on tumor cells, for which there is a “matching” monoclonal antibody pair available.¹²¹ MAB's have been used for targeting nanoparticles both *in vitro* and *in vivo*.

As the antibody molecules are relatively large, single-chain fragment variable recombinant antibodies (scFv) with an average size of 25kDa have been synthesized by genetic engineering.¹²² Antibody fragments have an improved biodistribution compared to that of intact IgGs due to their small size and absence of the highly immunogenic molecular stem. However, these molecules have proved to have a shorter retention time and express a decreased affinity and specificity compared to those of antibodies.¹¹⁷

Several studies have demonstrated the antibody-targeted silica *in vitro* and *in vivo*.^{126,127} Tsai *et al.* successfully targeted breast cancer cells by using Herneu mAb conjugated mesoporous silica particles.¹⁰⁵ The conjugation of biomolecules to an inorganic robust matrix such as nanoparticle surface generally

increases the stability of the biomolecule,¹²⁸ similar to a noncovalent interaction, such as a substrate ligand interaction that stabilizes the protein's three dimensional structure. Increased stability extends the lifetime of the biomolecule in various bioenvironments. As high numbers of ligands can be conjugated to one single particle, the multiple binding of ligands to their target cells is used to facilitate recognition and to increase binding efficacy.¹¹⁹ Mazzuccelli *et al.* reported a successful targeting of silica nanospheres to HER-2 overexpressing breast cancer cells by using anti-HER-2 scFv fragments as targeting ligands. These single-chain fragments exhibit a decreased retention time, decreased affinity as well as decreased specificity compared to those of intact HER-2 antibodies. By conjugating of multiple fragments to the silica nanoparticle surface, the binding efficacy was increased 4-fold, which is close to the affinity of intact anti-HER-2.¹¹⁷

5. Drug incorporation and release

The drug loading of mesoporous silica nanoparticles is typically a postsynthetic procedure. Drugs can be incorporated into the nanocarriers by surface adsorption or by covalent conjugation.^{129,130} MSN's possess high specific particle surface and large pore volumes, allowing incorporation of large quantities of drugs.¹³¹

The drug cargo can be incorporated inside the nanocarrier while guiding ligands are located on the surface to accomplish the task of targeted drug delivery. The targeting ligand can also function as a therapeutic drug.¹⁰⁷ Drug incorporation into nanocarriers allows the use of drugs with low hydrolytic solubility and stability, providing opportunity for reappraisal of drugs previously ignored because of their poor pharmacokinetics.¹³² The ceramic matrix of the silica carrier remains intact in organic solvents, which enables different types of solvents to be used in the drug loading steps. The solvent can be chosen in terms of drug's solubility in order to facilitate the drug adsorption to the pore walls over solvent-drug interactions. Because the drug incorporation process can be conducted in organic solvents, the repulsive forces between the carrier surface and the drug molecule that might be an issue in aqueous conditions due to electrostatic interactions (charges) and pH dependencies, in addition to possible drug hydrophobicity, can be discounted. On the other hand, when the drug is more hydrophilic, aqueous solutions and pH matching can be used to optimize the drug adsorption.¹⁶ In most cases, even after the functionalization process, the vast majority of the groups present on the silica surface are still silanol groups. Therefore the influence of the silanol groups on the overall chemistry of the pore surface should not be underestimated.¹³³ Drug adsorption to the carrier matrix leads typically to a monolayer formation and can be modeled using a Langmuir adsorption isotherm.¹³⁴ Monolayer adsorption onto the pore walls has also been observed for proteins from aqueous solutions.¹³⁵ To avoid premature drug release, the drug can be covalently linked to functional groups present on the pore wall.^{107,130,136} Depending on the physico-chemical properties of the drug, the drug loading inside the nanocarrier can provide the means for sustained release in order to maintain a drug concentration within a therapeutic window. One way to adjust the release profile is using molecular gates attached to the pore entrances or inside the pores themselves, which can be triggered by an external stimulus.¹³⁷ Other factors affecting the release profile are the particle pore size and particle matrix degradation. Moreover, the physical state that the incorporated drugs holds -amorphous, crystal or a combination- has an influence on the drug dissolution rate.

Biodegradable mesoporous silica nanoparticles have widely been reported as novel drug delivery systems holding promise especially in cancer therapy.¹³⁷⁻¹³⁹ The porous matrix may protect biomolecules from enzymatic deg-

radation. Silica nanoparticles have also been successfully used as carriers for targeted delivery of proteins, such as insulin, HIV-gp120, and Cytochrome C.^{117,140–142} Another very interesting therapeutic approach is the controlled delivery of vaccines. Antisense nucleotides usually have poor stability and cannot easily penetrate cells, and thus loading the compounds into a carrier matrix brings an extra benefit to the delivery approach. Nanoparticles conjugated with antigens have been found to generate a stronger immune response compared to conjugation with the free antigen alone.^{143,144}

6. Silica biodegradation

Nanoparticles aimed at theranostic applications have to remain intact, *i.e.* targeting and imaging groups, as well as the drug, have to remain associated with the particles until they have reached their site of action. Subsequently, degradation should take place to avoid carrier-induced toxicity. The rate of dissolution controls the detachment of the targeting ligands and the drug release profile, and therefore these parameters must be optimized for the application in question.

The solubility of amorphous silica in an aqueous medium is strongly dependent on the pH, temperature, on the degree of material condensation, specific surface area, and functionalization. Moreover, amorphous silica can occur in variable forms, which makes the mapping of the dissolution process challenging. Until now, a single pattern for the dissolution profile of amorphous silica has remained unclear.

In the dissolution process the silica network will depolymerize through hydration, hydrolysis, and ion-exchange processes.⁵¹ The chemical stability of silica significantly decreases in alkaline conditions, as the dissolution is promoted by water OH⁻ anions attacking silanol groups in the material.¹⁴⁵

Etienne *et al.* studied dissolution of native- and aminopropyl-grafted micron-sized mesoporous silica in water under biologically relevant pH conditions. The amino-functionalized silica dissolved at a faster rate than the native particles did and in 4 h, 2/3 of the amino-groups were found in the supernatant, after which the concentration of amino species in solution reached a plateau. It is important to note that particle properties such as surface charge can be dramatically influenced during the dissolution process. The fast dissolution was suggested to originate from the breakage of the chemical bonds between the aminopropylsilane and the silicon atom (Figure 28).¹⁴⁶

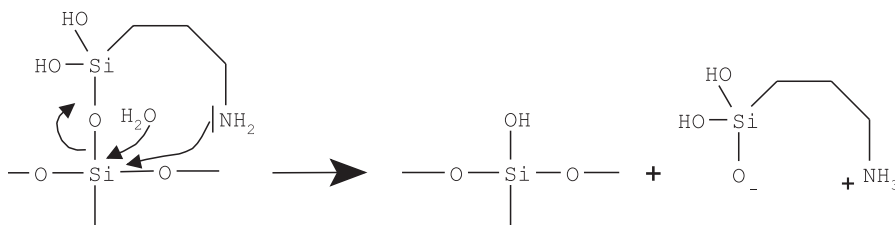


Figure 28. The breakage of the chemical bonds between the aminopropylsilane and the silicon atom leads to a faster dissolution process of aminofunctionalized mesoporous silica compared to that of native silica.¹⁴⁶

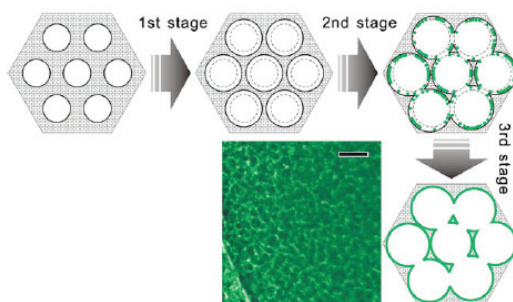


Figure 29. Schematic illustration of the degradation process of mesoporous nanoparticles in SBF. The highly-ordered hexagonal mesoporous structure degrades into a disordered network. The remaining walls are the result of the protective calcium/magnesium silicate layer deposited on the surface, which is illustrated by green dots in the 2nd stage and green lines in the 3rd stage.¹⁴⁹

The influence of the immersion time of mesoporous silica nanoparticles with sizes ranging from 200–800 nm in simulated body fluid, SBF, on the structure of the particles was studied by Onida *et al.* They reported a rapid decrease in the mesopore volume during the first hours after immersion; simultaneously signs of ordered mesoporous structure were still visible in x-ray diffraction (XRD) pattern. The authors proposed that the dissolved silica is re-deposited close to the mesopore openings gradually closing the pores. Further support for this claim was obtained from drug-release kinetic measurements, where the drug-release rate reached a plateau at times corresponding to the time at which the mesopore volume was strongly diminished. Similar to observations presented by Onida *et al.*, decreased drug-release rates connected to silica dissolution behavior has also been observed for micron-sized mesoporous silica.¹⁴⁸

He *et al.*, who obtained similar results to Onida *et al.*, illustrated a three-stage dissolution process for mesoporous silica in SBF. During the time below 1 h a relatively fast “initial burst” takes place. Then deposition of a calcium and magnesium silicate layer drastically decreases the degradation rate. The third stage of dissolution involves a slow diffusion of dissolved silica species detected as free Si. The whole sample was degraded after 15 days when immersed at a concentration of 0.5 mg/mL. Importantly, they reported an intact particle morphology up to 24 h even though hollowing out and enlargement of the mesopores was clearly observed (Figure 29).^{148,149}

There are very few studies related to *in vitro* cell degradation of silica nanoparticles. Degradation after particle uptake is of high importance as external factors such as the local pH in one biological environment compared to another varies remarkably, *e.g.* degradation in different cell compartments intracellularly takes place. Zhai *et al.* studied the degradation process by incubating

hollow mesoporous silica particles with a size of 300–430 nm in SBF *in vitro* with human umbilical vein endothelial cells (HUVEC). During the first day particle degradation took place in the cytoplasm and lysosomes, and after two days in the lysosomes only. Inductively-coupled plasma optical emission spectroscopy (ICP-OES) measurements indicated an increasing Si content in the culture medium over time. This suggests an ongoing degradation process inside the cells and also demonstrates that cells can excrete the degraded product into the culture medium.¹⁵⁰

Characterization techniques

The characterization of amorphous silica is challenging because the structure of the materials is enormously complex. Typically several techniques are used in combination to provide detailed and unambiguous structural information for the material.

The standard characterization of periodically-ordered mesoporous silicas include use of electron microscopies, small angle X-ray scattering (SAXS), small-angle x-ray diffraction (SAXD), gas adsorption analysis, and dynamic light scattering (DLS). Gas adsorption measurements are used to determine surface area, pore size, and pore size distributions. SAXS/SAXD can be used to determine the periodic-ordered structure of the material. The particle morphology is typically studied by scanning electron microscopy (SEM), while the ordered arrangement of pores can be detected by transmission electron microscopy (TEM). Important characterization technique used for the evaluation of fluorescently-labeled nanoparticles' specificity towards their target cells is fluorescence activated cell sorter (FACS) and a widely used technique to study their fate in biological environments is confocal fluorescence microscopy.

In the following section the characterization techniques used will be discussed at a level that is required for understanding the results that will be discussed.

7. Small angle x-ray diffraction

This technique is based on diffraction of x-rays by the electron clouds of the atoms in the sample. In the absence of absorption, the intensity of the scattered radiation is directly proportional to the electron density differences in the system. When an x-ray beam with a wavelength λ strikes a crystalline solid or a material with a periodic long-range order, the Bragg conditions are fulfilled and constructive interference occurs. Selective reflections of intensity for (hkl) planes will be observed in a diffractogram when the glancing angle satisfies Bragg's law (Eq. 5).

$$n\lambda = 2d_{hkl} \sin \theta \quad (\text{eq. 5})$$

Where n =integer number of wavelengths (order of diffraction), λ =wavelength, d_{hkl} = repeating distance between reflecting planes and θ =scattering angle.

Bragg's law relates the distance between crystal lattices d with the observed reflection angle. In the law the scattered intensity is measured as a function of scattering angle θ . Compounds with different unit cell parameters have different lattice spacing, and therefore different diffraction patterns will be observed for various materials. Thus the combination of d -spacing and intensities is characteristic for the structure in question. Furthermore, by analyzing the positions of the reflected beams, information about the size and symmetry of the lattice dimensions can be observed.

The periodicity of the material results in the diffraction phenomena. Therefore, XRD can also be used to analyze the material structure, *i.e.* the pore architecture of ordered mesoporous materials. Ordered amorphous mesoporous materials show reflections only in the low-angle range. Hexagonally ordered $p6m$ structured materials such as MCM-41 and SBA-15 result in an x-ray pattern containing three or more low-angle reflections. The $p6m$ structure is infinite in the c -direction, which results in the absence of periodicity along the c -direction and therefore only $(hk0)$ reflections are detected.

MCM-41 material reflections correspond to their hexagonal space group $p6m$, which can be indexed to a hexagonal $hk0$ lattice and are, therefore, indexed as (100), (110), (200), (210) and (300). A few characteristic x-ray patterns of some commonly observed mesoscopic structures are illustrated in Figure 30. The d -spacings of mesoscopically ordered 2D hexagonal and lamellar silica materials are illustrated in Figure 31. The (100) direction of 2D hexagonally-ordered materials is presented in Figure 32.

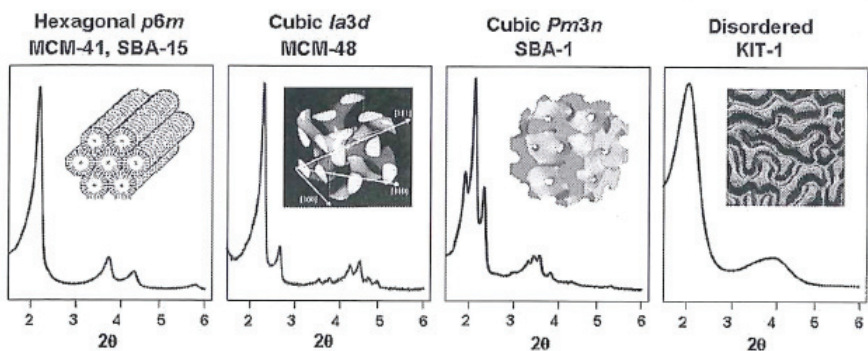


Figure 30. Presentation of typical x-ray diffraction patterns of some common mesoporous material structures.³⁶

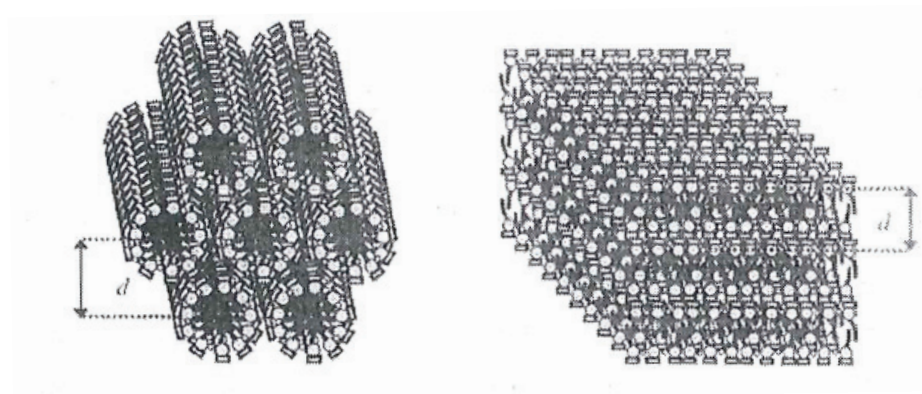


Figure 31. A schematic illustration of hexagonal and lamellar silicate-surfactant structures and their reflection planes, which yield their d-spacing.¹⁵¹

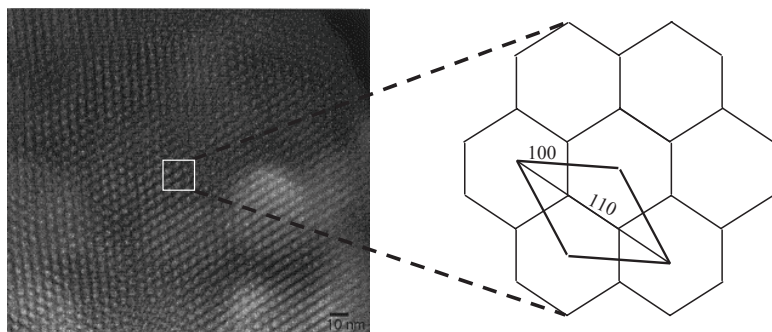


Figure 32. TEM image of MCM-41 type material (Left) together with a schematic illustration of the 2D hexagonally-ordered lattice (Right).³⁶

Mesostructured materials exhibit hexagonal, lamellar, or cubic meso-order. In a 2D hexagonal lattice the repeating distance d is related to the unit cell parameter a as

$$a = \frac{2d_{100}}{\sqrt{3}} \quad (\text{eq. 6})$$

where a is the lattice parameter which, in the case of hexagonally-ordered phases, means the distance between the centers of adjacent cylinders.

8. Nitrogen physisorption

Adsorption of gas molecules (adsorbate) can be used to determine the surface area, pore size distribution and pore volume of porous solids (adsorbent). Nitrogen physisorption process is described quantitatively by an adsorption/desorption isotherm, representing the amount of adsorbed/desorbed N_2 at a fixed temperature (77 K) as a function of pressure. Prior to the measurement, samples need to be outgassed to remove physisorbed molecules.

8.1. Porosity and classification of pores

According to IUPAC pores are classified according to their size.³

- Macropores: pores with widths exceeding 50 nm
- Mesopores: pores with widths between 2 nm and 50 nm
- Micropores: pores with widths between 0.7 nm and 2 nm
- Ultramicropores: pores with widths not exceeding 0.7 nm

8.2. The physisorption isotherms

The amount of gas adsorbed by a defined mass of solid depends on the equilibrium pressure, the temperature, and the nature of the gas-solid system. IUPAC has classified porous materials into 6 main types that have their characteristic adsorption-desorption isotherms (Figure 33). The shape of these isotherms is based on the strength of the adsorbent-adsorbate interactions and the type of porosity (or porosities) of the adsorbent. Type I shows steep uptake of nitrogen in low relative pressure, which is associated with the microporosity of the material. Type II and III isotherms are typical for nonporous or macroporous adsorbents, their difference being strong or weak adsorbent-adsorbate interactions respectively. The same way of interacting differs also type IV and V porous material from each other. Here the characteristic adsorption of nitrogen at higher relative pressures is related to capillary condensation inside the mesopores resulting in the hysteresis effect of the adsorption-desorption branch. The shape of the hysteresis loop reveals additional information about the pore structure. The type VI isotherm is relatively rare. It involves the step-by-step adsorption of layers on a highly uniform surface. As stated above, the shape of the isotherm gives direct information about the adsorbent-adsorbate interactions (weak or strong), monolayer-multilayer adsorption, filling and emptying of the pores, pore structure (size and shape), and layer-by-layer adsorption. Generally, the adsorption process in mesopores is dominated by multilayer adsorption and capillary condensation, whereas filling of micropores (pores of molecular dimensions) is controlled by stronger interactions.¹⁵² The samples prepared in this study are MCM-41 mesoporous materials expressing the type IV isotherms.

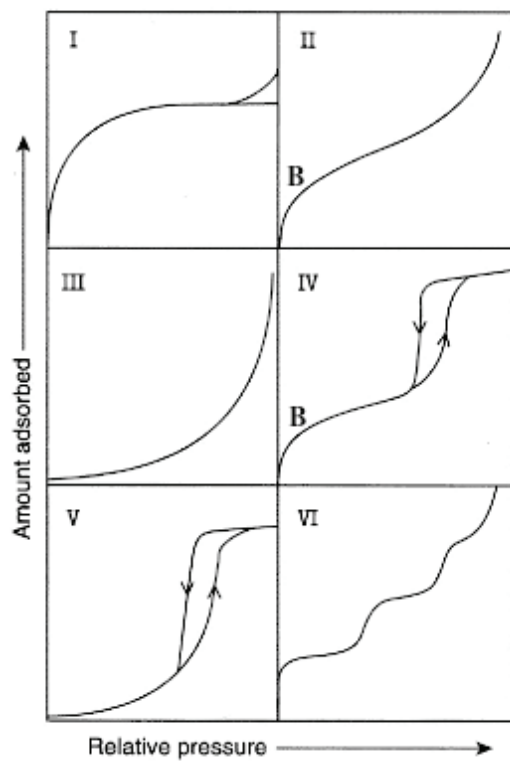


Figure 33. IUPAC classification of physisorption isotherms of porous solids.³

The specific surface area of the material can be determined by the Brunauer, Emmett, and Teller (BET) method using the physisorption isotherm data.¹⁵² To do this it is necessary to draw the BET plot and from that derive the value of the monolayer capacity, n_m .

$$\frac{P/P_0}{n(1 - P/P_0)} = \frac{1}{n_m C} + \frac{C - 1}{n_m C} \cdot \frac{P}{P_0} \quad (\text{eq. 7})$$

The constant C is related to the sharpness of point B shown in Figure 33 and the value is sensitive to both surface polarity and to the presence of microporosity. The C -value lies normally between 50 and 200.¹⁵² The BET surface area can be calculated as long as the BET plot is linear and does not cut the y -axis at $x=0$ at y -values below zero. The calculation requires that a_m , the average area occupied by each molecule in the monolayer, has a known value. For N_2 at 77 K the value of a_m is normally assumed to be 0.162 nm².

Furthermore, for v_p the total specific pore volume can be obtained from the adsorption isotherm as a liquid volume adsorbed at the end of the pore filling. However, it is not always possible to obtain this value since the adsorption capacity " P/P_0 approaches 1" depends on the magnitude of the external area and also the upper limit of pore distribution. In that case the isotherm does not reach its plateau at high relative pressures, the v_p is obtained at a predetermined P/P_0 close to 1.

The determination of pore diameter (pore width) of mesopores is based on the theory of capillary condensation and the application of the Kelvin equation. where γ is the surface tension and V_m is the molar volume of the liquid. The

$$\ln \frac{P}{P_0} = -\frac{2\gamma V_m}{r_k RT} \quad (\text{eq. 8})$$

equation shows the dependency between P/P_0 and the mean radius of the meniscus r_k . The radius of the cylindrical pore can be obtained by inserting the thickness of the adsorbed monolayer (t) to the value of r_k . There are different calculation models available for pore size distribution of which the Barrett-Joyner-Halenda (BJH) model is the most commonly used.¹⁵⁴ However, the BJH method based on the Kelvin-Cohan equation underestimates the pore size by ≈ 1 nm in the pore size range of 2–4 nm.¹⁵⁵ Although the BJH model is inaccurate in determining the absolute pore size, it is useful for comparing the pore sizes. A more accurate way of determining pore size distribution is the non-local density functional theory (NLDFT).^{154,155} DFT is used to create equilibrium profiles for all locations inside the pore, by minimizing the free energy. The free energy potential includes attractive and repulsive contributions of the fluid-fluid and fluid-wall interactions, which can be obtained using the NLDFT theory. Finally, the experimental isotherm is compared with the single pore

isotherms as determined by the theoretical isotherm calculations, which are based on the NLDFT method. The pore size distribution is obtained through fitting the experimental sorption isotherm to a linear combination of theoretical isotherms calculated for a given pore diameter. The weight coefficients of this fit are then used to determine the pore size distribution.

All nitrogen sorption measurements in this work were performed with an ASAP 2010 instrument (Micromeritics), at 77 K. Autosorb 1 software (Quantachrome instruments) was used to determine surface area by BET theory, and NLDFT theory was the basis for pore size and the pore size distribution calculations.

9. Electrokinetic zeta potential measurements

Zeta potential is an experimentally determined potential located in the proximity of the particle surface. When a charged particle is suspended in liquid, ions of the opposite charge will be attracted to the surface of the particle. The net charges at the particle affect the distribution of ions in the surrounding interfacial region in such a way that an increased concentration of counter-ions exists close to the surface of the particle (Figure 34). The liquid layer surrounding the particle will hence consist of two parts: an inner region, or the Stern layer consisting of strongly adsorbed counterions, and an outer layer, or the diffuse region, where both positive and negative ions less firmly form a charge “cloud”. The electrical double layer consists of these two layers.

The Stern layer is considered to be immobile so the particle and the adsorbed ions form a stable entity, meaning that when the particle moves in the liquid due to gravity or an applied electric field, for example, the ions within this boundary move along with the particle. The outer region of the diffuse double layer allows travel of ions via electrical forces and random thermal motion. This boundary inside the double layer is called the surface of hydrodynamic shear or the slipping plane. The potential between the particle surface and the dispersing liquid, varies in relation to distance from the solid surface. This potential, “close to the surface” at the slipping plane, is called the zeta potential. It is important to note that the zeta potential is an experimentally determined value and the precise quantitative meaning of “close” can not be defined.

Zeta potential is an important quantity in colloid chemistry since its magnitude gives an indication of the colloidal stability of the particle system. When the particles have a large negative or positive potential, the dispersion will resist flocculation and the colloidal system will be stable. The zeta potential varies strongly within the pH and therefore zeta potential should always be noted together with measured pH. Electrokinetic titrations can be utilized to determine the isoelectric point (IEP) of the system. The IEP is the pH point at which the net effective surface charge, *i.e.* the zeta potential, is zero. It is, therefore, the point where the colloidal system is least stable. Furthermore, the electrolyte concentration should also be taken into consideration, as added electrolyte will screen the surface charges reducing the thickness of the double layer and hence decreasing the absolute value of the zeta potential.^{44,156,157}

9.1. Determination of zeta potential by electrophoretic light scattering

Electrophoresis is capable of measure movement of colloidal particles in an electric field. Migration of particles can be determined optically by microelectrophoresis where location of individual particles can be determined in respect of time to marks on a grid of microscope eyepiece. Combination of microscopy with photon correlation spectroscopy enables determination of particles in the range of 3 nm and 5 μm .

In capillaries of microelectrophoretic cell, streaming potential takes place and the applied external voltage causes liquid in the cell to move, a phenomenon called electroosmosis. At a certain point x ($x=r/\sqrt{2}$) located between a cell wall and center of the cell is a stationary layer where particles move with their true velocity that origins solely from their own charge. An optical detection system, such as electrophoretic light scattering can be used to determine movement of the particles. The movement of the particles follows certain frequency that relates to their charge. Measured frequencies are converted to electrophoretic mobilities, velocities, and finally zeta potentials. The velocity (v_0) equals the product of electrophoretic mobility (μ_E) and the applied electrical field (E_0)

$$v_0 = \mu_E E_0 \quad (\text{eq. 9})$$

For calculating the zeta potential certain theoretical assumptions are necessary. In the following modified Stokes-equation the electrical field is the driving force for the movement of the particles.

$$\frac{v_0}{E_0} = \mu_E = \frac{Q}{6\pi a \eta} \quad (\text{eq. 10})$$

where Q is the charge of a particle, a is the radius of a particle, η is the viscosity.

The “thickness” of the double layer is determined by Debye-Hückel-parameter $1/\kappa$

$$\kappa = \sqrt{\frac{4\pi e^2 \sum n_i z_i^2}{\epsilon_0 \epsilon kT}} \quad (\text{eq. 11})$$

where e is the elementary charge, z_i is charge of the ion and ϵ is permittivity.

The dimensionless product κa represents the ratio of the particle radius to the thickness of the double layer

$$\mu_E = \frac{2\epsilon\zeta}{3\eta} f(\kappa a) \quad (\text{eq. 12})$$

where ζ is the zeta potential.

For low values of κa the Henry-function (eq. 12) approaches 1, for large values of κa the function approaches 1.5. These values correspond to the both borderline cases known as Hückel- and Smoluchowski equation. Smoluchowski approximation is generally used for the calculation of zeta potentials of dispersed colloidal systems containing spherical particles.¹⁷⁹

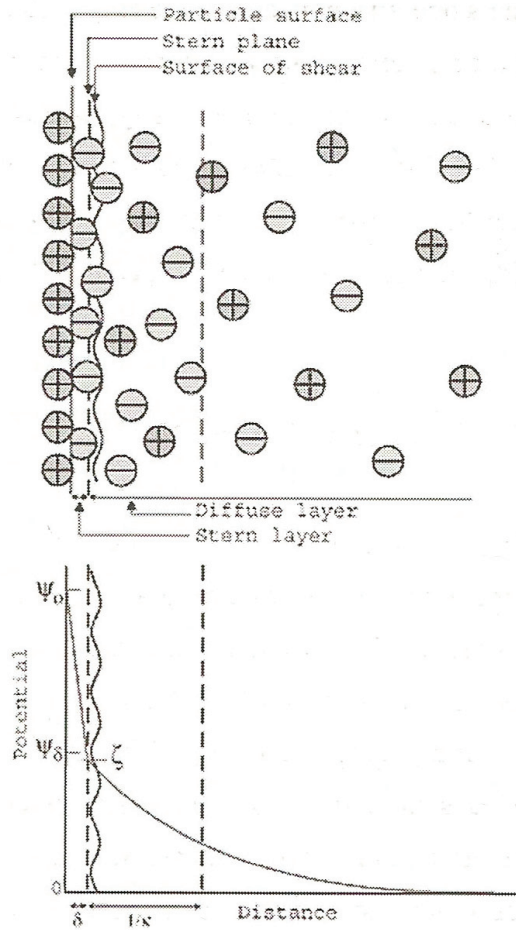


Figure 34. A schematic illustration of the structure of the electric double layer according to the Stern theory.¹⁵⁷

10. Dynamic light scattering

Dynamic light scattering (DLS) is applied to determine the hydrodynamic size of a nanoparticle. Brownian motion moves particles at a certain speed, which is related to the size of the particles, defined by the Stokes-Einstein equation.

$$D_H = \frac{kT}{3\pi\eta D_t} \quad (\text{eq. 13})$$

where k is the Boltzmann constant, η is the solvent viscosity, T is the absolute temperature, D_t is the diffusion coefficient and D_H is the hydrodynamic diameter of the particle.

When a sample is illuminated by a light source, such as laser, it scatters light in all directions. In this study DLS measurements were performed at 298 K, using a monochromatic laser, with a working wavelength of 632.8 nm and a non-invasive backscatter (NIBS), with the detector that is positioned at 173° relative to the laser beam. The speckle pattern is measured in relation to time, first within a certain time point t , next showing the fluctuation in scattering intensity at the time point $(t+\delta)$ continuing this way, always correlating the measured data to the previous one. According to the Stokes-Einstein equation, Brownian motion of the particles is slower for bigger particles than for smaller particles, which leads to slower fluctuation of intensity-speckle change for bigger particles. For the correlation, bigger particles fit for a longer time for the data collected from the previous data point, see Figure 35a. After the determination of the correlation function, it is possible to calculate the particle-size distribution, see Figure 35b. In the case of a sample consisting of particles in two size classes equal in number, the bigger particles scatter more light resulting in larger peak area by intensity. This results from the Rayleigh approximation, which describes the intensity of scattering to be proportional to the sixth power of the particle diameter. The size distribution of particles can also be determined by volume and by number (Figure 36). However, this data is generated from the raw data of the intensity.^{44,156,157}

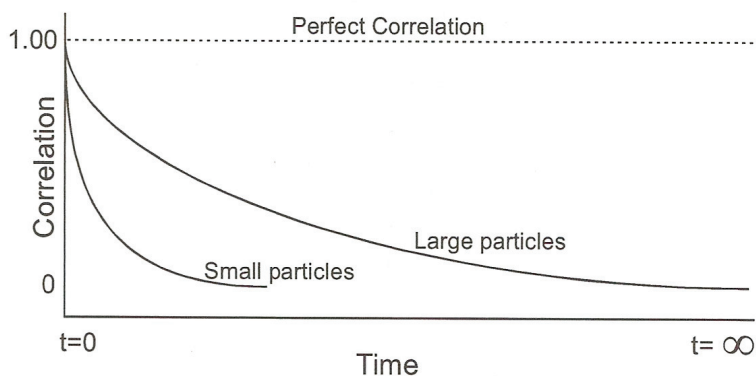


Figure 35a. Illustrated is a dynamic light-scattering correlation function for small and large particles. The rate of decay for the correlation is related to the particle size.⁴⁴

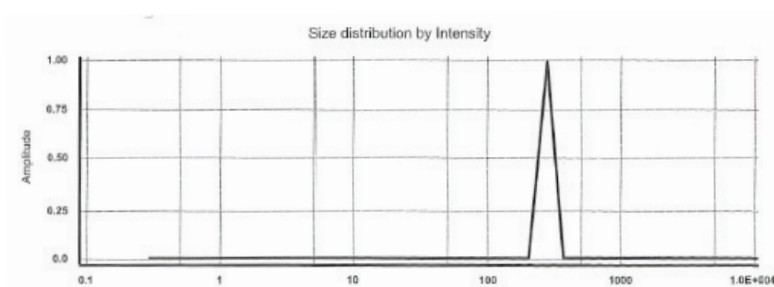


Figure 35b. Illustrated is a dynamic light-scattering correlation function for small and large particles. The rate of decay for the correlation is related to the particle size.⁴⁴

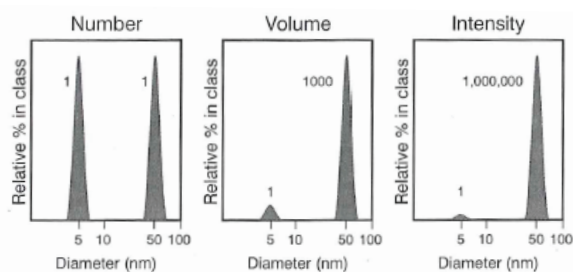


Figure 36. A sample containing particles of two sizes, 5 nm and 50 nm, equal in number. Particle distribution is represented by number, by volume, and by intensity.⁴⁴

11. Electron microscopy

The electron microscope operates on the same basic principles as the light microscope but uses electrons instead of light. Electrons have a much lower wavelength compared to photons, which makes it possible to get a resolution a thousand times better than with a light microscope.

11.1. Transmission electron microscopy

Depending on the set-up, transmission electron microscopy (TEM) enables the study of objects to an ångström level, such as imaging small details in the cell or different materials down to near atomic levels, making it a valuable tool for medical, biological and materials research.

An electron beam is generated by an electron gun commonly fitted with a tungsten filament cathode as the electron source and accelerated by an anode. Electromagnetic lenses focus the electrons into a very thin beam focused on an ultra-thin specimen.

Depending on the density of the material, some of the electrons are scattered and disappear from the beam. Electrons that transmit a specimen to a detector, provides a “shadow image” of the specimen with its different parts displayed in varied darkness according to the atom density in the sample. Electrons leaving the sample may have changed their direction, lost energy (inelastic scattering) or lost no energy (elastic scattering), or done both, even multiple times. Heavy atoms having high electron density result in more interactions between the electrons in the primary beam and those in the sample, which in turn provides a higher contrast in the resultant image. Biologic samples are often stained with heavy metals to increase their contrast in imaging.^{123, 158–160}

11.2. Scanning electron microscopy

In scanning electron microscopy (SEM), scanning of the specimen surface with a focused beam of electrons forms an image of the specimen’s topography. Similarly to TEM, a high voltage electron beam is created by an electron gun and focused to the sample by electrostatic and electromagnetic lenses. Primary electrons of the electron beam can enter the sample and refract around one or several atomic nuclei, exciting the sample by nearly unchanged energy called backscattered electrons. Since the heavier nuclei refract more electrons, the method can be used to determine the atomic composition of a sample. When electrons from the beam hit the nuclei of an atom in the specimen, secondary electrons are formed and emitted from the sample. Due to the remarkably lower energy of secondary electrons compared to that of primary electrons only electrons excited close to the surface of the sample manage to leave it. When the

beam scans a small area of the specimen surface, scattered secondary electrons are collected and an image of the specimen topography is formed.¹⁵⁸⁻¹⁶⁰

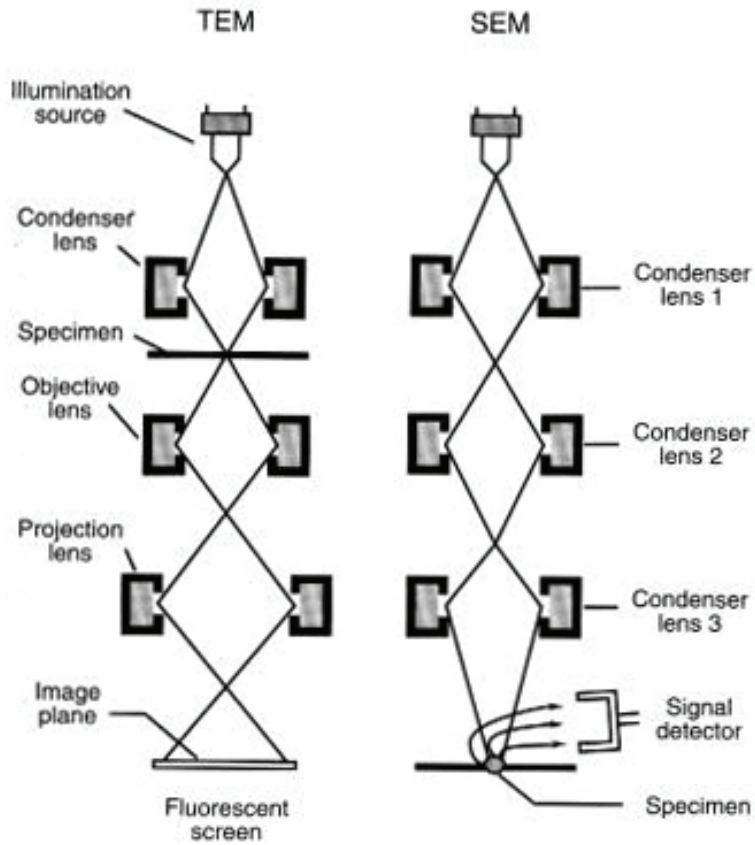


Figure 37. A principal picture of TEM and SEM devices.¹⁶¹

12. Confocal microscopy

The confocal laser-scanning microscope (CLSM or LSCM) is an instrument that is capable of constructing high-resolution images of 3D reconstructions of fluorescent samples. Fluorescent molecules absorb light of a certain wavelength and emit it at longer wavelengths. In the confocal microscope the light goes through excitation and emission filters wherein the wavelengths used depends of the fluorescent molecule used.

The key feature of confocal microscopy is its ability to produce blur-free images of thick specimens at various depths. In this technique images are taken point-by-point and reconstructed by using a computer. The microscope selectively collects images from a certain focal plane by using a directed beam of light from the laser.

The confocal microscope is based on a laser beam that passes a light source aperture and is further focused by an objective lens into a small (ideally diffraction-limited) focal volume within a fluorescent specimen. A mixture of emitted fluorescent light and reflected laser light from the illuminated spot is recollected by the objective lens. A beam splitter separates the light mixture by allowing only selected fluorescent wavelengths to pass while blocking the original excitation wavelength. The fluorescent light is then reflected into the detector (Figure 38). When the fluorescent light has passed a pinhole it is detected by a photo-detection device (photomultiplier tube (PMT) or an avalanche photodiode) which functions by transforming the light signal into an electrical signal, which is finally recorded by a computer.

Confocal microscopy imaging of a biological system should be carried out in such a way that the system retains its normal function. To reduce the damage caused by light, studies with fluorescence benefit from collecting efficiently the emitted fluorescent light available. This is particularly important for studies of living cells because photodynamic damage and consequent alteration in normal cell behavior is a concrete possibility.

It is common to incorporate multiple fluorescent probes within single cells or tissues in order to define the differential distribution of more than one labeled structure or molecular species. These types of multi-color or multi-spectral imaging experiments require adequate separation of the fluorescent emissions, and this is especially problematic when the spectra are substantially overlapping. Various spectral imaging computational processes are utilized to separate the emitted light into its spectral components.

Confocal imaging in living cells is dependent on the properties and availability of suitable fluorescent probes, for which the most important properties are high binding specificity, strong signal, slow bleaching, and nontoxicity leading to a high signal-to-noise ratio. To solve these specific problems, the use of nanoparticles as imaging agents has the potential to provide remark-

ably higher photostability and signal, compared to that of single fluorophores can produce thus enabling higher quantitativity in the analysis of the obtained data.^{147, 153, 162-163}

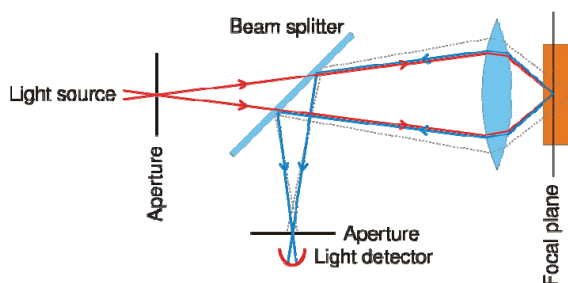


Figure 38. A schematic presentation of the principle of a confocal microscope.¹⁶⁴

13. Flow cytometry

Flow cytometry is a technique that is capable of simultaneously measure and then analyze multiple physical characteristics of single particles ($d \approx 0.2\text{--}150\text{ }\mu\text{m}$), usually cells, as they flow in a fluid stream through a beam of (laser) light. The properties that can be measured include relative size of particles, their relative granularity or internal complexity, and their relative fluorescence intensity. The technique determines these properties using an optical-to-electronic coupling system that records how the cell or particle scatters incident laser light and emits fluorescence.

In flow cytometry the fluidics system transports particles in a stream to the laser beam. The optics system consists of lasers to illuminate the particles in the sample stream and optical filters to direct the resulting light to detectors. The light that is scattered from the sample can be detected from various angles from the direction of a laser beam. Forward scattering (FCS) $<10^\circ$ from the direction of a laser beam tends to be more sensitive to the particle size and surface properties and is generally used to distinguish live and dead cells from each other. Side scattering (SSC) is detected from a 90° angle from the direction of a laser beam. SSC is used to detect the granularity of the cells. The electronics system converts the detected light into electronic data that can be processed by the computer. When the instrument is equipped with a sorting feature, the electronics system is also capable of initiating sorting decisions to charge and deflect particles.^{175–177}

Summary of the results

14. Article I

The purpose of Paper I was to study the influence of surface modifications and further functionalizations on the dispersion stability of silica nanoparticles in physiological conditions.

14.1. Construction of the model particle

A model system of nonporous, monodisperse silica nanoparticles with an average size of 240 nm was synthesized and further modified by various surface functionalization routes. To create sufficient functional surface groups on the intrinsic nanoparticle surface, first surface functionalization was carried out by hyperbranching polymerization of polyethyleneimine (PEI). Tethered polymer generally increases the number of anchoring groups for further conjugation. The relative amount of primary “accessible” amino groups in a PEI polymer was analyzed by using thermogravimetry and an imine method. Based on these analyses roughly 50 % of the surface-grown polymer amino groups turned out to have primary functions indicating that the polymer was fully branched to several generations.

The electrostatic stability of particle dispersions with varying pH values can be characterized by electrokinetic titrations. A high positive zeta potential of 60 mV of the PEI functionalized particles over a wide pH range, including also the neutral pH physiologically-relevant values, gave an indication of good dispersibility of the particles by electrostatic means.

To enable the attachment of specific biotinylated antibodies, the particles, surface modified by streptavidin, either native or fluorescently labeled, was accomplished. This covalent functionalization was carried out according to three different functionalization routes (Figure 39).

Streptavidin was attached to the PEI primary amino groups either directly (Route 3) or by using a glutaraldehyde (Route 1) or succinic acid (Route 2) as a linker molecule. To evaluate the dispersion stability, electrokinetic titrations were carried out for all streptavidin-conjugated particles in both water and saline solution (electrolyte concentration equals to that of phosphate buffered saline, PBS). IEP values provided from the titrations are summarized in Table 1.

The zeta potential changed according to the character of the conjugated surface functions. As aldehyde groups are not dissociable groups, this conjugation did not directly contribute to the surface-charge density and zeta potential, but its effect could be seen as the amount of effective amino groups decreased, leading to the increase of a relative concentration of negative silanol groups on the particle surface. In Route 2 succinic anhydride was used as a linker to form

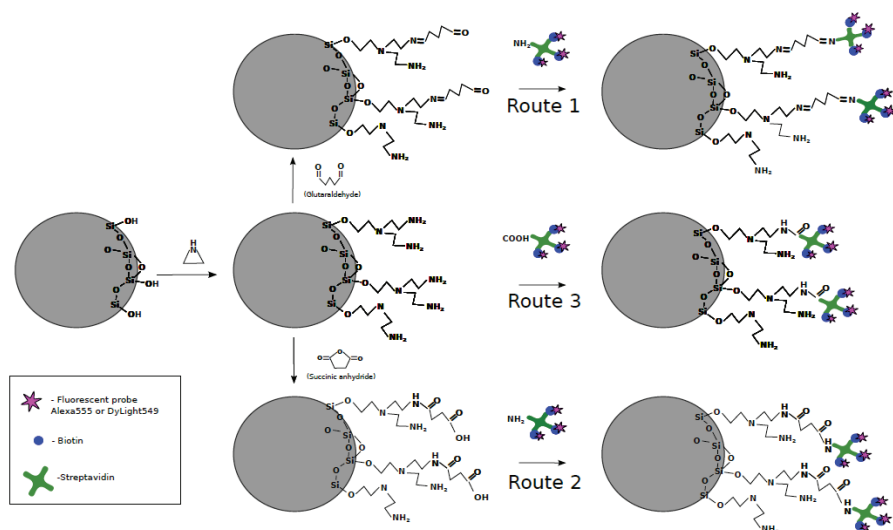


Figure 39. Streptavidin was conjugated on the particles by employing three different surface functionalization routes.

an amide bond between the linker molecule and particle, and then, further another amide bond between the linker and streptavidin. EDC (1-Ethyl-3-(3-(dimethylamino)propyl)-carbodiimide) “zero-length linker” was used in the procedure to activate the carboxylic acid groups in order to enable subsequent conjugation of streptavidin. The converting of amino groups into carboxylic acid groups via succinylation could be seen as a clear drop of the particle IEP from 10.3 to 5.35. The intrinsic pK_a for succinic acid is 4.16; therefore, the IEP of 5.35 indicates that not all of the amino groups were converted during the conjugation procedure. To compare the obtained values, an IEP of 3 has been reported for succinylated amino functionalized silica particles, where the amino groups were introduced by silanization.¹⁴ In this study, the PEI is hyper-branched polymer having also secondary and tertiary amino groups, which cannot be converted during the conjugation process but do contribute to the absolute surface charge of the particles. Moreover, streptavidin itself has an IEP of 5–7, which also explains the decrease of IEP. The IEP value presented in Table 1 shows that particles that are conjugated directly, without a linker molecule between streptavidin and the particle, provide higher stability for the particle suspension compared to using a linker molecule.

All surface functions influence the zeta potential of particles. For this reason, the influence of the type of fluorophore conjugated to the surface-bound streptavidin was studied in relation to dispersion stability.

The direct linking Route 3 was employed to conjugate fluorescent streptavidin, labeled either with Alexa555 or DyLight549. The particle stability was eval-

Table 1. The obtained IEP values of streptavidin conjugated particles determined from electrokinetic titrations in water or saline solution (SS). The saline solution has the same ionic strength as physiological media (0.154 M).

Stv-Alexa555, in water	6.1	5.9	9.3
Stv-Alexa555, in SS	7.1	6.2	8.2
Stv 30 μ g (unlabeled) in SS	8.5	6.2	10.2
Stv-DyLight549, in water	—	—	7.9
Stv-DyLight549, in SS	—	—	6.8

uated by conducting electrokinetic titrations, where zeta potential and particle size was measured in relation to the changing pH (Figure 40). While dispersions of particles conjugated with Alexa555-labeled streptavidin remain fully stable up to pH about 8, the conjugation with Dylight549 labeled streptavidin provides particles with an IEP of 7.9 leading to pronounced agglomeration within the biologically interesting pH range of 7–8. The Dylight fluorophores are synthesized through sulfonate addition, which makes these dyes negatively charged and hydrophilic. Dylight fluorophores are available as succinimidyl esters, the same as for Alexa555. Both Alexa555 and Dylight549 are amine-reactive dyes and are conjugated to free amino groups of the streptavidin tetramer, which means that the conjugation chemistry is similar.

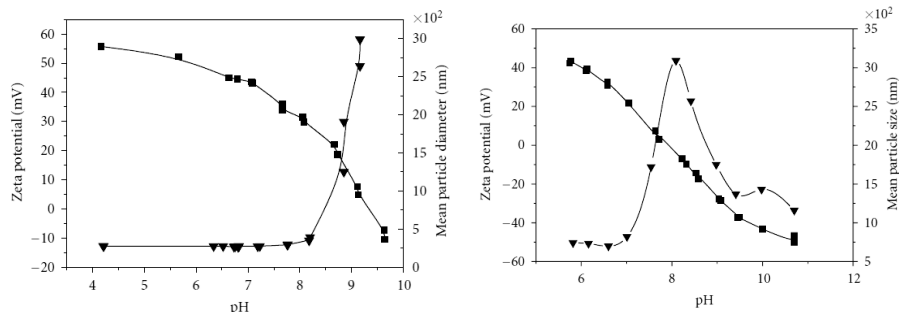


Figure 40. Simultaneous electrokinetic titration for the determination of the particle zeta potential (■) and dynamic light scattering for the measurement of the particle size(▼). (On the left) SiO₂-PEI-STV-Alexa555, IEP 9.3. (On the right) SiO₂-PEI-STV-DyLight549, IEP 7.9.

Confocal microscopy imaging was employed to evaluate the flocculation of the particles and the imaging characteristics of the differently conjugated particles (Figures 41–42). All of the particles prepared by different functionalization routes were fluorescing under the applied conditions, which indicated a successful conjugation of the labeled streptavidin to the particle surface. However,

only Alexa555-streptavidin conjugated by employing the direct route 3 showed virtually no flocculation, which also agrees with the measured zeta potential. Successful linkage of streptavidin on the particle surface was also confirmed by TEM imaging (Figure 43). Here streptavidin was conjugated by biotin- α 2 integrin antibodies labeled with protein A gold. Protein A gold could be observed on the particle surface, indicative of successful binding of the biotinylated antibody to streptavidin.

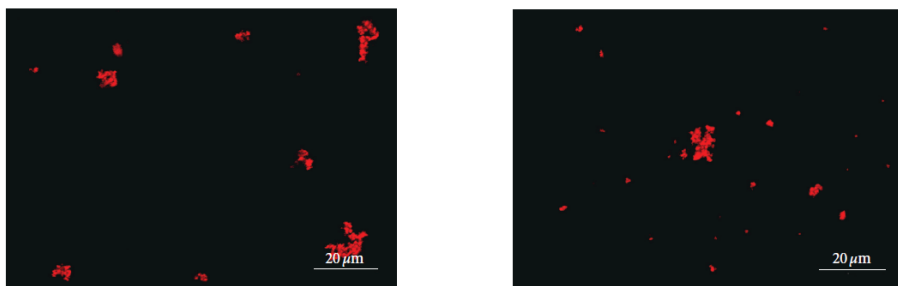


Figure 41. (On the left) PEI-GA-STV(Alexa555) particles (0.01 mg/mL) in water. (On the right) PEI-Succinic Acid-STV(Alexa555) in water (0.01 mg/mL). The scale bar corresponds to 20 μ m.

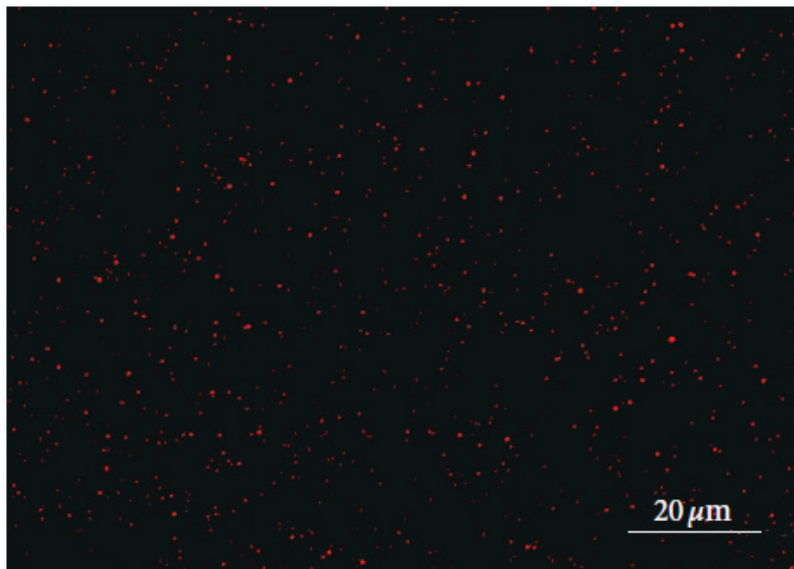


Figure 42. PEI-STV(Alexa555) (0.02mg/mL) in water. The scale bar corresponds to 20 μ m.

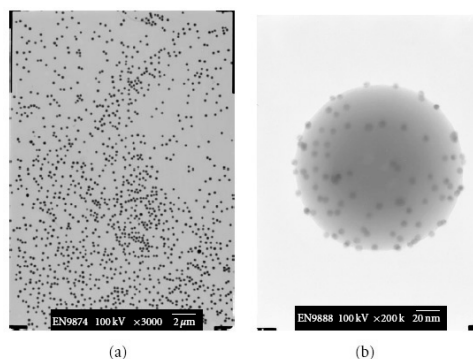


Figure 43. (On the left) PEI-GA-STV(Alexa555) particles (0.01 mg/mL) in water. (On the right) PEI-Succinic Acid-STV(Alexa555) in water (0.01 mg/mL). The scale bar corresponds to 20 μm .

14.2. Summary of the results

Fluorescent streptavidin complex was linked on the surfaces of the prepared nanoparticles by utilizing three different conjugation routes. The results clearly show that the stability of the particle suspensions is crucially dependent on all functional groups present on the particle surface. The surface functions may either directly affect the effective surface charge if the functions contain charged groups, or may indirectly affect them through relative concentration of charged groups on the nanoparticle surface. This introduced new methodology offers the means for fine-tuning the effective surface charge of the particles at a given pH, which is one of the key parameters for dispersion stability.

15. Article II

The purpose of Paper II was to study the intracellular decomposition of functionalized MSNs. The degradation and elimination of the particles from the body is important to minimize toxic effects of the carrier matrix itself. However, to fulfill their task, MSNs initially have to remain intact; the targeting and imaging groups, as well as the drug, have to stay associated with the MSNs until the particles reach their target site. A model system consisting of core-shell-shell silica nanoparticles, to which different fluorophores were selectively covalently linked was used to study the degradation processes of the particles *in vitro* (Figure 44). Confocal fluorescence microscopy was used as the main technique to analyse the particle fate in and outside the cells.

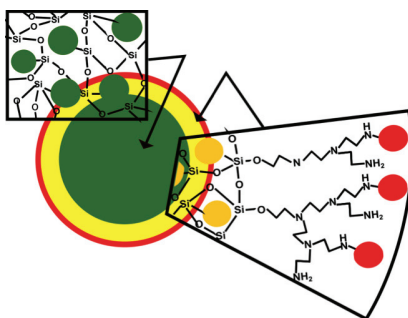


Figure 44. A schematic illustration of prepared three-color core-shell-shell particles.

15.1. Construction of the model particle

A three-layer particle structure was employed in order to enable tracking of the different parts of the particle in relation to the particle degradation as a function of time *in vitro*.

Fluorescent isothiocyanate isomer I (FITC) was incorporated by co-condensation into the solid core of the particle, and similarly tetramethylrhodamine isothiocyanate (TRITC) was co-condensed as part of the mesoporous shell. The surface of the particles was functionalized by surface-grown polyethyleneimine (PEI) and a third fluorophore, Alexa633 NHS ester, was conjugated to the primary amino groups of PEI.

In the discussion of the results, the different fluorescence emission colors will be indicated together with their locus in the particles as follows: green (C) for FITC-core, yellow (MP) for TRITC-mesoporous shell, and red (PEI) for Alexa633-PEI.

15.2. Characterization by the set of standard techniques

The prepared three-layer fluorescent silica particles were characterized by applying several techniques in combination. The size of the prepared particles and their uniformity was determined by SEM and TEM imaging together with DLS. The core-shell-shell MSNs have a diameter of about 240 nm and a very narrow size distribution, as shown in a SEM image. The core-shell structure of the MSNs is clearly visible, and the mesoporous shell is uniform as observed from the TEM image (Figure 45).

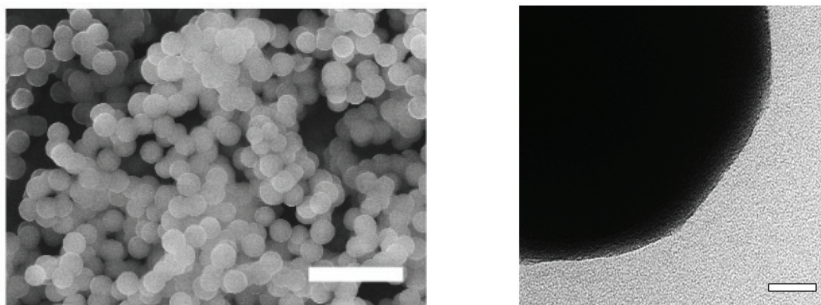


Figure 45. (On the left) SEM image of the core-shell-shell MSNs. The scale bar corresponds to 1 μm . (On the right) TEM image of the particles. The scale bar corresponds to 20 nm.

A nitrogen adsorption-desorption isotherm of the core-shell particles measured prior to surface functionalization is shown in Figure 46. A pronounced uptake of nitrogen at a relative pressure close to 0.3 P/P_0 is characteristic of mesophases synthesized using CTAB surfactant as a structure-directing agent and corresponds to filling mesopores having a diameter of about 4 nm with a narrow pore-size distribution. The specific surface area, obtained from the nitrogen physisorption data, was 344 m^2/g , and the specific pore volume of the primary mesopores was 0.34 cm^3/g . The pronounced uptake observed at the higher P/P_0 is due to the filling in interparticulate porosity. The low-angle SAXD pattern exhibits a main reflection at 2.2° 2θ and additional intensity in the regions expected for (11) and (20) reflections of a 2D hexagonal mesophase, suggesting an ordered mesoporous surface layer. Assuming a 2D hexagonal arrangement of pores, the lattice spacing derived from the (10) reflection is 4.83 nm (Figure 47).

The zeta-potential of co-condensed core-shell particles was -27 mV in 25 mM HEPES pH 7.2, which increased to +52 mV after PEI functionalization. This indicates a successful attachment of the highly cationic PEI layer. The

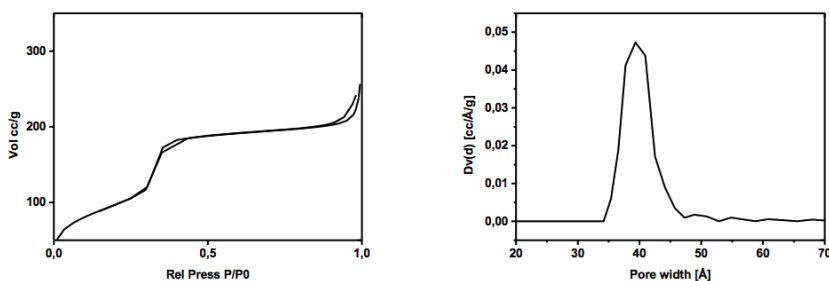


Figure 46. (On the left) N_2 physisorption isotherm for prepared core-shell particles. (On the right) N_2 physisorption BJH pore-size distribution in the mesoporous layer indicates a uniform pore size.

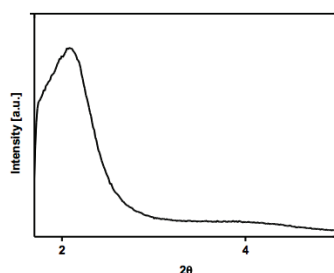


Figure 47. The SAXD pattern measured for the core-shell particles indicate an ordered porosity of the mesoporous shell.

content of PEI was analyzed by thermogravimetry. A mass loss of 7.1 wt-% in comparison to reference particles lacking PEI was shown. After attachment of the Alexa633 dye to PEI primary amino groups, the zeta-potential increased slightly to +55 mV.

15.3. Local pH correlates to the fluorescence intensity of the highly pH dependent fluorescein isothiocyanate

In contrast to the other two fluorophores in the particle, Alexa633 and TRITC, the fluorescence of FITC is known to be strongly pH dependent due to the pK_a of FITC being 6.4. Fluorescence intensity measurements using free FITC in buffers showed a decrease in the fluorescence intensity of about 50 % at pH 6.5 and of about 85 % at pH 5.5 as compared to the intensities measured for the same FITC concentration at pH 7.5, which is in agreement with the values in literature.¹⁰³

When similar experiments were performed for the core-shell particles void of PEI, a FITC fluorescence intensity decrease of 60 % was observed at pH 5.5 as compared to pH 7.5. Thus, the fluorescent intensity drop was lower than that of the free fluorophore. The smaller pH dependency of the FITC fluorescence emission intensity when incorporated into Stöber-type silica particles is tentatively attributed to different local pH values experienced by the probe inside the Stöber particles,¹⁶⁵ but these results also highlight that the Stöber-like particles are not completely nonporous, as external pH changes can indeed affect the dye.

Importantly, no pH-dependent changes in the fluorescence intensity of FITC were detected for PEI-coated core-shell particles, which suggest that the presence of PEI buffered the pH inside the core-shell particles. These obtained results will be discussed further as a means of clarifying the detachment kinetics of PEI from the MSNs, in addition to the analysis of the locus of the different fluorescent dyes.

15.4. Evaluation of the particle degradation *in vitro*

Confocal imaging, image analysis, and quantification was carried out to evaluate the particles' fate *in vitro*. Human SAOS-2 (sarcoma osteogenic) cells were incubated with the particles at a concentration of 125 µg/mL, and cell samples were taken at three points in time: 5 min, 1 h, and 4 h. Samples were fixed in paraformaldehyde for confocal imaging studies. 2D confocal images were acquired both near the surface of the microscope glass and from the upper half of the cell. All three fluorophore excitation wavelengths (488, 543, and 633 nm) were applied, and images were recorded separately (multitracking). Regions of interest (ROI) were drawn onto the recorded images so that particles outside the cells were analyzed separately from particles inside the cells. In total approximately 40 images from inside and 40 from outside the cells were analyzed for each defined point in time. The segmented objects were analyzed for the intensities of each of the three wavelengths as well as for average object size. Co-localization studies were performed to analyze the relationships of the different colors inside the cells. For that procedure all pixels in the images were analyzed, unlike for that in the segmentation-based analyses. Co-localization analyses were completed by recording all six possible Manders' co-localization coefficients and observing changes in these between the three time points: 5 min, 1 h, and 4 h. All image analysis was performed with the BioImageXD software.¹⁶⁶ The obtained results were statistically analyzed with a *t*-test for unequal variances and sample sizes, and significance was noted on graphs as follows: $ns = p > 0.05$, $* = p < 0.05$, $** = p < 0.01$, $*** = p < 0.001$.

15.4.1. Segmentations

All three fluorescent colors were segmented separately. The intensity of the yellow channel showed the highest stability over the measurement time. Therefore, intensities of all colors were measured based on the yellow channel segmentations; that is, pixels having yellow fluorescence were used as the basis of the total intensity of the green and red fluorescence, and the intensities were normalized against the total yellow fluorescence intensity. In these measurements no significant changes in the dye intensities outside the cells were detected over time. These segmentation results suggest that particles located extracellularly remained stable or dissolved in a homogeneous manner (Figure 48).

Particles were internalized already at the 5 min time point, and the number of internalized particles increased with time in accordance with the literature. The time-dependency of the fluorescence intensity measured for the three different fluorophores originating from particles located inside the cells followed a different pattern. While the total fluorescence emission intensity of the yellow (MP) remained constant over time, a clear decrease in the corresponding total intensities of the red (PEI) and the green (C) was observed with increasing incubation time. The decrease in the red (PEI) intensity, both in the individual segmentations and when normalized against the intensity of the yellow fluorescence, is consistent with a partial detachment of PEI from the particles with time, together with dilution of the surface-detached PEI, possibly due to endosomal escape.^{64,167} Moreover, the decrease also in the green (C) fluorescence intensities over time supports this suggestion. As noted in the discussion above, FITC fluorescence intensities decrease with decreasing pH in the absence of pH-buffering PEI polymer on the particles.

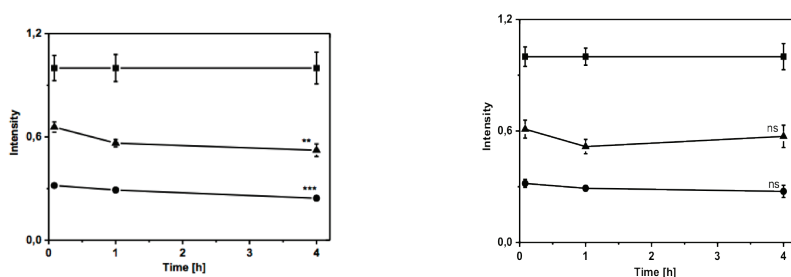


Figure 48. Intensity of the segmented objects over the observation time, measured both inside and outside the cells. (On the left) All of the colors are segmented in relation to the yellow channel inside the cells. (On the right) All colors are segmented in relation to yellow channel outside the cells. In the figures [ns] stands for non-significant change, and stars (*), up to three, describe the degree of significant change. (yellow ■, red ●, green ▲).

15.4.2. Co-localizations

Co-localization analyses of all three fluorophores were executed to obtain more detailed picture of the particle degradation process in and outside the cells. The results are expressed as Manders' coefficients, measuring two colors at a time. The number of pixels that contain both fluorescent colors is determined, and the total intensity of a given color within these pixels is divided by the total intensity of one or the other color within that segment. For example, the Manders' coefficients of red toward yellow and yellow toward red do not necessarily give the same result. This is due to the fact that red could be completely co-localized with yellow, which would correspond to a Manders' coefficient of 1, while yellow pixels might not coincide with pixels showing both red and yellow, resulting in a Manders' coefficient less than 1. It should also be noted that the determined Manders' coefficients are more sensitive to stable particles as compared to potentially detached fluorophores, the detached fluorophores being diluted and thus falling below the set threshold values. This implies that intracellular analyses are more sensitive to colors remaining inside cellular compartments rather than being located in the cytoplasm.

Separate co-localization analyses were carried out separately for particles located inside as compared to outside the cells. The changes in the Manders' coefficients in relation to the measured time for particles located outside the cells were within experimental error. The results suggest that the particles contained all fluorophores throughout the experiment. However, this does not mean that there was no particle dissolution but that the particles did at least not completely disintegrate nor did any of the layers completely detach from the main particle during the time observed. Similar to the segmentation analyses, inside the cells the co-localization was quite different.

The Manders' coefficients of all color combinations inside the cells are shown in Figure 49. The co-localization for green(C)-yellow(MP) is high over the time of observation, while the corresponding values for yellow(MP)-green(C) decrease significantly over time. This result suggests that the mesoporous silica layer is detaching from the main particles, and leaves some of the mesoporous layer behind. Also co-localization for red(PEI)-yellow(MP) is high throughout the experiment, while the Manders' coefficient for yellow(MP)-red(PEI) decreases in a significant manner over time. This result is consistent with a process where the mesoporous layer is dissolved in a way that some of the mesoporous silica layer is detaching together with the PEI layer from the particles, and at the same time a portion of the mesoporous silica layer remains associated with the main particle. This is also indicated by the high Manders' coefficient for green(C)-yellow(MP) throughout the experiments. Interestingly, the co-localization for red(PEI)-green(C) and green(C)-red(PEI) cannot be explained by using this simple dissolution model. The co-localization of green(C)-yellow(MP) remains throughout the experiment, as expected based on the values of the Manders' coefficients, while the co-localization is signifi-

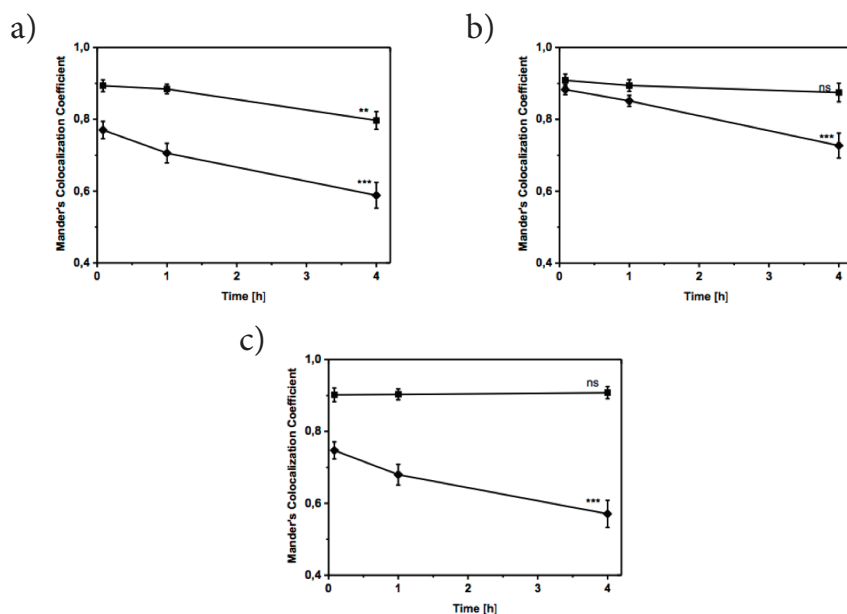


Figure 49. Calculated Manders' co-localization coefficients as a function of incubation time (a) for (red/green ■, green/red ◆), (b) for (green/yellow ■, yellow/green ◆), and (c) for (red/yellow ■, yellow/red ◆).

cantly decreasing for yellow(MP)-green(C) with time. This suggests that the core is separating from the PEI layer, while the PEI layer remains on the Stöber particle core. The finding can be explained by a coexistence of particles where some fraction of the core-shell-shell particles have lost their PEI layer, while some particles still have a PEI layer on them. In accordance to the discussion above, the detachment of PEI, which is also supported by the time-dependent total fluorescence intensity analysis, together with the escape of PEI into the cytoplasm, will lead to an overestimation of the amount of PEI present in intracellular compartments. PEI may be attached to particles or to fragments of mesoporous silica particles still present within intracellular compartments. As a conclusion, the results clearly suggest that the PEI layer is detaching from the particles, most probably both in the form of free PEI and PEI attached to fragments of mesoporous silica, and that this degradation process preferentially occurs inside the cells.

An illustration of the suggested intracellular degradation process of the core-shell-shell particles is given in Figure 50. These results do not allow for a more detailed analysis of the nature of the intracellular compartments such as different types of endosomes and lysosomes. However, the preferential intracellular detachment of PEI from the particles, do give clear support for the intuitive claims based on drug release studies that PEI must detach from the

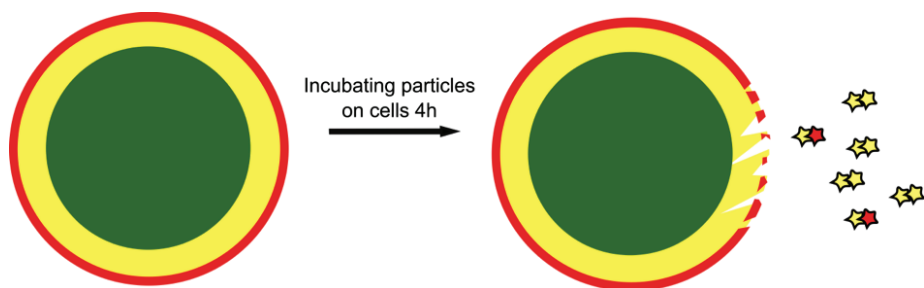


Figure 50. A schematic illustration of the suggested disintegration process of particles located inside the cells.

particles inside cells, providing a means for an intracellularly-triggered drug release. Furthermore, this mechanism seems to be operational irrespective of whether the drug is covalently linked to the PEI layer or if the drug is physically adsorbed into the mesopores of the MSNs, here referring to a previous study where MTX was delivered *in vitro* by using fully mesoporous nanoparticles.¹⁰⁷

15.5. Summary of the results

The obtained results clearly suggest that the PEI layer is detaching from the core-shell-shell particles, most probably both in the form of free PEI and PEI attached to fragments of mesoporous silica and that this degradation process preferentially occurs inside the cells. The results also suggest that the dissolution process is mainly driven by the dissolution of the mesoporous silica shell. These results further suggest that covalent attachment of drugs, targeting groups or other functionalities and their subsequent intracellular detachment is a promising route towards intrinsically-triggered intracellular release. Finally, these results demonstrate that new imaging-based methodologies can be used to effectively analyze the degradation of nanoparticles inside cells.

16. Article III

The purpose of Paper III was to demonstrate the targeting of nonporous monoclonal antibody-conjugated nanoparticles *in vitro*. The principle of the model system introduced in Paper I. Fluorescent nanoparticles are functionalized with biotinylated integrin $\alpha 2\beta 1$ monoclonal antibody-streptavidin complex for targeting $\alpha 2\beta 1$ stably expressing SAOS-2 cells.

Because the targets of many drugs are located in specific intracellular compartments, medically-used nanoparticles should not only bind to the cell surface and be internalized, but also find their way to the right location inside the cell. Due to these specific needs, the aim of the study was also to examine whether it is possible to guide nanoparticles into cells via a specific entry route that is characterized in a receptor-specific manner for the antibody used.

16.1. Construction of the model particle

Nonporous amino-FITC co-condensed silica nanoparticles with an average size of 70 nm (determined from SEM image) were synthesized by a Stöber process. The surface of the particles was functionalized by fluorescent streptavidin by using homobifunctional α, ω -Bis-NHS-PEG, Mw 3000 as a cross-linker between the particle-surface amino groups and the fluorescent-streptavidin amino groups. A PEG linker was utilized in order to provide steric stability and to minimize unspecific protein adsorption to the particles. The particle surface was finally modified with an $\alpha 2\beta 1$ integrin-specific antibody capable of recognition of $\alpha 2\beta 1$ integrin (Figure 51).

16.2. Characterization by the set of standard techniques

SEM and DLS were applied to analyze the morphology of the particles and their dispersibility, respectively. The successful surface modifications and imageability, were analyzed by electrokinetic measurements and confocal microscopy. Similarly to Paper II, confocal microscopy co-localization and segmentation studies were undertaken to analyze the cell-particle samples.

The hydrodynamic size of the particles was determined by intensity to ensure the uniformity of the particles after each conjugation step. After the attachment of PEG, the hydrodynamic size was about 130 nm with a polydispersity index (PDI) of 0.08. After attachment of PEG-streptavidin to the surface, the hydrodynamic size by intensity increased to about 170 nm, with a PDI of 0.124.

Surface functionalization can be followed with zeta potential measurements; the zeta potential for amino-FITC functionalized particles was 30 mV, which increased to 42 mV after the particle-surface modification with PEG and streptavidin. As the pI of streptavidin is, depending on the reference, in the

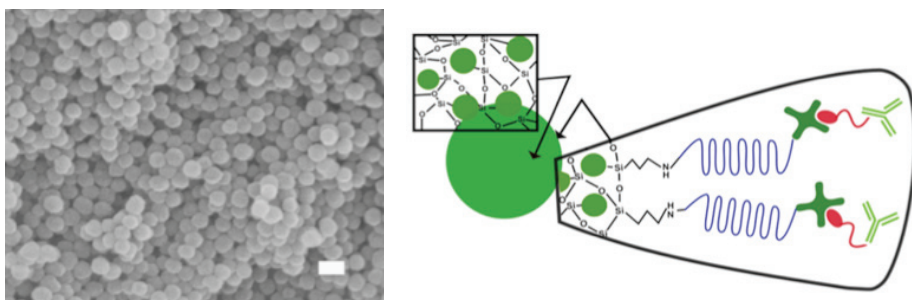


Figure 51. (On the left) A SEM image of the prepared Stöber-like nonporous nanoparticles. The scale bar corresponds to 100 nm. (On the right) A schematic representation of the particle structure. Particles were co-condensed with amino-organosilane and FITC while the surface was modified by a homobifunctional PEG cross-linker connecting the fluorescent streptavidin on the particle.

range of 5–7, the increase of the zeta potential after conjugation gives an indication of successful surface functionalization.

16.3. Targeting of the particles *in vitro*

16.3.1. Flow cytometry

In the final surface modification step, the streptavidin-functionalized particles were conjugated with biotinylated antibodies, either a monoclonal antibody against the integrin $\alpha 2$ -subunit “ $\alpha 2$ -particles” or a negative control antibody against NS-1 (not present on the SAOS-2 cells, “control particles”). The $\alpha 2$ -particles or control particles were incubated with the cells for 30 min, after which the attachment of the particles to the cell surfaces was determined using flow cytometry. The obtained flow cytometry results indicate that $\alpha 2$ -particles were specifically bound to the cell surface, whereas control particles showed only weak binding, similar to cell type-dependent background levels (Figure 52).

16.3.2. Confocal microscopy and image analysis

16.3.2.1. Co-localization of the $\alpha 2$ -conjugated particles with $\alpha 2\beta 1$ integrin

To further determine the co-localization of the $\alpha 2$ -conjugated particles with $\alpha 2\beta 1$ integrin, the cell surface was analyzed with 3D confocal imaging-based co-localization studies. Co-localization studies were conducted according to

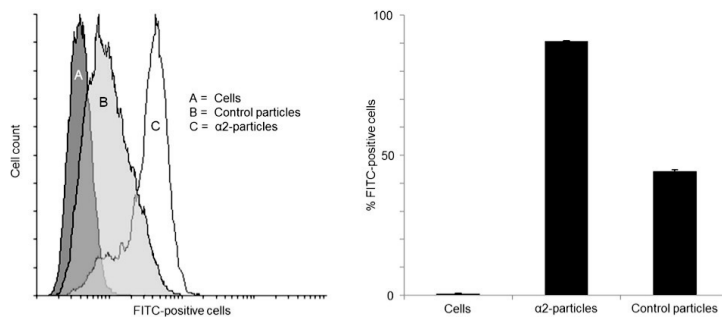


Figure 52. Flow cytometry. (On the left) The flow cytometry volume plot shows attachment of $\alpha 2$ -particles to the cell surface. The attachment of control particles is observed in a remarkably weaker manner. (On the right) The flow cytometry histogram of two repeated experiments represents the attaching of $\alpha 2$ -particles to the cell surface in a considerably increased manner compared to that of the control particles.

the principles presented in Paper II. Both particle types, $\alpha 2$ -particles and control particles, were analyzed for co-localization with $\alpha 2\beta 1$ integrin. To detect the FITC-labeled particle location in respect to the target receptor, $\alpha 2\beta 1$ integrin receptors were immunolabeled with Alexa555-coupled secondary antibodies.

The co-localization was analyzed in a quantitative manner, whereby it was quantified by segmenting the particle channel, followed by calculating the ratio of the integrin channel intensity within the segmented particles as compared to elsewhere in the cell. The applied particle concentration was doubled (250 $\mu\text{g}/\text{mL}$) to allow for more unspecific control particle-binding and proper comparison of the clustering effect between samples measured at the time points of 15 min and 60 min. To interpret the obtained data, a result of 1 would indicate the same amount of integrins at the particle sites as elsewhere in the cell and therefore no co-localization, whereas a number larger than 1 would indicate a higher amount of integrins at the particle sites than elsewhere. Both studied time points showed values close to 1 for the control particles, whereas $\alpha 2$ -particles showed significant co-localization with the $\alpha 2\beta 1$ integrins. Obtained results confirmed that the $\alpha 2$ antibody-containing nanoparticles could be specifically targeted to $\alpha 2\beta 1$ integrin-positive cells (Figure 53).

16.3.2.2. Clustering of integrin receptors

Characteristic of the $\alpha 2\beta 1$ integrin receptor-substrate interaction is receptor clustering followed by internalization of the clusters. Here, confocal studies were carried out to determine whether $\alpha 2$ antibody-conjugated particles could also induce such clustering. Again, the applied particle concentration was doubled (250 $\mu\text{g}/\text{mL}$) to allow for more unspecific control-particle binding and

proper comparison of the clustering effect between samples measured at time points of 15 min, where the clusters are typically very prominent.¹⁶⁸ The cells were stained with CellTracker Orange. Both particles and the cell membrane were segmented for the 15 min time point after which three central parameters for the clusters were quantified: intensity, volume, and number per cell surface area. During clustering the first two parameters should increase, whereas the last one should decrease.¹⁶⁶ Clusters of the particles conjugated with the $\alpha 2$ -specific antibody were much brighter and larger but fewer in number than those of the control particles. Thus, $\alpha 2$ -particles clustered significantly more on the cell membrane than control particles. This is probably due to the underlying integrin clustering. These results confirmed that the particles were attach-

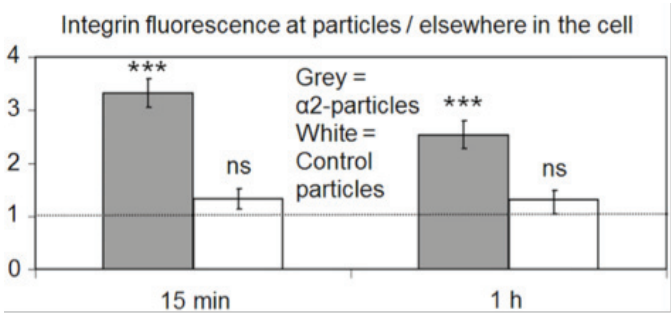


Figure 53. Co-localization was quantified by segmentation-based confocal imaging. As seen from the diagram, there was significantly more integrin signal at the $\alpha 2$ -particles than elsewhere in the cell. No such difference could be detected with the control particles. Twenty cells were analyzed for each sample. The p-values were following: < 0.05 (*), < 0.01 (**), and < 0.001 (***), "ns" is equal to "not significant". Error bars in the presented figures are standard errors.

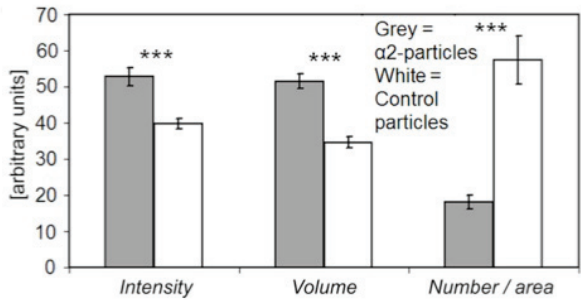


Figure 54. Quantification segmentation-based analysis of the particle clusters at the 15 min time point. Clusters were significantly larger, brighter, and fewer in number with $\alpha 2$ -particles than with control particles, all indicating stronger clustering with $\alpha 2$ -particles than with control particles. Twenty cells were analyzed for each sample.

ing to the integrins in a manner that could potentially trigger their internalization also.

16.3.2.3. Particle Internalization by $\alpha 2\beta 1$ integrin positive cells

While forming clusters, $\alpha 2\beta 1$ integrin is also internalized into the cell.^{166,169} 3D confocal microscopy studies were conducted to study whether the nanoparticles were similarly internalized. For these studies the original particle concentration of 125 $\mu\text{g/mL}$ was applied. To determine the internalization, both the particles and the cell membrane were segmented from the images, and the percentage of particle voxels inside the membrane was calculated.¹⁶⁶ Significantly more of the $\alpha 2$ -conjugated particles than control particles were internalized both at the 15 min and 1 h time points (Figure 55). Over the incubation time the percentage of internalized particles increased, as expected. However, the increase was larger for $\alpha 2$ -particles than for control particles. Using clustering studies the experiment was repeated with doubled particle concentration of 250 $\mu\text{g/mL}$. To enable more control particles to be analyzed and to see whether specific internalization could still be observed at higher particle concentrations also. As expected with the higher particle concentrations there was an increased unspecific entry of the control particles and at the 15 min time point there was no longer a difference between the two types of particles. At the 1 h time point, however, significantly more internalization was observed with $\alpha 2$ -conjugated particles and an increase in their internalization over time was higher.

The specific internalization of the $\alpha 2$ -conjugated particles was further confirmed with flow cytometry. To determine the fraction of internalized particles from those sitting on the cell surface, the outside fluorescence was quenched with Trypan blue, and thus only the fluorescence from internalized particles recorded. Obtained results indicate that significantly more $\alpha 2$ -conjugated particles than control particles were internalized (Figure 56).

Interestingly, when comparing these results to the results of the earlier flow cytometry results, only a small portion of the cell-surface bound control particles seems to be internalized when compared to the same ratio for $\alpha 2$ particles. This suggests that even though there is some unspecific cell-surface binding of

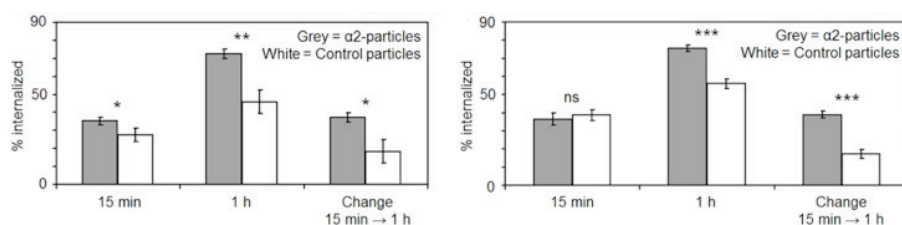


Figure 55. Particles were specifically internalized into cells via $\alpha 2\beta 1$ integrin determined by quantitative confocal segmentation studies. (On the right) Particle concentration was doubled and the experiment repeated.

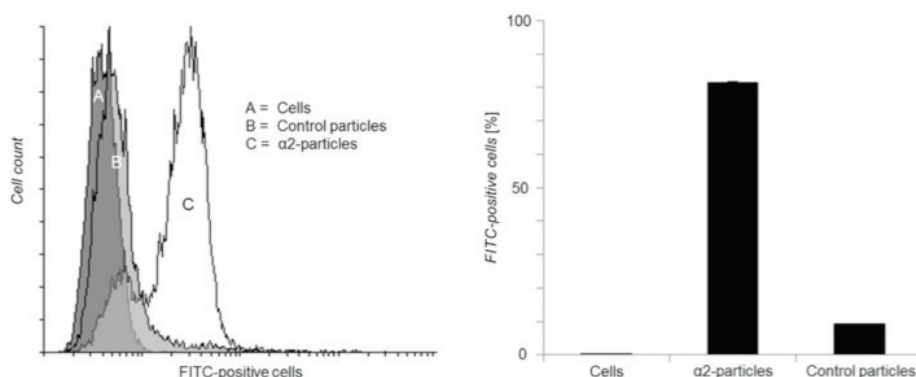


Figure 56. (On the left) Flow cytometry volume plot shows considerably more internalization of $\alpha 2$ -particles than of control particles. (On the right) A flow cytometry histogram of two repeated experiments, indicates that $\alpha 2$ -conjugated particles internalized in a considerably increased manner compared to that of control particles. In the experiment non-internalized surface-bound particles were quenched with Trypan blue.

the control particles, the endocytosis of the particles is more specific than the surface-binding. In turn, this would give support to the usefulness of targeting nanovehicles to endocytic receptors for effective endocytosis.¹⁷⁰

16.3.2.4. Intracellular trafficking

Finally, the aim of the investigation was to clarify the internalization mechanism of the $\alpha 2$ -particles. This was done by confocal co-localization studies based on the same principles as introduced above. Co-localization of $\alpha 2$ -particles was determined using seven known internalization markers: Caveolin-1 for the caveolar pathway; monosialotetrahexosylganglioside (GM1) for the macropinosytosis pathway; Transferrin 2 (TFR2), Rab5 (early endosomes) and Early endosome antigen 1 (EEA1) for the clathrin-mediated pathway; Rab7 for late endosomes; and Lysosomal-associated membrane protein 1 (LAMP1) for late endosomes and lysosomes. Each marker was visualized with antibodies linked to the Alexa555 fluorescent dye and imaged one-by-one together with the fluorescent nanoparticles. Imaging was conducted at the time points of 15 min and 1 h. Based on earlier studies, integrin $\alpha 2\beta 1$ is thought to internalize via a macropinocytotic mechanism into Caveolin-1 positive structures and further into late endosomal structures.^{168,169,171} In accordance with these results, $\alpha 2$ -particles were determined to co-localize significantly with the macropinosytosis marker GM1, Caveolin-1, and Rab7, a typical late endosome marker (Figure 57).

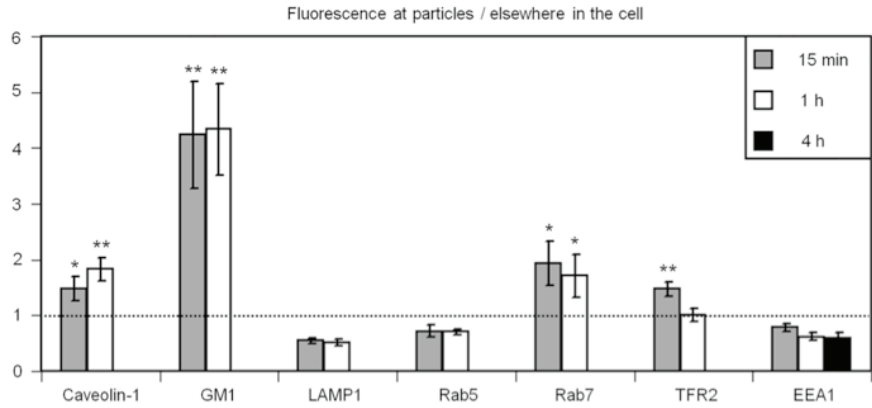


Figure 57. Particles were internalized via specific route(s) characteristic of $\alpha 2 \beta 1$ integrin-mediated internalization. The specific internalization route was determined by co-localization studies quantified by segmentation based confocal imaging. The diagram shows the fluorescence ratios for each marker compared to particles elsewhere in the cells.

16.4. Summary of the results

The results obtained by flow cytometry, confocal microscopy and atomic force microscopy indicates that the $\alpha 2$ monoclonal antibody-conjugated nanoparticles can be targeted specifically towards their receptor, $\alpha 2 \beta 1$ -integrin. Quantitative segmentation analysis of nanoparticle trafficking inside the cell indicates that the particles enter cells via a macropinocytosis-like process and end up in caveolin-1 positive structures, which is similar to the internalization process of $\alpha 2 \beta 1$ integrin-echovirus-1.

The obtained results clearly support the potential of nanoparticles as tools for molecular imaging, as it was possible by an appropriate image analysis to conduct sensitive and complex analyses of the small fluorescent particles inside cells by using basic confocal microscopy images.

17. Article IV

The purpose of Paper IV was to prepare mesoporous imageable and targetable silica nanoparticles with the aim of delivering a poorly water-soluble molecular drug, a gamma-secretase inhibitor (GSI) ($\{N-[N-(3,5\text{-Difluorophenacetyl})\text{-L-alanyl}]\text{-S-phenylglycine-butyl ester}\}$) (DAPT).

The regulation of Notch signaling in cells is of high interest as it is a key regulator of stem cells and is frequently over activated in various types of cancer. It is often linked to aggressive forms of cancer, making Notch an exciting therapeutic target. Notch is in principle “druggable” by γ -secretase inhibitors (GSIs), inhibitory peptides, and antibodies, but clinical use of Notch inhibitors is restricted because it causes severe side effects. There is, therefore, a demand for an alternative cancer-targeted therapy.

17.1. Construction of the particles

Amino-functionalized co-condensed mesoporous silica nanoparticles (MSN) were synthesized in two different sizes. The synthesis was modifiable in relation to the produced particle size, as $H_2O:MeOH$ ratio of 60:40 was used to obtain particles with a diameter of 250 nm while $H_2O:MeOH$ ratio of 50:50 was used to synthesize particles with a diameter of 350 nm. After extraction, particles were surface functionalized either with fluorescein isothiocyanate (FITC) for *in vitro* or Alexa750 succinimidyl ester for *in vivo* experiments. These functional fluorophores reacted with the amino groups introduced into the particle structure during the co-condensation synthesis. Afterward, the particle functionalization was carried out by surface-grown polyethyleneimine (PEI) polymerization. As discussed, the PEI-layer provides an increased number of anchoring groups and therefore facilitates efficient further modifications such as coupling of high amount of the targeting ligands and increased suspension stabilization. In the next functionalization step the targeting ligand, folic acid (FA), was conjugated to the primary amino groups of PEI. Zero-length cross-linker 1-ethyl-3-(3-dimethylaminopropyl) carbodiimide (EDC) was used to activate the carboxylic acid groups of FA to enable the forming of peptide binding. The drug loading with DAPT was conducted on vacuum dried, surfactant extracted particles by suspending the particles in cyclohexane. DAPT was dissolved in cyclohexane with either 1 or 5 wt-% with regard to the particle mass.

17.2. Characterization by the set of standard techniques

SEM images of the prepared 200 nm MSNs and 350 nm MSNs confirms the uniformity of the particles (Figure 58). SAXD pattern measured at a low-angle $2.2^\circ 2\theta$ reveals the ordered pore structure of the particles and, further, the ni-

trogen sorption isotherm confirms the mesoporosity of the particles (Figure 59). Calculated from the sorption data, the 200 nm-Alexa750-labeled particles have a specific surface area (BET) of 1116 m²/g, pore volume (V_p) of 0.65 cm³/g, and d -spacing (d_p) of 3.5 nm determined by NLDFT. DLS measurements in HEPES buffer pH 7.2 of FA-conjugated fluorescent MSNs confirms their redispersibility after all functionalization and drying steps. The overlapping curves for given particle sizes shows curves measured at different times for the same particle batch. The zeta potential was measured in HEPES buffer giving values of 52 mV and 41 mV before and after the FA-conjugation indicating a successful surface modification (Figure 60).

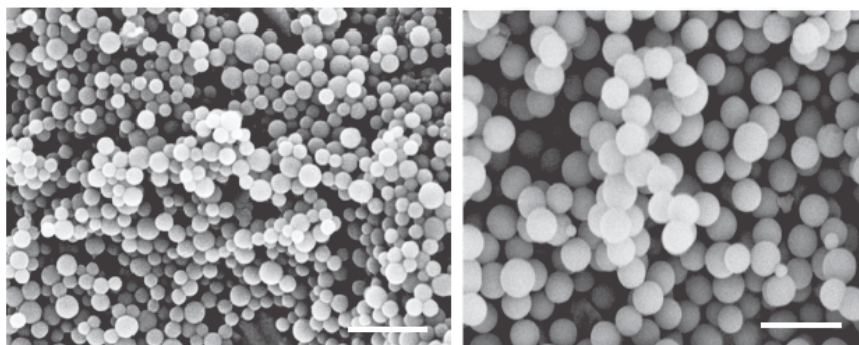


Figure 58. SEM images of particles used for intravenous injections. (On the left) 200 nm and (on the right) particles with an average size of 350 nm. 20kx magnification, scale bar 1 μ m.

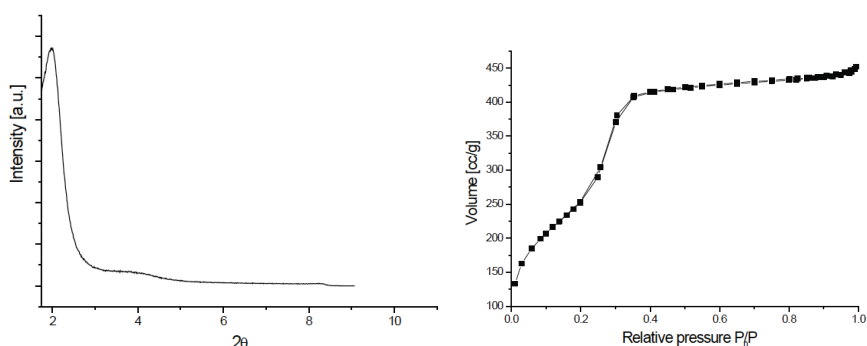


Figure 59. (On the left) SAXD pattern reveals the ordered pore structure of 200 nm Alexa750 labeled particles. (On the right) Adsorption-desorption isotherm of 200 nm-Alexa750 labeled particles.

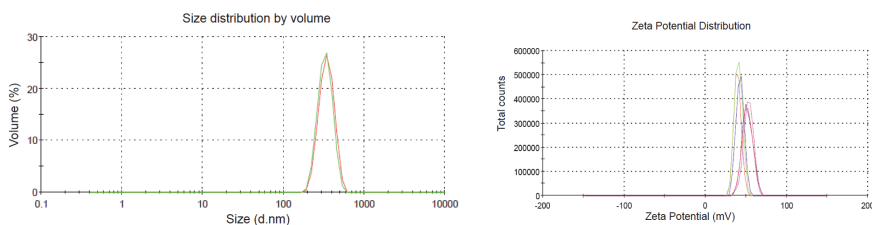


Figure 60. (On the left) Particles were uniform in size. (On the right) Zeta potential was measured before and after functionalization.

17.3. Targeting of the prepared particles *in vitro*

17.3.1. Flow cytometry

The targetability of the particles was assessed *in vitro* by using cell-lines expressing different levels of the folate receptor (FR), and FR high (HeLa) and FR low (HEK 293) cells and applying either MSN-PEI-FA or MSN-PEI particles to the cells at a concentration of 10 $\mu\text{g/mL}$. The relative amount of endocytosed particles was analyzed by flow cytometry. To further assess the apoptotic cell death, the cells were incubated in the presence of 10 $\mu\text{g/mL}$ nanoparticles for 72 hours. Propidium iodide incubation was applied to reveal the fraction of dead cells. Results indicate that FA-conjugated MSNs were specifically taken up by the FR-expressing cells and were further shown to be non-cytotoxic (Figure 61) in agreement with previous results obtained for similar particles.^{107,76,173}

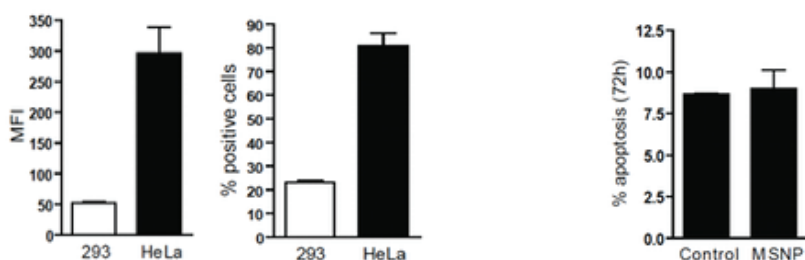


Figure 61. The specificity of MSN-PEI-FA towards the FA receptor was assessed by applying particles on the cells *in vitro* by using cell-lines expressing different levels of the folate receptor (FR), and FR high (HeLa) and low (HEK 293) cells. Specific ligand-lacking MSN-PEI particles was used as a particle control. (On the left) FACS histogram presents that particles are targeted specifically to the FR overexpressing HeLa cells. (Y axis denotes mean fluorescent intensity (MFI)). On the right) No particle-induced toxicity was observed.

17.3.2. Luciferase-based reporter assay

The effect of using GSIs such as DAPT for therapeutic purpose is based on the following principle. When Notch binds to Jagged or Delta ligands, the Notch receptor is subjected to proteolytic processes that release the Notch intracellular domain (NICD), which then translocates to the nucleus where it regulates Notch-dependent gene expression. The cleavage of NICD is mediated by the γ -secretase (GS) complex. In this way gamma secretase inhibitors (GSI) inhibit the cleavage process (Figure 62).

Luciferase-based reporter assay was used to determine cell-specific particle-induced Notch inhibition. GSI-loaded MSNs conjugated either with or without folic acid (Figure 63) were used to determine the targeting and further inhibition of Notch activity. GSI-MSN-FA was determined to specifically block the Notch activity in a dose-dependent manner in FR-high cells as compared to FR-low cells. The targeting function was further confirmed as the Notch inhibition was detected only in the FR-high expressing cells. Importantly, this also demonstrated the lack of premature leakage of the drug into the cell medium, as leakage into the medium would have inhibited Notch in FR-low cells (Figure 64). To confirm further the lack of premature drug leakage, high-pressure liquid chromatography (HPLC) was used to determine the concentration of the drug in medium under mimicked extracellular conditions.

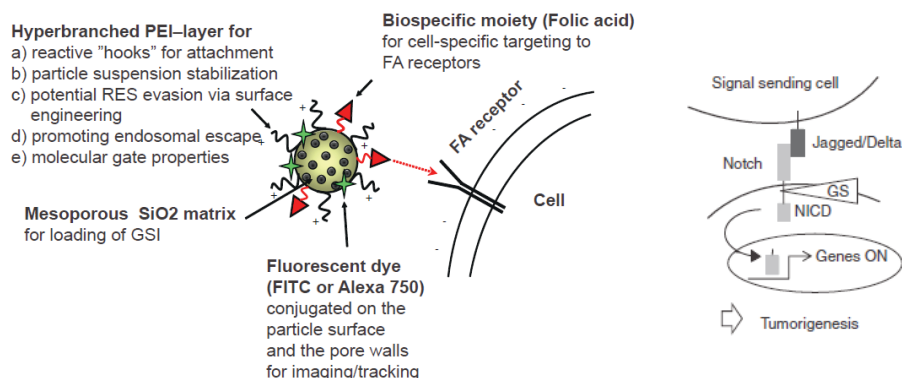


Figure 62. (On the left) A schematic presentation of the particle structure. (On the right) The principle of Notch inhibition induced by GS inhibitors.

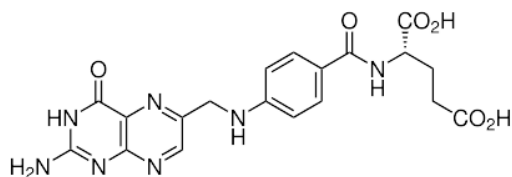


Figure 63. Folic acid was used as targeting ligand.¹⁷²

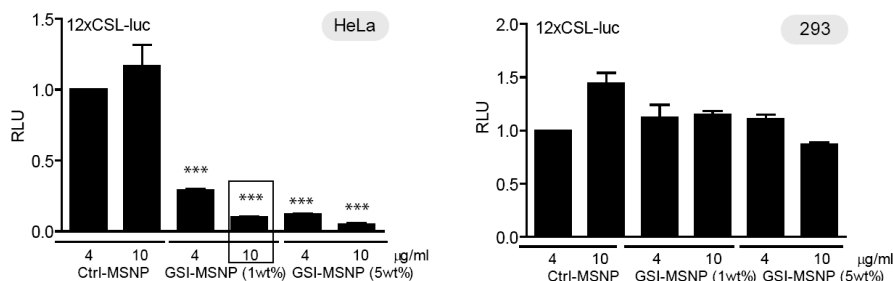


Figure 64. The luciferase reporter assay, which was carried out to determine the Notch activity *in vitro*. Particles were incubated 24 hours with FR-high HeLa cells and FR-low 293 cells. GSI-MSNs are particles loaded with 1 wt-% and 2.5 wt-% GSI. Control MSNs (Ctrl-MSNs) are particles containing no drug. The particles were FA-conjugated in all cases. The x-axis presents the particle concentration ($n \geq 3$; mean \pm SD), while y-axis denotes the relative luciferase units (RLU).

17.4. Targeting enhances tumor penetration and retains MSNs at the tumor site *in vivo*

17.4.1. Peritumoral injections

Tumor accumulation of nanoparticles *in vivo* is facilitated by a combination of passive and active targeting. The main objective of active targeting is to enhance interactions with tumor cells to facilitate cellular uptake and retain the drug carrier within the tumor. To verify active targeting *in vivo*, FA-MSNs and PEI-MSNs, lacking the targeting ligand, were administered through peritumoral (p.t.) (20 mg/kg) injections in nude mice bearing subcutaneous MDA-MB-231 tumors. *In vivo* tracking was facilitated through covalent attachment of the far-red fluorophore Alexa750 to the particles. All particle batches were prescreened with an IVIS set-up to determine the signal to concentration ratio in order to ensure comparability between different particle batches. After the administration, an enhanced tumor retainment and increased tumor

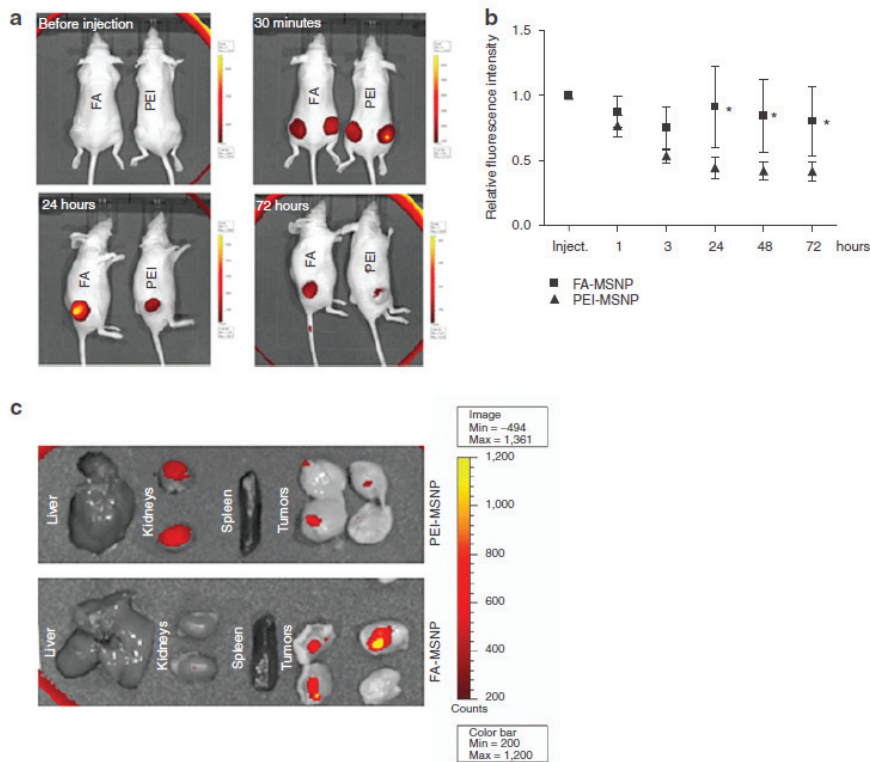


Figure 65. a) Tumor accumulation and retention of PEI-MSN-FA nanoparticles. PEI-MSN-FA and PEI-MSN used as control were injected p.t. and followed by IVIS imaging for 72 h. Scale bars in the images range from 300 to 8000 counts for images 30 min to 72 h. The control image is taken before the injection and has a scale bar of 200 to 4500 counts. b) Quantification of the fluorescence intensity in tumors injected with FA-MSNs and PEI-MSNs over time as related to the initial intensity within each tumor ($n = 6$, two tumors per animal) ($*P < 0.05$). c) Ex vivo imaging of internal organs and tumors 72 h after injection of MSNs. The tumors were further cut in half to visualize particles within the tumor tissue.

penetration of FA-MSNs were observed as compared to that of PEI-MSNs (Figure 65a–b). This result was further supported by *ex vivo* analyses of isolated tumors (Figure 65c). To conclude, an improved tumor retention and penetration of MSNs *in vivo* were achieved through conjugation of targeting ligands.

17.5. GSI-loaded MSNs show enhanced Notch inhibition as compared to a free drug *in vivo*

17.5.1. Peritumoral injections

To verify the applicability of MSNs for delivery of GSIs *in vivo*, the therapeutic efficacy GSI-loaded FA-tagged particles (GSI-MSNs) was validated in mice bearing MDA-MB-231 tumors expressing high Notch activity. The therapeutic efficacy of particle-mediated GSI delivery was compared to the efficacy achieved with free GSI delivery. Rizzo *et al.* recently reported that mice with MDA-MB-231 tumors, consisting of cells expressing high intrinsic Notch activity, were treated by p.t. injections of 1.2 mg/kg GSI every second day for 2 weeks which led to reduced tumor growth.¹⁷⁴ Here, GSI loaded particles were administered 1 mg/kg GSI every 3rd day for 12 days after which the treatment was terminated and the mice were left untreated for an additional 2 weeks. According to the obtained results in our study, treatment with GSI loaded particles clearly reduced tumor growth and the effect was detectable even 2 weeks after the last injection (Figure 66a). In contrast to the same administration procedure of free GSI had no effect on tumor growth (Figure 66b). Consequently, the levels of Notch intracellular domain were clearly reduced (inhibition of Notch activity) in tumors treated with GSI-loaded particles as compared to tumors treated with control particles, analyzed by western blotting (Figure 66c).

17.6. Evaluation of the biocompatibility of MSNs administered through the intravenous and peritumoral routes

In order to evaluate the biocompatibility of the developed MSNs, the particles were tracked both after p.t. (20 mg/kg) (Figure 67) and after intravenous (i.v.) (20 mg/kg) administration (Figure 68).

Within a few hours after the p.t. injection, a strong fluorescent signal was shown in the bladder, which indicates urine excretion of non-retained particles (Figure 67a). Further, at the 48 h time point, the signal in the bladder had reduced below the detection limit, indicating that the majority of particles which were not taken up by the cancer cells were eliminated within 2 days. This was supported also by particle dissolution tests in biological media, demonstrating 70 % reduction of the particle mass of MSNs in 50 h (Figure 70). The biodegradation and renal excretion were further supported by the inductively coupled plasma and optical emission spectrometry (ICP-OES) analyzes of the silica content in the urine collected from the mice at 4 and 24 h time points after i.v. injection (Figure 71). However, particles that were uptaken by cells dissolved at a slower rate¹⁰⁷ and 72 h after injection FA-conjugated particles or parts of them were still observed in the tumors.

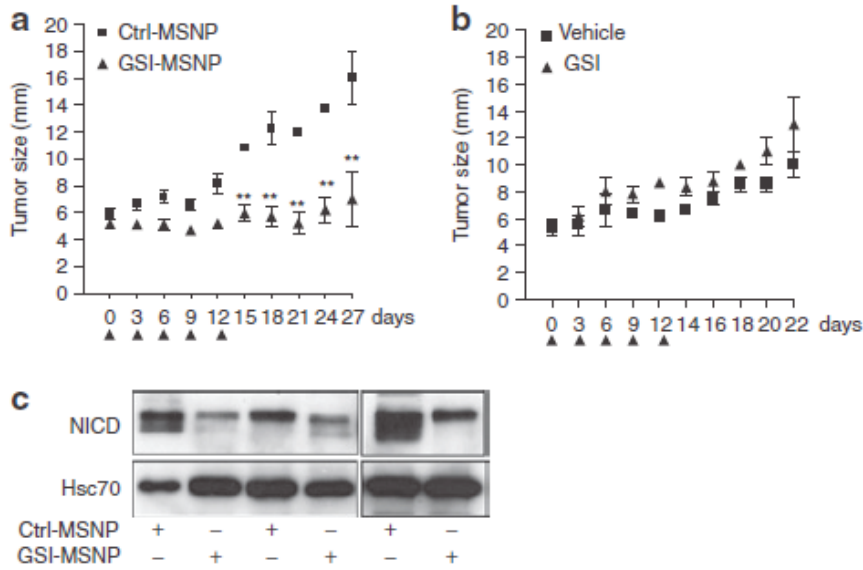


Figure 66. DAPT-loaded mesoporous silica nanoparticles (MSNs) block Notch activity, inhibit tumor growth, and control stem cell functions in vivo. a) MDA-MB-231 tumor-bearing mice were injected p.t. with FA-conjugated GSI-loaded (GSI-MSN, 20 mg/kg, 2.5 wt-% GSI) and empty MSNs were used as a control (Ctrl-MSN, 20 mg/kg) up to 12 days. The tumor size was followed for 3 weeks ($n = 6$, mean \pm SD) (** $P < 0.011$). b) MDA-MB-231 tumor-bearing mice were injected p.t. with 1 mg/kg free DAPT or the DMSO aqueous vehicle solution (Vehicle) up to 12 days. The tumor size was followed until day 22 ($n = 4$, mean \pm SD). c) p.t. treatment of GSI-MSN leads to reduced active Notch levels of in the tumors, as demonstrated by western blotting. Here Notch was detected by an antibody recognizing the intracellular domain (NICD), the active form of Notch.

After i.v. injections (20 mg/kg) tumor accumulation was observed within 12 h, and they remained visible at the tumor site at 120 h (Figure 68). The reported specific tumor accumulation was further determined and supported by ex vivo analyses of isolated organs at 196 h after particle administration (Figure 69b). Furthermore, to analyze the significance of active targeting, the signal was quantified at 72 h time point after injection ex vivo in organs of animals that had injected i.v. with PEI-MSNs and FA-MSNs.

Both particles with the targeting function (FA-MSNs) and particles lacking the targeting ligand accumulated preferably to tumors. This phenomenon can be interpreted as a sign of passive targeting. Generally, after 72 h the targeted and non-targeted particles showed quite similar distribution *in vivo*.

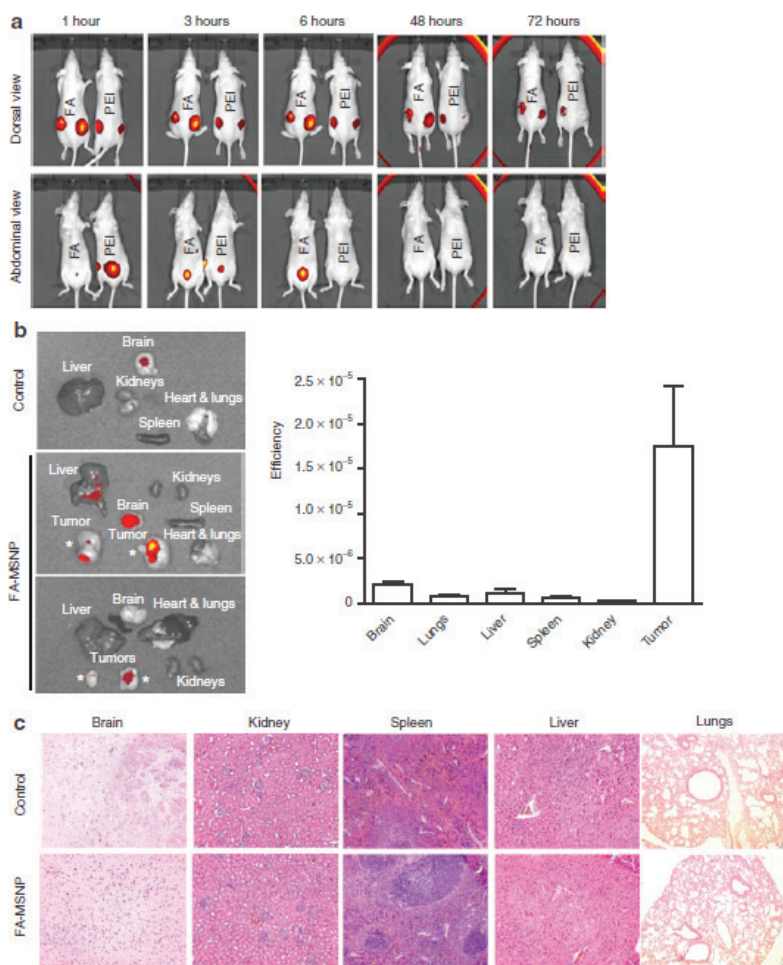


Figure 67. MSNs accumulate in the tumors. They are biocompatible, biodegradable, and mainly eliminated through renal excretion. a) In vivo imaging of mice injected p.t. with PEI-MSNs or FA-PEI-MSNs. IVIS images of the abdominal area show accumulation of fluorescence in the bladder and imaging of the dorsal area presents accumulation of fluorescence in the tumors. Fluorescence was eliminated from the bladder within 48 h after the injections (number of animals per group, $n = 4$, two tumors per animal). b) i.v. administration of FA-MSNs. Ex vivo images of organs (on the left) and fluorescence intensity quantification (on the right). All examined animals were killed 196 h after injection ($n = 4$). Please note the occasional signal from the brain tissue. This is most likely background fluorescence, as it is present also in untreated control animals. (c) The conducted histological analysis of brain, kidney, spleen, liver, and lungs of untreated mice and FA-MSNs-treated mice. This showed no morphological changes. All animals were killed 192 h after i.v. injection.

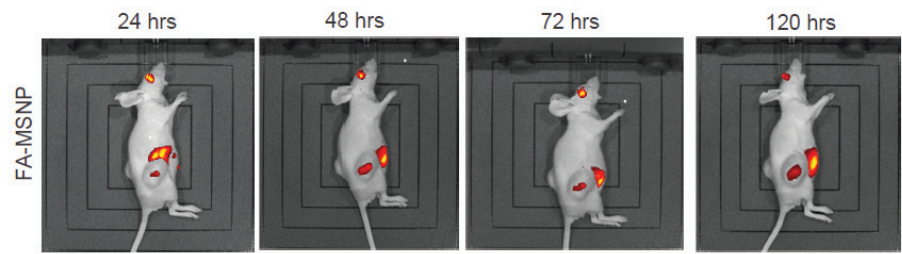


Figure 68. Particles administered through i.v. injections (20 mg/kg) show positive tumor accumulation. Particles remained visible at the tumor site up to 120 hours after administration.

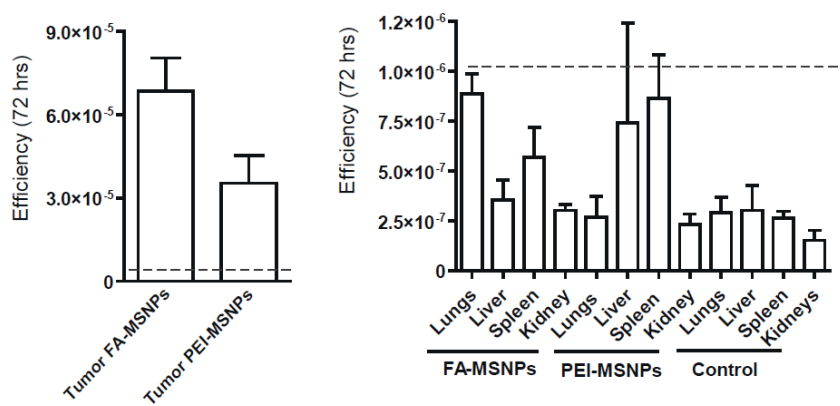


Figure 69. The targeted and non-targeted particles were determined to have quite similar in vivo distribution at 72 hours time point after i.v. injection. Both particles showed signs of renal excretion.

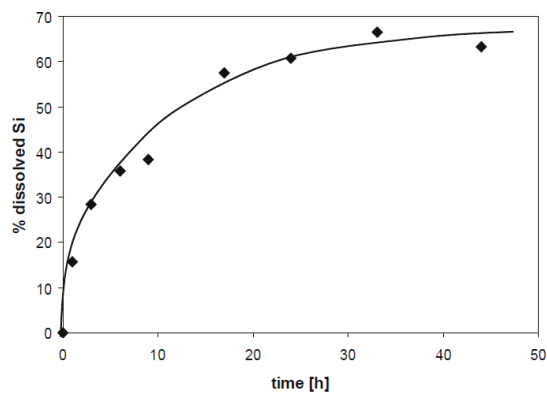


Figure 70. Dissolution of MSNs $120 \mu\text{g ml}^{-1}$ in 25 mM HEPES buffer (pH 7.2, 37 °C) as a function of time.

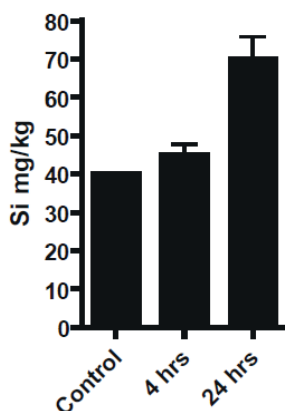


Figure 71. ICP-OES analyzes of the silica content in the urine of mice. Samples were collected at 4 and 24 h time points after i.v. injection. The silica concentration in urine increases with time, which supports the biodegradation of particles and their renal excretion.

Both particles appeared to be biodegradable and were eliminated with the exception of accumulation of FA-tagged particles in the lungs (Figure 68). However, in 196 h the fluorescent signal from the lungs in the mice injected with FA-MSNs was no longer detectable, which supports the efficient biodegradation and elimination of the particles.

Moreover, mice treated with FA-MSNs showed no pathological abnormalities in major organs (Figure 67d). Eight days after i.v. administration, a gross histology of brain, liver, spleen, kidneys, and lungs isolated from treated and control mice was concluded to be identical (Figure 67c). Generally, the animals tolerated particle treatment well and the body weight of the mice did not change during treatment; there were, moreover, no signs of reduced food intake, impaired mobility or visible infections. As the kidneys through the urine excretion were determined to be the main route of elimination, kidney function was analyzed by measuring serum creatinine levels in untreated mice and in mice treated with PEI-MSNs or FA-MSNs. Significant elevation of creatinine levels was detected, which indicates that kidney function was not impaired.

17.7. Summary of the results

In this study, the targetability of MSNs was demonstrated both *in vitro* and *in vivo*. The GSI-loaded MSNs showed therapeutic efficacy through targeted inhibition of gamma secretase leading to reduced Notch signaling activity, which was seen as a halt of the tumor growth *in vivo*. The enhanced therapeutic efficacy was evaluated by using a free drug at the corresponding concentrations as a control. MSNs-mediated GSI delivery *in vivo* provided a significant therapeutic benefit compared to free drug administration, as the free drug was virtually noneffective at inhibiting tumor growth. An added value of the particle-mediated drug delivery is the possibility of using lower drug concentrations and a dosing with lower frequency compared to the administration of a free drug. These results are encouraging also on a general level, as using MSNs as delivery vehicles for GSI, or any other drug, especially those with severe side effects, may also allow for the use of drug concentrations below the systemic toxicity limit. Moreover, the MSNs were shown to be biocompatible, biodegradable, and eliminated mainly by renal excretion.

Conclusions and outlook

Silica nanoparticles with targeting and tracing functions were prepared; the functionalities were confirmed both *in vitro* and *in vivo*. Furthermore, studies related to the biocompatibility and dispersion stability of the particles in biomedical conditions supported the potential of versatile silica platforms for personalized medicine.

The properties of nanoparticles are highly size-dependent, and thus good dispersion stability is a prerequisite for an active theranostic agent. Particle physico-chemical characteristics such as the surface functionalization have high influence on the colloidal properties, which is seen from the provided results indicating that the stability of the particle suspensions is crucially dependent on all functional groups present on the particle surface. It was shown that by the proper choice of surface functionalization route, traceable streptavidin conjugated particles, stable in physiological conditions can be prepared. The added value of conjugating streptavidin on the particle surface is its exceptionally high affinity to its water-soluble ligand biotin (vitamin H), which enables its binding to a wide variety of biotin-antibody complexes and further targeting of nanoparticles to cell receptors of interest.

The biomedical environment consists of aqueous media and therefore theranostic agents should possess hydrolytic stability in a magnitude that enables the particles to remain stable (intact) in the body the time scales needed to accomplish their task, followed by dissolution and degradation of the particle matrix. Therefore targeting groups should stay on the particle surface until the particles have been internalized, after which the degradation should take place to facilitate the release of the particle-incorporated drug and to prevent particle material-induced toxicity. The degradation of silica nanoparticles was evaluated by preparing a model particle in which all particle functionalities were labeled with a different fluorophore. The particle design, together with light microscopy and image analysis, enabled a detailed study of the degradation process *in vitro*, thus supporting the biocompatibility of silica particles in nanomedicine. The obtained results clearly suggest that the PEI layer, modeling generally the particle functionalities, is detached from the rest of the particle, most probably both in the form of free PEI and PEI attached to fragments of the outmost particle structure, in this case mesoporous silica. This degradation process was preferentially detected inside the cells. These results further suggested that covalent attachment of drugs, targeting groups, or other functionalities and their subsequent intracellular detachment is a promising route towards intrinsically-triggered intracellular release. These results also demonstrated new imaging-based methodology that can be used to effectively analyze the degradation of nanoparticles inside cells.

Silica nanoparticles were successfully targeted and also simultaneously used to deliver therapeutic agents *in vitro* and *in vivo*. Nonporous nanoparticles using monoclonal antibodies as guiding agents were examined *in vitro* to study their targetability and internalization. In addition to successful targetability, a specific cell entry route was detected. In a separate study, *in vivo*-traceable mesoporous nanoparticles loaded with a hydrophobic cancer drug conjugated with a small molecular targeting ligand was demonstrated for *in vitro*- and *in vivo*-targeted drug delivery. Drug-characteristic pathway inhibition was observed, which led to enhanced tumor shrinkage and to a significantly improved therapeutic outcome. The enhanced therapeutic efficacy of particle-mediated delivery was evaluated by using a free drug at corresponding concentrations as a control. The particle-mediated drug delivery *in vivo* was reported to provide a significant therapeutic benefit compared to an administered free drug. Moreover, the demonstrated therapy of using mesoporous silica nanoparticles was shown to be biocompatible, biodegradable, and eliminated mainly by renal excretion.

It would, in the future research, be attractive to optimize *in vivo* biodistribution of particles aimed for theranostics. Preparing traceable and targetable silica nanoparticles for biomedical use would require special attention to be paid on particle dispersion stability, biocompatibility and targeting capabilities to optimize their use in biological systems, similar to the present study. Particle functionalization could provide new means for instance to control the protein adsorption on the particles and particles' interaction with RES. One very important parameter controlling the biodistribution is the particle size. Monoclonal antibodies are a group of very versatile ligands "allowing specificity to almost any extracellular cell-surface target" and thus targeting using mAb's would be attractive also in the future research.

Acknowledgements

The present work was carried out at the Laboratory of Physical Chemistry, at Åbo Akademi University, Turku, Finland and at the Laboratory of Inorganic Chemistry II, University of Ulm, Germany, during years 2008–2013.

First of all, I would like to thank my supervisor Professor Mika Lindén for the invaluable advice, support, inspiring guidance and positive attitude during working with my thesis. I would like to thank him for providing me an opportunity to work in his group at the Laboratory of Inorganic Chemistry II, University of Ulm, Germany, for 15 months, this time was really extraordinary.

I would like to thank Professor Jouko Peltonen for providing me an opportunity to finalize my thesis at the Department of Physical Chemistry. I would like also to thank the former Professor Jarl B. Rosenholm. I am honored to have Adjunct Professor Dr. Hélder A Santos from Division of Pharmaceutical Chemistry and Technology, University of Helsinki, Finland and Associate Professor Freddy Kleitz from Department of Chemistry, Université of Laval, Quebec, Canada as the reviewers of this thesis.

Special thanks to my co-authors and colleagues, past and present, it has really been rewarding working with you all. I would like to thank all the personnel at the Laboratory of Physical Chemistry, Åbo Akademi University, the personnel at Laboratory of Inorganic Chemistry II, University of Ulm, the personnel at Research Affairs and at Technology Transfer Office, Åbo Akademi University for their support and most of all creating a cheerful working environment.

Finally, I want to thank my friends and family for the support I would never have been able to cope without.

Turku, August 2014
Lotta Bergman

References

1. Stöber, W., Fink, A. & Bohn, E. Controlled growth of monodisperse silica spheres in the micron size range. *J. Colloid Interface Sci.* **26**, 62–69 (1968).
2. Kresge, C. T., Leonowicz, M. E., Roth, W. J., Vartuli, J. C. & Beck, J. S. Ordered mesoporous molecular sieves synthesized by a liquid-crystal template mechanism. *Nature* **359**, 710–712 (1992).
3. Sing, K. S. W., Everett D.H., Haul, R.A.W., Moscou, L., Pierotti, R.A., Rouquerol, J., Siemieniowska, T. Reporting physisorption data for gas/solid systems, with special reference to the determination of surface area and porosity. *Pure Appl. Chem.* **57**, 603–619, (1984).
4. Hoffmann, F., Cornelius, M., Morell, J. & Fröba, M. Silica-based mesoporous organic-inorganic hybrid materials. *Angew. Chem. Int. Ed.* **45**, 3216–3251 (2006).
5. Grün, M., Lauer, I. & Unger, K. K. The synthesis of micrometer- and submicrometer-size spheres of ordered mesoporous oxide MCM-41. *Adv. Mater.* **9**, 254–257 (1997).
6. Nooney, R. I., Thirunavukkarasu, D., Chen, Y., Josephs, R. & Ostafin, A. E. Synthesis of Nanoscale Mesoporous Silica Spheres with Controlled Particle Size. *Chem. Mater.* **14**, 4721–4728 (2002).
7. Cai, Q., Luo, Z-S Luo, Pang, W-Q, Fan, Y-W., Chen, X-H, Cui, F-Z Cui. Dilute Solution Routes to Various Controllable Morphologies of MCM-41 Silica with a Basic Medium. *Chem. Mater.* **13**, 258–263 (2001).
8. Cai, Q., Cui, F. Z. Cui, Chen, X. H., Zhang, Y., Luo, Z. S. Nanosphere of Ordered Silica MCM-41 Hydrothermally Synthesized with Low Surfactant Concentration. *Chem. Lett.* 1044–1045 (2000).
9. Matijevic, E. Preparation and properties of uniform size colloids. *Chem. Mater.* **5**, 412–426 (1993).
10. Caruso, F., Caruso, R.A., & Mohwald, H. Nanoengineering of inorganic and hybrid hollow spheres by colloidal templating. *Science* **282**, 1111–1114 (1998).
11. Chen, Y., Chen, H., Guo, L., He, Q., Chen, F., Zhou, J., Feng, J., Shi, J. Hollow/Rattle-Type Mesoporous Nanostructures by a Structural Difference-Based Selective Etching Strategy. *ACS Nano* **4**, 529–539 (2010).
12. Tang, F., Li, L. & Chen, D. Mesoporous Silica Nanoparticles: Synthesis, Biocompatibility and Drug Delivery. *Adv. Mater.* **24**, 1504–1534 (2012).
13. Brinker, C. J. & Scherer, G. W. *Sol-gel science: The physics and chemistry of sol-gel processing*. (Academic Press, 1990).

14. Schiestel, T., Brunner, H. & Tovar, G. E. M. Controlled surface functionalization of silica nanospheres by covalent conjugation reactions and preparation of high density streptavidin nanoparticles. *J. Nanosci. Nanotechnol.* **4**, 504–511 (2004).
15. Hermanson, G. T. *Bioconjugate techniques*. (Academic Press, 2008).
16. Huo, Q., Margolese, D.I., Ciesla, U., Feng, P., Gier, T.E., Sieger, P., Leon, R., Petroff, P.M., Schüth, F., Stucky, G.D. Generalized synthesis of periodic surfactant/inorganic composite materials. *Nature* **368**, 317–321 (1994).
17. Fowler, C. E., Khushalani, D., Lebeau, B. & Mann, S. Nanoscale Materials with Mesostructured Interiors. *Adv. Mater.* **13**, 649–652 (2001).
18. Sadasivan, S., Fowler, C. E., Khushalani, D. & Mann, S. Nucleation of MCM-41 Nanoparticles by Internal Reorganization of Disordered and Nematic-Like Silica–Surfactant Clusters. *Angew. Chem. Int. Ed.* **41**, 2151–2153 (2002).
19. Lu, F., Wu, S.-H., Hung, Y. & Mou, C.-Y. Size Effect on Cell Uptake in Well-Suspended, Uniform Mesoporous Silica Nanoparticles. *Small* **5**, 1408–1413 (2009).
20. Lin, V. S.-Y., Lai, C.-Y., Huang, J., Song, S.-A. & Xu, S. Molecular Recognition Inside of Multifunctionalized Mesoporous Silicas: Toward Selective Fluorescence Detection of Dopamine and Glucosamine. *J. Am. Chem. Soc.* **123**, 11510–11511 (2001).
21. Lai, C.Y., Trewyn, B.G., Jeftinija, D.M., Jeftinija, K., Xu, S., Jeftinija, S., Lin, V.S. A Mesoporous Silica Nanosphere-Based Carrier System with Chemically Removable CdS Nanoparticle Caps for Stimuli-Responsive Controlled Release of Neurotransmitters and Drug Molecules. *J. Am. Chem. Soc.* **125**, 4451–4459 (2003).
22. Mizutani, M., Yamada, Y., Nakamura, T. & Yano, K. Anomalous Pore Expansion of Highly Monodispersed Mesoporous Silica Spheres and Its Application to the Synthesis of Porous Ferromagnetic Composite. *Chem. Mater.* **20**, 4777–4782 (2008).
23. Suzuki, K., Ikari, K. & Imai, H. Synthesis of Silica Nanoparticles Having a Well-Ordered Mesosstructure Using a Double Surfactant System. *J. Am. Chem. Soc.* **126**, 462–463 (2004).
24. Vallhov, H., Gabrielsson, S., Strømme, M., Scheynius, A. & Garcia-Bennett, A. E. Mesoporous Silica Particles Induce Size Dependent Effects on Human Dendritic Cells. *Nano Lett.* **7**, 3576–3582 (2007).
25. Lund, K. *Structural and Morphological Studies of Mesoporous Materials*. (Department of Physical, Inorganic and Structural Chemistry, Stockholm university, 2007).
26. Gao, F., Botella, P., Corma, A., Blesa, J. & Dong, L. Monodispersed Mesoporous Silica Nanoparticles with Very Large Pores for Enhanced Adsorption and Release of DNA. *J. Phys. Chem. B* **113**, 1796–1804 (2009).

27. Möller, K., Kobler, J. & Bein, T. Colloidal Suspensions of Nanometer-Sized Mesoporous Silica. *Adv. Funct. Mater.* **17**, 605–612 (2007).
28. Kobler, J., Möller, K. & Bein, T. Colloidal Suspensions of Functionalized Mesoporous Silica Nanoparticles. *ACS Nano* **2**, 791–799 (2008).
29. He, Q., Cui, X., Cui, F., Guo, L. & Shi, J. Size-controlled synthesis of monodispersed mesoporous silica nano-spheres under a neutral condition. *Microporous Mesoporous Mater.* **117**, 609–616 (2009).
30. Berggren, A. & Palmqvist, A. E. C. Particle Size Control of Colloidal Suspensions of Mesostructured Silica. *J. Phys. Chem. C* **112**, 732–737 (2008).
31. Tadros, T. F. *Self-Organized Surfactant Structures*. (John Wiley & Sons, 2011).
32. Holmberg, K., Jönsson, B., Kronberg, B. & Lindman, B. *Surfactants and Polymers in Aqueous Solution*. (John Wiley & Sons, Ltd, 2003).
33. Lind, A., Andersson, J., Karlsson, S., Ågren, P., Bussian, P., Amenitsch, H., Lindén, M. Controlled Solubilization of Toluene by Silicate–Cationic Surfactant Mesophases as Studied by *in Situ* and *ex Situ* XRD. *Langmuir* **18**, 1380–1385 (2002).
34. Johansson, E. Controlling the Pore Size and Morphology of Mesoporous Silica. (Department of Physics, Chemistry and Biology (IFM) Linköping University, 2010).
35. Lindén, M., Schacht, S., Schüth, F., Steel, A. & Unger, K. K. Recent Advances in Nano- and Macroscale Control of Hexagonal, Mesoporous Materials. *J. Porous Mater.* **5**, 177–193 (1998).
36. Ertl, G., Knötzinger, H., Schüth, F., and J. Weitkamp, Eds., *Handbook of Heterogeneous Catalysis*, 2nd edition, Vol 1 (VCH-Wiley, Weinheim, **2008**)
37. Lang, N. & Tuel, A.A. Fast and Efficient Ion-Exchange Procedure To Remove Surfactant Molecules from MCM-41 Materials. *Chem. Mater.* **16**, 1961–1966 (2004).
38. Kawi, S. & Lai, M. W. Supercritical fluid extraction of surfactant from Si-MCM-41. *AIChE J.* **48**, 1572–1580 (2002).
39. Keene, M. T. J., Denoyel, R. & Llewellyn, P. L. Ozone treatment for the removal of surfactant to form MCM-41 type materials. *Chem. Commun.* 2203–2204 (1998)
40. Chen, C., Li, H. & Davis, M. E. Synthesis and characterization of MCM-41. *Microporous Mesoporous Mater.* **2**, 17 (1993).
41. Gogotsi, Y. *Nanomaterials Handbook*. (CRC Press, 2006)
42. Zhuravlev, L. T. Concentration of hydroxyl groups on the surface of amorphous silicas. *Langmuir* **3**, 316–318 (1987).

43. Metin, C. O., Lake, L. W., Miranda, C. R. & Nguyen, Q. P. Stability of aqueous silica nanoparticle dispersions. *J. Nanoparticle Res.* **13**, 839–850 (2011).
44. Malvern Instruments. at <<http://www.malvern.com/en/>>, accessed 11 June 14
45. Sperling, R. A. & Parak, W. J. Surface modification, functionalization and bio-conjugation of colloidal inorganic nanoparticles. *Philos. Trans. R. Soc. Math. Phys. Eng. Sci.* **368**, 1333–1383 (2010).
46. Bergna, H. E. & Roberts. *Colloidal silica: fundamentals and applications*. (CRC Taylor & Francis, 2006).
47. Liu, J. *et al.* Hybrid Mesoporous Materials with Functionalized Monolayers. *Adv. Mater.* **10**, 161–165 (1998).
48. Mercier, L. & Pinnavaia, T. J. Heavy Metal Ion Adsorbents Formed by the Grafting of a Thiol Functionality to Mesoporous Silica Molecular Sieves: Factors Affecting Hg(II) Uptake. *Environ. Sci. Technol.* **32**, 2749–2754 (1998).
49. Lagaly, G. K. K. Unger: *Porous Silica — its properties and use as support in column liquid chromatography*. (Elsevier Scientific Publishing Co., Amsterdam, Oxford, New York 1979)
50. Zhao, X. S. & Lu, G. Q. Modification of MCM-41 by Surface Silylation with Trimethylchlorosilane and Adsorption Study. *J. Phys. Chem. B* **102**, 1556–1561 (1998).
51. Zhuravlev, L. T. The surface chemistry of amorphous silica. Zhuravlev model. *Colloids Surf. Physicochem. Eng. Asp.* **173**, 1–38 (2000).
52. Potapov, V. V. & Zhuravlev, L. T. Temperature Dependence of the Concentration of Silanol Groups in Silica Precipitated from a Hydrothermal Solution. *Glass Phys. Chem.* **31**, 661–670 (2005).
53. Stein, A., Melde, B. J. & Schrodin, R. C. Hybrid Inorganic–Organic Mesoporous Silicates—Nanoscopic Reactors Coming of Age. *Adv. Mater.* **12**, 1403–1419 (2000).
54. Santra, S. & Dutta, D. in *Nanotechnologies Life Sci.* (Wiley-VCH Verlag GmbH & Co. KGaA, 2007)
55. Smith, L., Kuncic, Z., Ostrikov, K. (Ken) & Kumar, S. Nanoparticles in Cancer Imaging and Therapy. *J. Nanomater.* **2012**, (2012).
56. Nooney, R. I., McCormack, E. & McDonagh, C. Optimization of size, morphology and colloidal stability of fluorescein dye-doped silica NPs for application in immunoassays. *Anal. Bioanal. Chem.* **404**, 2807–2818 (2012).
57. Slowing, I. I., Trewyn, B. G., Giri, S. & Lin, V. S.-Y. Mesoporous Silica Nanoparticles for Drug Delivery and Biosensing Applications. *Adv. Funct. Mater.* **17**, 1225–1236 (2007).
58. Kirkey, W. D. *et al.* Optical Properties of Polymer-Embedded Silicon Nanoparticles. *MRS Online Proc. Libr.* **789** (2003)

59. Caruso, F. Nanoengineering of Particle Surfaces. *Adv. Mater.* **13**, 11–22 (2001)
60. Boiteau, R. & Maede, T. Gadolinium-Labeled Nanoparticles for Magnetic Resonance Imaging. *Nanoscope* **5**, (2008).
61. Taylor-Pashow, K. M. L., Rocca, J. D. & Lin, W. Mesoporous Silica Nanoparticles with Co-Condensed Gadolinium Chelates for Multimodal Imaging. *Nanomaterials* **2**, 1–14 (2011).
62. Lim, M. H. & Stein, A. Comparative Studies of Grafting and Direct Syntheses of Inorganic–Organic Hybrid Mesoporous Materials. *Chem. Mater.* **11**, 3285–3295 (1999).
63. Kim, C. O., Cho, S. J. & Park, J. W. Hyperbranching polymerization of aziridine on silica solid substrates leading to a surface of highly dense reactive amine groups. *J. Colloid Interface Sci.* **260**, 374–378 (2003).
64. Xia, T., Kovochich, M., Liong, M., Meng, H., Kabehie, S., George, S., Zink, J.I., Nel, A.E. Polyethyleneimine Coating Enhances the Cellular Uptake of Mesoporous Silica Nanoparticles and Allows Safe Delivery of siRNA and DNA Constructs. *ACS Nano* **3**, 3273–3286 (2009).
65. X. Feng, G. E. F. Functionalized Monolayers on Ordered Mesoporous Supports. *Science* **276**, 923–926 (1997).
66. Caravajal, G. S., Leyden, D. E., Quinting, G. R. & Maciel, G. E. Structural characterization of (3-aminopropyl)triethoxysilane-modified silicas by silicon-29 and carbon-13 nuclear magnetic resonance. *Anal. Chem.* **60**, 1776–1786 (1988).
67. Vrancken, K. C., Possemiers, K., Van Der Voort, P. & Vansant, E. F. Surface modification of silica gels with aminoorganosilanes. *Colloids Surf. Physicochem. Eng. Asp.* **98**, 235–241 (1995).
68. Trens, P. & Denoyel, R. Adsorption of (γ -Aminopropyl)triethoxysilane and Related Molecules at the Silica/Heptane Interface. *Langmuir* **12**, 2781–2784 (1996).
69. Vrancken, K. C., Voort, P. V. D., Gillis-D’Hamers, I., Vansant, E. F. & Grobet, P. Influence of water in the reaction of γ -aminopropyltriethoxysilane with silica gel. A Fourier-transform infrared and cross-polarisation magic-angle-spinning nuclear magnetic resonance study. *J. Chem. Soc. Faraday Trans.* **88**, 3197–3200 (1992).
70. Kallury, K. M. R., Macdonald, P. M. & Thompson, M. Effect of Surface Water and Base Catalysis on the Silanization of Silica by (Aminopropyl)alkoxysilanes Studied by X-ray Photoelectron Spectroscopy and ^{13}C Cross-Polarization/Magic Angle Spinning Nuclear Magnetic Resonance. *Langmuir* **10**, 492–499 (1994).

71. Beck, J.S., Vartuli, J.C., Roth, W.J., Leonowicz, M. E., Kresge, C. T., Schmitt, K. D., Chu, C.T.W., Olson, D.H., Sheppard, E.W. A new family of mesoporous molecular sieves prepared with liquid crystal templates. *J. Am. Chem. Soc.* **114**, 10834–10843 (1992).
72. Sharma, K.K., Anan, A., Buckley, R.P., Ouellette, W. & Asefa, T. Toward efficient nanoporous catalysts: controlling site-isolation and concentration of grafted catalytic sites on nanoporous materials with solvents and colorimetric elucidation of their site-isolation. *J. Am. Chem. Soc.* **130**, 218–228 (2008).
73. Hicks, J. C., Dabestani, R., Buchanan, A. C. & Jones, C. W. Assessing site-isolation of amine groups on aminopropyl-functionalized SBA-15 silica materials via spectroscopic and reactivity probes. *Inorganica Chim. Acta* **361**, 3024–3032 (2008).
74. Radhakrishnan, B., Ranjan, R. & Brittain, W. J. Surface initiated polymerizations from silica nanoparticles. *Soft Matter* **2**, 386–396 (2006).
75. Khan, M. & Huck, W. T. S. Hyperbranched Polyglycidol on Si/SiO₂ Surfaces via Surface-Initiated Polymerization. *Macromolecules* **36**, 5088–5093 (2003).
76. Rosenholm, J.M., Meinander, A., Peuhu, E., Niemi, R., Eriksson, J.E., Sahlgren, C. & Lindén M. Targeting of Porous Hybrid Silica Nanoparticles to Cancer Cells. *ACS Nano* **3**, 197–206 (2009).
77. Casasús, R., Marcos, M.D., Martínez-Mañez, R., Ros-Lis, J.V., Soto, J., Villaesca, L.A., Amorós, P., Beltrán, D., Guillem, C., Latorre, J., Toward the development of ionically controlled nanoscopic molecular gates. *J. Am. Chem. Soc.* **126**, 8612–8613 (2004).
78. Lyatskaya, Y. & Balazs, A. C. Modeling the Phase Behavior of Polymer–Clay Composites. *Macromolecules* **31**, 6676–6680 (1998).
79. Edmondson, S., Osborne, V. L. & Huck, W. T. S. Polymer brushes via surface-initiated polymerizations. *Chem. Soc. Rev.* **33**, 14–22 (2004).
80. Prucker, O. & Rühle, J. Mechanism of Radical Chain Polymerizations Initiated by Azo Compounds Covalently Bound to the Surface of Spherical Particles. *Macromolecules* **31**, 602–613 (1998).
81. Harush-Frenkel, O., Debotton, N., Benita, S. & Altschuler, Y. Targeting of nanoparticles to the clathrin-mediated endocytic pathway. *Biochem. Biophys. Res. Commun.* **353**, 26–32 (2007).
82. Chen, X. & Program, S. of M. P. A., Calif Department of Radiology and Bio-X. *Recent Advances of Bioconjugation Chemistry in Molecular Imaging: 2008* (Research Signpost, 2008).
83. Timkovich, R. Detection of the stable addition of carbodiimide to proteins. *Anal. Biochem.* **79**, 135–143 (1977).
84. *Cross-Linking Reagents - Technical Handbook*. <www.piercenet.com/xlink95d>, accessed 11 June 14

85. O,O'-Bis[2-(N-Succinimidyl-succinylamino)ethyl]polyethylene glycol. *Sigma-Aldrich* at <<http://www.sigmaaldrich.com/catalog/product/aldrich/713783?lang=fi®ion=FI>>, accessed 11 June 14
86. Cai, W., Shin, D.W., Chen, K., Gheysens, O., Cao, Q., Wang, S.X., Gambhir, S.S., Chen, X. Peptide-labeled near-infrared quantum dots for imaging tumor vasculature in living subjects. *Nano Lett.* **6**, 669–676 (2006).
87. Jun, Y-W., Huh, Y-M., Choi, J-S., Lee, J-H., Song, H-T., Yoon, S., Kim, K-S., Shin, J-S., Suh, J-S., Cheon, J., Nanoscale Size Effect of Magnetic Nanocrystals and Their Utilization for Cancer Diagnosis via Magnetic Resonance Imaging. *J. Am. Chem. Soc.* **127**, 5732–5733 (2005).
88. González, M., Bagatolli, L.A., Echabe, I., Arrondo, J.L., Argaraña, C.E., Cantor, C.R., Fidelio, G.D. Interaction of Biotin with Streptavidin. Thermostability and conformational changes upon binding. *J. Biol. Chem.* **272**, 11288–11294 (1997).
89. Shrake, A. & Ross, P. D. Ligand-induced biphasic protein denaturation. *J. Biol. Chem.* **265**, 5055–5059 (1990).
90. Streptavidin Biotin Interaction. <<http://amber.scripps.edu/tutorial/streptavidin/index.html>>, accessed 11 June 14
91. Bae, S. W., Tan, W. & Hong, J.-I. Fluorescent dye-doped silica nanoparticles: new tools for bioapplications. *Chem. Commun.* **48**, 2270–2282 (2012).
92. Bergman, L., Kankaanpää, P., Tiitta, S., Duchanoy, A., Li, L., Heino, J., Lindén, M. Intracellular Degradation of Multilabeled Poly(Ethylene imine)–Mesoporous Silica–Silica Nanoparticles: Implications for Drug Release. *Mol. Pharm.* **10**, 1795–1803 (2013).
93. Jiang, S., Gnanasammandhan, M. K. & Zhang, Y. Optical imaging-guided cancer therapy with fluorescent nanoparticles. *J. R. Soc. Interface* **7**, 3–18 (2010).
94. Accomasso, L., Cibrario, R.E., Raimondo, S., Catalano, F., Alberto, G., Giannitti, A., Minieri, V., Turinetto, V., Orlando, L., Saviozzi, S., Caputo, G., Geuna, S., Martra, G., Giachino, C. Fluorescent silica nanoparticles improve optical imaging of stem cells allowing direct discrimination between live and early-stage apoptotic cells. *Small* **8**, 3192–3200 (2012).
95. Matsushita, H., Mizukami, S., Sugihara, F., Nakanishi, Y., Yoshioka, Y., Kikuchi, K. Multifunctional Core–Shell Silica Nanoparticles for Highly Sensitive ¹⁹F Magnetic Resonance Imaging. *Angew. Chem. Int. Ed.* **53**, 1008–1011 (2014).
96. Taylor, K.M.L., Kim, J.S., Rieter, W.J., An, H., Lin, W., Lin, W. Mesoporous Silica Nanospheres as Highly Efficient MRI Contrast Agents. *J. Am. Chem. Soc.* **130**, 2154–2155 (2008).
97. Lee, S.B., Kim, H.L., Jeong, H-J., Lim, S.T., Sohn, M-H., Kim, D.W. Mesoporous Silica Nanoparticle Pretargeting for PET Imaging Based on a Rapid Bioorthogonal Reaction in a Living Body. *Angew. Chem. Int. Ed.* **52**, 10549–10552 (2013).

98. Joshi, R., Feldmann, V., Koestner, W., Detje, C., Gottschalk, S., Mayer, H.A., Sauer, M.G., Engelmann, J. Multifunctional silica nanoparticles for optical and magnetic resonance imaging. *Biol. Chem.* **394**, 125–135 (2013).
99. Wickline, S. A. & Lanza, G. M. Nanotechnology for Molecular Imaging and Targeted Therapy. *Circulation* **107**, 1092–1095 (2003).
100. Massoud, T. F. & Gambhir, S. S. Molecular imaging in living subjects: seeing fundamental biological processes in a new light. *Genes Dev.* **17**, 545–580 (2003).
101. Minchin, R. F. & Martin, D. J. Minireview: Nanoparticles for Molecular Imaging—An Overview. *Endocrinology* **151**, 474–481 (2010).
102. Gao, H., Yang, Z., Zhang, S., Cao, S., Shen, S., Pang, Z., Jiang, X. Ligand modified nanoparticles increases cell uptake, alters endocytosis and elevates glioma distribution and internalization. *Sci. Rep.* **3**, (2013).
103. Geisow, M. Fluorescein conjugates as indicators of sub cellular pH a critical evaluation. *Exp. Cell Res.* **150**, 29–35 (1984).
104. Ghoroghchian, P. P., Therien, M. J. & Hammer, D. A. In vivo fluorescence imaging: a personal perspective. *Wiley Interdiscip. Rev. Nanomed. Nanobiotechnol.* **1**, 156–167 (2009).
105. Tsai, C.-P., Chen, C.-Y., Hung, Y., Chang, F.-H. & Mou, C.-Y. Monoclonal antibody-functionalized mesoporous silica nanoparticles (MSN) for selective targeting breast cancer cells. *J. Mater. Chem.* **19**, 5737–5743 (2009).
106. Milgroom, A., Intrator, M., Madhavan, K., Mazzaro, L., Shandas, R., Liu, B., Park, D. Mesoporous silica nanoparticles as a breast-cancer targeting ultrasound contrast agent. *Colloids Surf. B Biointerfaces* (2013).
107. Rosenholm, J.M., Peuhu, E., Bate-Eya, L.T., Eriksson, J.E., Sahlgren, C., Lindén, M. Cancer-cell-specific induction of apoptosis using mesoporous silica nanoparticles as drug-delivery vectors. *Small* **6**, 1234–1241 (2010).
108. Yu, M.K., Park, J., Jon, S., Targeting Strategies for Multifunctional Nanoparticles in Cancer Imaging and Therapy. *Theranostics* **2**, 3–44 (2012).
109. Hussey, S. L. & Peterson, B. R. Efficient delivery of streptavidin to mammalian cells: clathrin-mediated endocytosis regulated by a synthetic ligand. *J. Am. Chem. Soc.* **124**, 6265–6273 (2002).
110. Xin, H., Jiang, X., Gu, J., Sha, X., Chen, L., Law, K., Chen, Y., Wang, X., Jiang, Y., Fang, X. Angiopep-conjugated poly(ethylene glycol)-co-poly(ϵ -caprolactone) nanoparticles as dual-targeting drug delivery system for brain glioma. *Biomaterials* **32**, 4293–4305 (2011).
111. Liu, J. & Shapiro, J. I. Endocytosis and Signal Transduction: Basic Science Update. *Biol. Res. Nurs.* **5**, 117–128 (2003).
112. Slowing, I., Trewyn, B. G. & Lin, V. S.-Y. Effect of Surface Functionalization of MCM-41-Type Mesoporous Silica Nanoparticles on the Endocytosis by Human Cancer Cells. *J. Am. Chem. Soc.* **128**, 14792–14793 (2006).

113. Zhang, L. W. & Monteiro-Riviere, N. A. Mechanism of Quantum Dot Nanoparticle Cellular Uptake. *Toxicol. Sci.* (2009).
114. Kuthati, Y., Sung, P.-J., Weng, C.-F., Mou, C.-Y. & Lee, C.-H. Functionalization of mesoporous silica nanoparticles for targeting, biocompatibility, combined cancer therapies and theragnosis. *J. Nanosci. Nanotechnol.* **13**, 2399–2430 (2013).
115. Barua, S. & Rege, K. Cancer-cell-phenotype-dependent differential intracellular trafficking of unconjugated quantum dots. *Small Wein. Bergstr. Ger.* **5**, 370–376 (2009).
116. Jiang, W., Kim, B. Y. S., Rutka, J. T. & Chan, W. C. W. Nanoparticle-mediated cellular response is size-dependent. *Nat. Nanotechnol.* **3**, 145–150 (2008).
117. Mazzucchelli, S. *et al.* Multiple presentation of Scfv800E6 on silica nanospheres enhances targeting efficiency toward HER-2 receptor in breast cancer cells. *Bioconjug. Chem.* **22**, 2296–2303 (2011).
118. Hong, S., Leroueil, P.R., Majoros, I.J., Orr, B.G., Baker, J.R., Banaszak, H. The binding avidity of a nanoparticle-based multivalent targeted drug delivery platform. *Chem. Biol.* **14**, 107–115 (2007).
119. Nelson, D. L., Nelson, D. L., Lehninger, A. L. & Cox, M. M. *Lehninger principles of biochemistry*. (W.H. Freeman, 2008).
120. Warenus, H. M., Galfre, G., Bleehen, N. M. & Milstein, C. Attempted targeting of a monoclonal antibody in a human tumour xenograft system. *Eur. J. Cancer Clin. Oncol.* **17**, 1009–1015 (1981).
121. Carter, P., Smith, L. & Ryan, M. Identification and validation of cell surface antigens for antibody targeting in oncology. *Endocr. Relat. Cancer* **11**, 659–87 (2004).
122. Bayly, A. M., Kortt, A., Hudson, P. J. & Power, B. E. Large-scale bacterial fermentation and isolation of scFv multimers using a heat-inducible bacterial expression vector. *J. Immunol. Methods* **262**, 217–27 (2002).
123. Reimer, L., *Elements of a Transmission Electron Microscope*, (Springer Berlin 1993)
124. Ruoslahti, E. Specialization of tumour vasculature. *Nat. Rev. Cancer* **2**, 83–90 (2002).
125. Peer, D., Karp, J.M. Hong, S., Farokhzad, O.C. Margalit, R., Langer, R. Nanocarriers as an emerging platform for cancer therapy. *Nat. Nanotechnol.* **2**, 751–760 (2007).
126. Milgroom, A., Intrator, M., Madhavan, K., Mazzaro, L., Shandas, R., Liu B., Park, D. Mesoporous silica nanoparticles as a breast-cancer targeting ultrasound contrast agent. *Colloids Surf. B Biointerfaces* (2013).

127. Ma, M., Zhang, Y., Gong, H., Li, F. & Gu, N. Silica-Coated Magnetite Nanoparticles Labeled by Nimotuzumab, A Humanised Monoclonal Antibody to Epidermal Growth Factor Receptor: Preparations, Specific Targeting and Bioimaging. *J. Nanosci. Nanotechnol.* **13**, 6541–6545 (2013).
128. Vallet-Regi, M., Rámila, A., del Real, R. P. & Pérez-Pariente, J. A New Property of MCM-41: Drug Delivery System. *Chem. Mater.* **13**, 308–311 (2001).
129. Pasqua, L., Cundari, S., Ceresa, C. & Cavaletti, G. Recent Development, Applications, and Perspectives of Mesoporous Silica Particles in Medicine and Biotechnology. *Curr. Med. Chem.* **16**, 3054–3063 (2009).
130. Corine Tourné-Péteilh , Daniel Brunel , Sylvie Bégu , Bich Chiche , François Fajula, D. A. L. and J.-M. D. Synthesis and characterisation of ibuprofen-anchored MCM-41 silica and silica gel. **27**, 1415–1418 (2003).
131. Arruebo, M. Drug delivery from structured porous inorganic materials. *Wiley Interdiscip. Rev. Nanomed. Nanobiotechnol.* **4**, 16–30 (2012).
132. Langer, R. Drug delivery and targeting. *Nature* **392**, 5–10 (1998).
133. Rosenholm, J. M. & Lindén, M. Towards establishing structure-activity relationships for mesoporous silica in drug delivery applications. *J. Control. Release* **128**, 157–64 (2008).
134. Andersson, J., Rosenholm, J., Areva, S. & Linde, M. Influences of Material Characteristics on Ibuprofen Drug Loading and Release Profiles from Ordered Micro- and Mesoporous Silica Matrices. 4160–4167 (2004).
135. Deere, J., Magner, E., Wall, J. G. & Hodnett, B. K. Adsorption and activity of cytochrome c on mesoporous silicates. *Chem. Commun.* 465–465 (2001).
136. Mortera, R., Vivero-Escoto, J., Slowing, I.I., Garrone, E., Onida, B., Lin, V.S. Cell-induced intracellular controlled release of membrane impermeable cysteine from a mesoporous silica nanoparticle-based drug delivery system. *Chem. Commun.* 3219–21 (2009).
137. Benezra, M., Penate-Medina, O., Zanzonico, P.B., Schaer, D., Ow, H., Burns, A., DeStanchina, E., Longo, V., Herz, E., Iyer, S., Wolchok, J., Larson, S.T., Wiesner, U., Bradbury, M.S. Multimodal silica nanoparticles are effective cancer-targeted probes in a model of human melanoma. *J. Clin. Invest.* **121**, 2768–2780 (2011).
138. Mamaeva, V., Rosenholm, J.M., Bate-Eya, L.T., Bergman, L., Peuhu, E., Duchanoy, A., Fortelius, L.E., Landor, S., Toivola, D.M., Lindén, M., Sahlgren, C. Mesoporous Silica Nanoparticles as Drug Delivery Systems for Targeted Inhibition of Notch Signaling in Cancer. *Mol. Ther.* **19**, 1538–1546 (2011).
139. Zhang, Q., Wang, X., Li, P-Z., Nguyen, K.T., Wang, X-J., Luo, Z., Zhang, H., Soon, N., Zhao, Y. Biocompatible, Uniform, and Redispersible Mesoporous Silica Nanoparticles for Cancer-Targeted Drug Delivery In Vivo. *Adv. Funct. Mater.* **24**, (17) 2450-2461 (2014)

140. Papat, A., Hartono S.B., Stahr, F., Liu, J., Qiao, S.Z., Qing, M.L.G. Mesoporous silica nanoparticles for bioadsorption, enzyme immobilisation, and delivery carriers. *Nanoscale* **3**, 2801–2818 (2011).
141. Zhao, Y., Trewyn, B. G., Slowing, I. I. & Lin, V. S.-Y. Mesoporous Silica Nanoparticle-Based Double Drug Delivery System for Glucose-Responsive Controlled Release of Insulin and Cyclic AMP. *J. Am. Chem. Soc.* **131**, 8398–8400 (2009).
142. Cheng, K., El-Boubbou, K. & Landry, C. C. Binding of HIV-1 gp120 glycoprotein to silica nanoparticles modified with CD4 glycoprotein and CD4 peptide fragments. *ACS Appl. Mater. Interfaces* **4**, 235–243 (2012).
143. Nembrinia, C., Stanoa, A., Danea, K.Y., Ballester M., Vliesa, A.J., Marslandc, B.J., Swartzb, M.A., Hubbella, J.A. Nanoparticle conjugation of antigen enhances cytotoxic T-cell responses in pulmonary vaccination. *Proc. Natl. Acad. Sci.* **108**, E989–E997 (2011).
144. Tittaa, A., Ballester M., Juliera, Z., Nembrinia, C., Jeanbarta, L., Vliesa, A., Swartz, M.A., Hubbella, J.A. Nanoparticle conjugation of CpG enhances adjuvancy for cellular immunity and memory recall at low dose. *Proc. Natl. Acad. Sci.* 201313152 (2013).
145. Iler, R. *The Chemistry of Silica: Solubility, Polymerization, Colloid and Surface Properties and Biochemistry of Silica*. (Wiley-VCH Verlag GmbH & Co. KGaA, 1979).
146. Etienne, M. & Walcarius, A. Analytical investigation of the chemical reactivity and stability of aminopropyl-grafted silica in aqueous medium. *Talanta* **59**, 1173–88 (2003).
147. Wilson, T. *Confocal Microscopy*, (Academic Press, 1990)
148. Mortera, R., Fiorilli, S., Garrone, E., Verné, E., Onida, B. Pores occlusion in MCM-41 spheres immersed in SBF and the effect on ibuprofen delivery kinetics : A quantitative model. *Chem. Eng. J.* **156**, 184–192 (2010).
149. He, Q., Shi, J. Zhu, M., Chen, Y., Chen, F. The three-stage in vitro degradation behavior of mesoporous silica in simulated body fluid. *Microporous Mesoporous Mater.* **131**, 314–320 (2010).
150. Zhai, W., He, C., Wu L., Zhou, Y., Chen, H., Chang, J., Zhang H. Degradation of hollow mesoporous silica nanoparticles in human umbilical vein endothelial cells. *J. Biomed. Mater. Res. B Appl. Biomater.* **100**, 1397–1403 (2012).
151. Ågren, P. Influence of Non-Ionic Polymers and Cationic Surfactants on Silica Sols, Gels and Porous Ceramic Materials. (Åbo Akademi, 1999) (ISBN 9521205652)
152. Rouquerol, F., Rouquerol, J., Sing, K. *Adsorption by powders and porous solids - principles, methodology and applications*. (Academic Press, 1999).
153. Pawley B. P. *Handbook of Biological Confocal Microscopy*. (Springer Science+Business Media LLC, 2006)

154. Barrett, E. P., Joyner, L. G. & Halenda, P.P. The Determination of Pore Volume and Area Distributions in Porous Substances. I. Computations from Nitrogen Isotherms. *J. Am. Chem. Soc.* **73**, 373–380 (1951).
155. Ravikovitch, P. I., Wei, D., Chueh, W. T., Haller, G. L. & Neimark, A. V. Evaluation of Pore Structure Parameters of MCM-41 Catalyst Supports and Catalysts by Means of Nitrogen and Argon Adsorption. *J. Phys. Chem. B* **101**, 3671–3679 (1997).
156. Hiemenz, P. C. & Rajagopalan, R. *Principles of Colloid and Surface Chemistry, Third Edition, Revised and Expanded*. (CRC Press, 1997).
157. Shaw, D. J. *Introduction to colloid and surface chemistry*. (Butterworth-Heinemann, 1992) ISBN 0750611820.
158. Flegler, S. L., Heckman, J. & Klomparens, K. L. *Scanning and Transmission Electron Microscopy -An Introduction*. (Oxford University Press, 1995).
159. Kazmiruk, V. *Scanning Electron Microscopy*, (InTech 2012)
160. Williams, D. B. & Carter, C. B. *Transmission Electron Microscopy: A Textbook for Materials Science*. (Springer, 2009).
161. Principal picture of TEM and SEM. <<http://www.uiowa.edu/~cemrf/methodology/tem/index.htm>>, accessed 11 June 14
162. Paddock, S. W. *Confocal microscopy methods and protocols*. (Humana Press, 1999).
163. *Handbook of Biological Confocal Microscopy*. <<http://www.springer.com/life+sciences/biochemistry+%26+biophysics/book/978-0-387-25921-5>>, accessed 11 June 14
164. A principal picture of a confocal microscope. <http://en.wikipedia.org/wiki/Confocal_laser_scanning_microscopy>, accessed 11 June 14
165. Rosenholm, J.M., Czuryzskiewicz, T., Kleitz, F., Rosenholm, J. B. & Lindén, M. On the Nature of the Brønsted Acidic Groups on Native and Functionalized Mesoporous Siliceous SBA-15 as Studied by Benzylamine Adsorption from Solution. *Langmuir* **23**, 4315–4323 (2007).
166. Kankaanpää, P., Paavolainen, L., Tiitta, S., Karjalainen, M., Päivärinne, J., Nieminen, J., Marjomäki, V., Heino, J., White, D.J. BioImageXD: An open, general-purpose and high-throughput image-processing platform. *Nat. Methods* **9**, 683–689 (2012).
167. Guo, S. & Huang, L. Nanoparticles Escaping RES and Endosome: Challenges for siRNA Delivery for Cancer Therapy. *J. Nanomater.* **2011**, (2011).
168. Upla, P., Marjomäki, V., Kankaanpää, P., Ivaska, J., Hyypiä, T., Van Der Goot, F.G., Heino, J. Clustering induces a lateral redistribution of alpha 2 beta 1 integrin from membrane rafts to caveolae and subsequent protein kinase C-dependent internalization. *Mol. Biol. Cell* **15**, 625–636 (2004).

169. Marjomäki, V., Pietiäinen, V., Matilainen, H., Upla, P., Ivaska, J., Nissinen, L., Reunanen, H., Huttunen, P., Hyypiä, T., Heino, J. Internalization of echovirus 1 in caveolae. *J. Virol.* **76**, 1856–1865 (2002).
170. Chuang, K.H., Wang, H.E., Chen, F.M., Tzou, S.C., Cheng, C.M., Chang, Y.C., Tseng, W.L., Shiea, J., Lin, S.R., Wang, J.Y., Chen, B.M., Roffler, S.R., Cheng, T.L. Endocytosis of PEGylated Agents Enhances Cancer Imaging and Anticancer Efficacy. *Mol. Cancer Ther.* **9**, 1903–1912 (2010).
171. Karjalainen, M., Kakkonen, E., Upla, P., Paloranta, H., Kankaanpää, P., Liberali, P., Renkema, H., Hyypiä, T., Heino, J., Marjomäki, V. A Raft-derived, Pak1-regulated Entry Participates in $\alpha 2\beta 1$ Integrin-dependent Sorting to Caveosomes. *Mol. Biol. Cell* **19**, 2857–2869 (2008).
172. Folic acid, molecular structure. at <http://en.wikipedia.org/wiki/Folic_acid>, accessed 11 June 14
173. Rosenholm, J. M., Peuhu, E., Eriksson, J. E., Sahlgren, C. & Lindén, M. Targeted intracellular delivery of hydrophobic agents using mesoporous hybrid silica nanoparticles as carrier systems. *Nano Lett.* **9**, 3308–3311 (2009).
174. Rizzo, P., Miao, H., D'Souza, G., Osipo, C., Song, L.L., Yun, J., Zhao, H., Mascarenhas, J., Wyatt, D., Antico, G., Hao, L., Yao, K., Rajan, P., Hicks, C., Siziopikou, K., Selvaggi, S., Bashir, A., Bhandari, D., Marchese, A., Lendahl, U., Qin, J.Z., Tonetti, D.A., Albain, K., Nickoloff, B.J., Miele L. Cross-talk between notch and the estrogen receptor in breast cancer suggests novel therapeutic approaches. *Cancer Res.* **68**, 5226–5235 (2008).
175. Givan, A.L. *Flow Cytometry: First Principles*. (Wiley-Liss, 1992)
176. Melamed MR. *Flow Cytometry and Sorting*. (Wiley-Liss, 1990)
177. Shapiro H. *Practical Flow Cytometry*. (Wiley-Liss, 1994)
178. Yamada, H.; Urata, C.; Aoyama, T.; Osada, S.; Yamauchi, Y.; Kuroda, K. Preparation of Colloidal Mesoporous Silica Nanoparticles with Different Diameters and Their Unique degradation Behavior in Static Aqueous Systems. *Chem. Mater.* **2012**, 24, 1462.
179. R.J. Hunter, *Potential in Colloidal Science, Principles and Applications*. (Academic Press Limited, 1988)

